

University of Rajshahi

Rajshahi-6205

Bangladesh.

RUCL Institutional Repository

<http://rulrepository.ru.ac.bd>

Department of Electrical and Electronic Engineering

PhD Thesis

2016

Hybrid and Eddy Current Belt Sensors for Quality Control of Nonferrous Scrap Metals from Municipal Solid Waste Incinerator Bottom Ash

Rahman, Md. Abdur

University of Rajshahi

<http://rulrepository.ru.ac.bd/handle/123456789/347>

Copyright to the University of Rajshahi. All rights reserved. Downloaded from RUCL Institutional Repository.

Hybrid and Eddy Current Belt Sensors for Quality Control of
Nonferrous Scrap Metals from Municipal Solid Waste
Incinerator Bottom Ash



Ph.D. Thesis

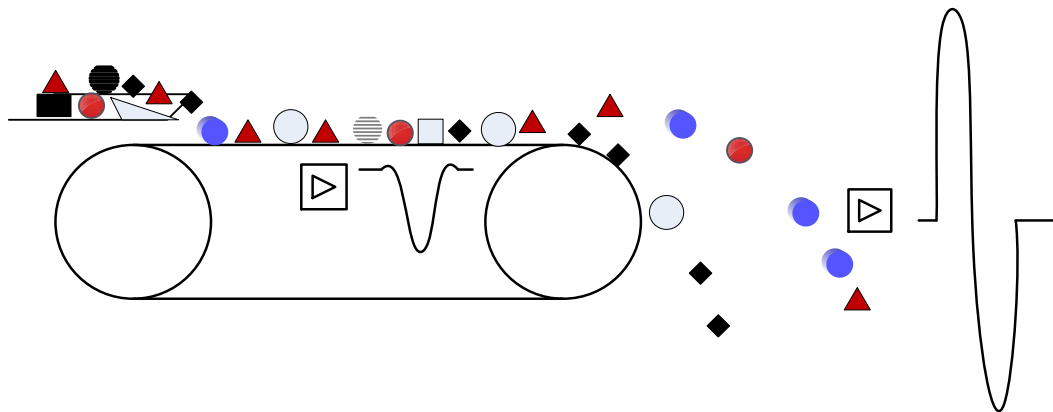
By

Md. Abdur Rahman

Submitted To

The Department of Applied Physics and Electronic Engineering
The University of Rajshahi for Doctor of Philosophy (Science) Degree

Session: - 2015-2016, Roll: - 1600074502



Resources & Recycling Laboratory, Materials and Environment, Faculty of Civil
Engineering and Geosciences, Delft University of Technology, Netherlands

&

Department of Applied Physics and Electronic Engineering,
The University of Rajshahi, Rajshahi-6205, Bangladesh

November 2016, Rajshahi

Hybrid and Eddy Current Belt Sensors for Quality Control of
Nonferrous Scrap Metals from Municipal Solid Waste
Incinerator Bottom Ash



Ph.D. Thesis

By

Md. Abdur Rahman

Session: - 2015-2016, Roll: - 1600074502

Assistant Professor

Department of Applied Physics and Electronic Engineering

The University of Rajshahi

Ph.D. Thesis

Hybrid and Eddy Current Belt Sensors for Quality Control of
Nonferrous Scrap Metals from Municipal Solid Waste Incinerator
Bottom Ash

November, 2016

Dedicated to my parents

Md. Abdus Sattar and Begum Rokeya.

Acknowledgements

First of all I remember the time at Delft University of Technology, Netherlands where I have completed the major parts of this thesis under all kind of supports and laboratory facilities provided by resources and recycling laboratory there. I am grateful to my Co-Supervisor Dr. M.C.M Bakker who was guiding this Ph.D. work in that laboratory. I gratefully appreciate his contributions to build up me as a competitive individual in producing research especially in the field of sensor sorting and quality control of waste materials. Moreover his contributions to the successive revisions of this thesis are gratefully acknowledged.

Afterwards I came up with the name of Prof. Abu Bakar Md. Ismail for his kind cooperation as a supervisor to complete this Ph.D. thesis at the University of Rajshahi. Prof. Ismail was very enthusiastic to this research and his successive suggestions throughout the submission processes of this thesis are gratefully acknowledged. I appreciate teachers and colleagues for their supports and suggestions those came up during my seminars held in the department of Applied Physics and Electronic Engineering at the University of Rajshahi.

Afterwards I remember a long endeavour to complete this thesis. Actually this research was primarily initiated for developing a sensor system for quality control of eddy currents separator (ECS) concentrated bottom ash materials, size fraction 1-6mm that led a hybrid sensor system. To this point I would like to express my sincere thanks to Thijs van de Winckel for his cooperation to carry out some experimental tests for functionality analyses of the developed hybrid sensor in situ. I am grateful to FONDEL B.V. and INASHCO B.V. for supplying the bottom ash sample materials to carry out this sensor research at Delft University of Technology. The electronic and mechanical support division (DEMO) of Delft University of Technology built the hybrid sensor from the design of laboratory prototype unit, which is gratefully acknowledged here. Later this sensor research was extended to a fundamental issue in the field of sensor sorting of metal scraps in bottom ash materials that led eddy current belt sensor. I gratefully appreciate Peter Berkhout, Ron, Mohammed and again the DEMO

division for their technical cooperation to build up experimental set up of the eddy current belt sensor. I remember the name of other Ph.D. students such as Bin Hu, Seyed Ali Sanaee, Somi Lotfi who were my friends there and I gratefully acknowledge their friendly cooperation to carry out this research in that laboratory.

To the end what I am feeling is the name of my father Md. Abdus Sattar and the name of my mother Begum Rokeya. I am so grateful to them for their countless contributions throughout my life. I gratefully appreciate my father in law Abdul Hadi Md. Anwar for his continuous encouragement to complete this thesis. And at last but not least I am grateful to my family members for their supports and patience to complete this thesis.

The Author

Author's Declaration for the Originality of the Ph.D. Thesis

I hereby declare that the Ph.D. thesis entitled “**Hybrid and Eddy Current Belt Sensors for Quality Control of Nonferrous Scrap Metals from Municipal Solid Waste Incinerator Bottom Ash**” session 2015-2016 submitted to the Department of Applied Physics and Electronic Engineering, University of Rajshahi is my own research outcome. I also state that the experimental design, method, sample preparation, data analyses and preparation of the results presented in this thesis are originally performed at my own investigations and completed at the Resources and Recycling Laboratory, Delft University of Technology, Netherlands.

At the end I humbly and consciously declare that this thesis or a part of this thesis has not been presented at this or any other university for any degree or prize.

Date: 08 November 2016

The Author

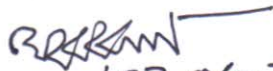
 10.11.2016

Md. Abdur Rahman,
Ph.D. candidate, Session: 2015-216, Roll: 1600074502
Assistant Professor
Department of Applied Physics and Electronic Engineering.
University of Rajshahi

Author's Declaration for the Corrections Made to the Ph.D. Thesis


In response to the comments and queries made by the honourable examiners of this thesis, I, as the author hereby declare that I have completed the suggested minor corrections to the Ph.D. thesis entitled "**Hybrid and Eddy Current Belt Sensors for Quality Control of Nonferrous Scrap Metals from Municipal Solid Waste Incinerator Bottom Ash**" which have been agreed by honourable principle supervisor Prof. Abu Bakar Md. Ismail, Department of Applied Physics and Electronic Engineering, University of Rajshahi.

The Author


03.04.2017

Md. Abdur Rahman,
Ph.D. candidate, Session: 2015-216,
Roll: 1600074502
Assistant Professor
Department of Applied Physics and
Electronic Engineering
University of Rajshahi

Principle Supervisor


04.04.2017

Prof. Abu Bakar Md. Ismail
Department of Applied Physics and
Electronic Engineering
University of Rajshahi

আবু বকর মোঃ ইসমাইল, পি-এইচ.ডি.
 প্রফেসর
 ফলিত পদার্থবিজ্ঞান ও ইলেকট্রনিক ইঞ্জিনিয়ারিং
 বিভাগ
 রাজশাহী বিশ্ববিদ্যালয়
 রাজশাহী-৬২০৫, বাংলাদেশ।



Abu Bakar Md. Ismail, Ph.D
 Professor
 Dept. of Applied Physics &
 Electronic Engineering.
 Rajshahi University
 Rajshahi-6205, Bangladesh.

Tel: +88-0721-711658(O), +880-721-770701(R), Cell: +88-01712-511-457 Fax: +88-0721-750064,
 Email:ismail@ru.ac.bd

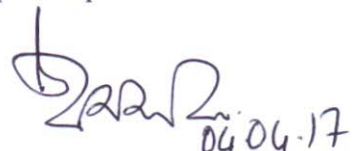
Principle Supervisor's Certification

This is to certify that the work embodied in the accompanying thesis entitled **“Hybrid and Eddy Current Belt Sensors for Quality Control of Nonferrous Scrap Metals from Municipal Solid Waste Incinerator Bottom Ash”**, submitted by **Md. Abdur Rahman** submitted to the Department of Applied Physics and Electronic Engineering, University of Rajshahi in the session 2015-2016, was his own research investigation except where otherwise acknowledged. The experimental parts of this thesis are carried out in Resource and Recycling Laboratory, under the Faculty of Civil Engineering and Geosciences, Delft University of Technology, Netherlands where Dr. M.C.M Bakker was guiding as a co-supervisor of his Ph.D. work.

The candidate has fulfilled the requirements of the regulations laid down for the **Doctor of Philosophy (Science) Degree** examination of the University of Rajshahi. I have read this thesis and to the best of my knowledge this work has not been submitted elsewhere for any other degree or diploma and I certify that the presented thesis is prepared properly and worthy of examination.

Dated: 03 April 2017

Principle Supervisor


 Abu Bakar Md. Ismail 04.04.17

SUMMARY

The municipal solid waste (MSW) is so complex but a significant secondary source of materials. The incombustible residue after the incineration of the MSW is known as municipal solid waste incinerator (MSWI) bottom ash that is mostly a mix of organic and mainly inorganic materials as well as a significant secondary source of ferrous and nonferrous (NF) metals. However, despite the technological development of eddy current separator (ECS), the recovery of NF contents from MSWI bottom ash, size 1-6mm remains unsatisfactory where the splitter setting of an ECS machine plays crucial role for effective separation and quality control of nonferrous metals and non-metals. For effective separation and quality control of the bottom ash materials the ECS machine needs continuous adjustment of the splitter setting which is quite impractical for a manual operator as a result this thesis primarily addresses this issue by suggesting a sensor based remedy for that.

Accordingly this Ph.D. thesis embodied the development of two different kinds of sensors namely hybrid sensor and eddy current belt sensor. The hybrid sensor was developed for the measurement of metal grade (G) of the ECS concentrated bottom ash materials and the measured (G) was used as a qualifier for the quality control of the bottom ash materials. Actually the hybrid sensor produces count data for metal and non-metal particles present in the ECS concentrated bottom ash stream where the hybrid sensor consists of infrared sensor (IRS) for counting all types of particles present in the stream and electromagnetic sensor (EMS) for counting only the metal particles present in the stream. A mathematical model is developed that calculates the metal grade (G) from the sensor count data with the pre-knowledge of average particle mass ratio (k) between non-metal and metal.

Consequently this research first focused on design, construction and characterization of the hybrid sensor. Each sensor section is characterized individually in terms of sensitivity, repeatability and accuracy. The hybrid sensor was highly repeatable to its count data and the math model for the measurement of G was verified using the synthetic sample with known values of k i.e. were $k = 0.24, 0.54, 1.23$ and 2.54 . The same method was applied for the grade measurement of the ECS concentrated bottom ash materials with an accuracy $\pm 2.4\%$.

After the laboratory characterization a robust set up from the laboratory prototype of the hybrid sensor was built for functionality analyses in situ. The measurements and trends in sensor data from the laboratory and in situ for dry feed materials were quite comparable, considering the ECS machines were different and the bottom ashes came from different sources. The hybrid sensor data predicted quite accurately the trend of the metal grade of the stream of the particles with the splitter distance, which was mandatory for sensor-based control of the ECS splitter position in bottom ash processing.

Afterwards this thesis presented an extended part of this sensor research that resulted another fundamental investigation on the development of an eddy current belt sensor. The purpose of the belt sensor was to identify NF scrap metals on a conveyor that could be applied for sensor sorting and quality control of bottom ash materials. The belt sensor relies on a mathematical method which is called in this thesis as conductivity approach. In conductivity approach a parameter *CIF* (conductivity indication factor) has been defined from where the *CIF* has been found as truly a function of conductivity. This thesis suggested producing a database of material *CIF* that was used for the identification of different materials based on conductivity.

For experimental validation of the conductivity approach a set of pure sample particles S1 of Cu, Al, and Brass, each of six generic shapes i.e. disk, disk block, square plate, square block, rod, and cylinder were investigated. The test analyses for the sample set S1 showed 100% accuracy for the identification of the Cu, Al and Brass by using their average *CIF* values. As an application of the eddy current belt sensor another sample set S2 i.e. a representative amount of randomly mixed metal scraps of Cu, Al, Brass and Zn collected from a batch of bottom ash materials was used as a test case for the identification of different metals using their measured *CIF* values. As a first step towards an application of the belt sensor, the thesis also presented a logical sorting statistics of the bottom ash scraps based on their average *CIF* values. Moreover, the calculated and calibrated conductivity values of the metal scraps using only the belt sensor were also presented and finally some recommendations have been compiled for further advancement of sensor sorting of waste and quality control of bottom ash materials.

Date 08-11-2016
Our reference R&R-TUD-231116-11
Contact person Dr. ir. M.C.M. Bakker
Telephone/fax +31-(0)15-2785219
E-mail m.c.m.bakker@tudelft.nl



Delft University of Technology

Concerns: Co-Supervisor's certification of originality of Ph.D. thesis of Mr. Md Abdur Rahman University of Rajshahi Rajshahi-6205, Bangladesh

Faculty of Civil Engineering and Geosciences
Resources & Recycling group

Visiting address
Stevinweg 1
2628 CN Delft
Postal address
P.O. Box 5048
2600 GA Delft
The Netherlands

Co-Supervisor's certification of the Originality of the Ph.D. Thesis

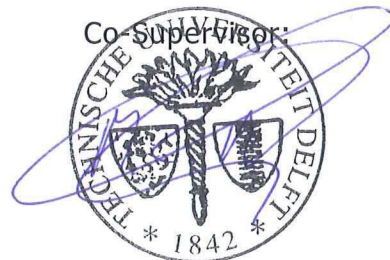
I hereby truthfully certify that the Ph.D. thesis entitled "Hybrid and Eddy Current Belt Sensors for Quality Control of Nonferrous Scrap Metals from Municipal Solid Waste Incinerator Bottom Ash", session 2015-2016 submitted to the Department of Applied Physics and Electronic Engineering of the University of Rajshahi, is solely the research outcome of Md. Abdur Rahman. I also certify that the experimental design, method, sample preparation, data analyses and preparation of the results presented in this thesis are original and obtained solely by Md. Abdur Rahman's investigations, which were mainly prepared and completed at the Resources and Recycling Laboratory, Delft University of Technology, The Netherlands.

This thesis work has led two published scientific articles in the internationally reputed journal "Waste Management", as well as an international patent application in world intellectual property organization (WIPO), international patent number #WO 2012/118373A1, on the basis of Md. Abdur Rahman's contributions to the world scientific literature database on sensor sorting and quality control, specifically in the field of bottom ash waste materials.

I certify that no part(s) of this thesis have before been presented at the University of Rajshahi, or at any other university, for any degree or prize. I therefore fully recommend this thesis for the degree of doctor of philosophy (Ph.D) of Mr. Rahman in Applied Physics and Electronic Engineering at University of Rajshahi.

Dated: 8 Nov 2016

(University seal)



Dr. ir. M.C.M. Bakker

List of publications from this research to date:

1. **Rahman Md. A.**, Bakker M. C. M., 2013, Sensor based control in eddy current separation of incinerator bottom ash, Waste Management 33, pp.1418-1424.
2. **Rahman Md.** Bakker M.C.M, 2012, Hybrid sensor for metal grade measurement of a falling stream of solid waste particles, Waste Management 32, pp. 1316-1323.
3. **Patent: Rem P.C.** Bakker M.C.M. Berkhout S.P.M, Rahman Md. Abdur, 2012, International Patent nr. WO 2012/118373 A1.

List of acronyms and symbols:

AM	amplitude modulation;
ECS	eddy currents separator;
EMS	electromagnetic sensor;
IRS	infrared sensor;
LIBS	laser induced breakdown;
MSW	municipal solid waste;
MSWI	municipal solid waste incinerator
NF	nonferrous;
XRF	X-ray fluorescence;
A_{disk}	bottom surface projection of reference disk;
A_{eff}	effective projected field surface of a particle;
A_{1z}^p	effective magnetic vector potential of a particle at ω_1 ;
B_{1sum}^a	applied z-component dominating time varying magnetic field at ω_1 ;
B_{2sum}^a	applied z-component dominating time varying magnetic field at ω_2 ;
B_{1sum}	peak amplitude of applied field B_{1sum}^a ;
B_{2sum}	peak amplitude of applied field B_{2sum}^a ;
B_{1x}^{L1}	field produced along x-direction by bias coil L_1 at ω_1 ;
B_{2x}^{L1}	field produced along x-direction by bias coil L_1 at ω_2 and so on;
B_{1xsum}	sum of the field components along x direction produced by the bias coils L_1 and L_2 at ω_1 and so on;
B_{1z}^p	effective z field produced by an arbitrary particle at ω_1 for m_{1z}^p and so on;
$C1$	count correction parameter for hybrid sensor Chapter 2 and 3;
C^{IRS}	count correction factor for IRS;
C^{EMS}	count correction factor for EMS;
$C2$	ratio between the effective projected field surface of a particle and a reference particle in Chapter 4 and 5;
CIF	conductivity indication factor;
d_{disk}	thickness of reference disk;
G	metal grade;
G_m	manually analysed metal grade;

G_s	measured metal grade;
k	average particle mass ratio between non-metal and metal;
m^{metal}	average particle mass of metal;
$m^{non-metal}$	average particle mass of minerals or non-metals;
$m_{1z\text{eff}}^{disk}$	effective magnetic moment of a reference disk particle at ω_1 ;
$m_{2z\text{eff}}^{disk}$	effective magnetic moment of a reference disk particle at ω_2 ;
$m_{1z\text{eff}}^p$	effective z-magnetic moment of a particle at ω_1 and so on;
N^{EMS}	metal count by EMS;
N^{IRS}	non-metal count by IRS;
r	distance;
\hat{r}	unit vector;
V_{1z}^{tot}	total voltage induced in z receiver at ω_1 and so on;
Z	count ratio between metal and non-metal;
ω	angular frequency;
ω_1	sufficiently low angular frequency;
ω_2	sufficiently high angular frequency;
σ	conductivity of a particle;
μ_0	magnetic permeability of free space;

List of Tables:

Table no.	Title	Page
Table 1.1:	A list of traditional and sensor sorting techniques.	8
Table 2.1:	Four k -values using sand-metal particles mixtures.	20
Table 2.2:	Threshold detection voltage for +1 mm particles.	25
Table 2.3:	Repeatability test using a sample mixer of 1605 sand particles and 300 metal particles.	25
Table 2.4:	Metal grade analyses of bottom ash samples, each of 100 g, sieve size 1-6 mm, particle feed rate 13 per second, $CI = 1$ is assumed, $k=0.49$ in G_s calculation	31
Table 2.5:	Calculation of measured grade (G_s) using the data from Figures 2.5c and 2.5d. The manually analysed grade (G_m) was $G_m = 23.2\%$ and $k=0.49$ in G_s calculation (from Table 2.4).	32
Table 5.1:	Specifications of the belt sensor	68
Table 5.2:	Specifications of pure sample set S1. Circular particles have a diameter of 11.3 mm and square ones have a cross section of 10 x 10 mm.	71
Table 5.3:	One and two sided magnetic penetration depths (3 skin depths) for three metal types.	94

List of Figures:

Figure no.	Figure caption	Page
Figure 1.1:	A typical flow diagram of municipal solid waste (MSW) recycling for material upgradation and recovery from various generation sites.	3
Figure 1.2:	(a) A pile of naturally dried MSWI bottom ash, size fraction 0-6mm in a waste energy conversion plant that comes as a residue from an incinerator of a waste to energy conversion plant. (b) ECS concentrated moist NF fractions, size 0-6mm. (c) Manually analyzed NF metal contents from a subsample of (b).	4
Figure 1.3:	(a) Principle of ECS separation. Trajectories of small nonferrous metal and mineral particles overlap and the splitter must be set in a compromise. (b) The sensor system measures metal grade and amounts of metal and mineral particles, allowing for online quality assessment or online splitter control.	6
Figure 1.4:	A flow diagram of pre-melt hybrid physical separation system.	11
Figure 2.1:	(a) Synthetic sample material and (b) ECS concentrated bottom ash.	20
Figure 2.2:	(a) The hybrid sensor main build-up and data flow and (b) the prototype unit with feed tube and an Aluminium shield for EMS.	21
Figure 2.3:	Layout of the infrared sensor (IRS).	23
Figure 2.4:	EMS detection principle and dataflow.	23
Figure 2.5:	(a) Sensor counts against particle feed rate for the synthetic sample.(b) Count correction parameters for the synthetic sample counts in Figure 2.5a. (c) Sensor counts against maximum count rate for bottom ash and (d) Count correction parameters for the bottom ash counts in Figure 2.5c.	27
Figure 2.6:	(a) Solid lines: prediction using Eq. (2.3) for $CI = 1$. Markers: Experiments using synthetic samples at a low feed rate with $CI = 0.99$. (b) Measured grade against the calibrated grade corresponding to (a).	28
Figure 2.7:	(a) Mass distribution over the sieve size ranges of the bottom ash sample. (b) Signal to noise ratio (SNR) in the sieve size ranges for bottom ash.	29
Figure 3.1:	ECS settings with the sensor unit mounted on the splitter at the metal concentrate side (a) In the laboratory and (b) In-situ at a bottom ash treatment plant.	39

- Figure 3.2: Bottom ash from batch L with size fraction <6 mm used in the laboratory tests. (a) Feed material. (b) Non-ferrous metal concentrate sampled by the sensor. (c) Metal content of the sensor sample after roll crusher to remove minerals. 40
- Figure 3.3: Bottom ash from batch L with size fraction <6 mm used in the laboratory tests. (a) Feed material. (b) Non-ferrous metal concentrate sampled by the sensor. (c) Metal content of the sensor sample after roll crusher to remove minerals. 42
- Figure 3.4: Laboratory measurements of the average particle mass of metals and minerals. 42
- Figure 3.5: Laboratory test comparisons of metal and mineral sensor counts, sensor grade, and recovery of the complete metals concentrate. The feed grade was 6.6%. 43
- Figure 3.6: In-situ average particle mass ratio for dry and wet 1-6 mm bottom ash, measured at five different splitter distances. Notice that the wet particles landed on average 22 mm closer to the ECS drum. 46
- Figure 3.7: In-situ counts of mineral and metal particles, sensor grade and product bin grade for 1-6 mm dry bottom ash using $k = 0.60$. 46
- Figure 3.8: In-situ grade measurements integrated over one minute interval for $k=0.6$ at the five splitter locations for dry bottom ash. The average of five minutes is shown as a dotted line. 47
- Figure 3.9: In-situ measurements of the average particle mass of metals and minerals. (a) Dry bottom ash. (b) Wet bottom ash. 47
- Figure 3.10: In-situ counts of mineral and metal particles, sensor grade ($k = 1.22$) and product bin grade for wet 1-6 mm bottom ash. 49
- Figure 4.1: Typical situation of the belt sensor for the conductivity approach. (a) Shows the dominant and homogenous applied z-field for a certain frequency. A rectangular coil underneath to the belt detects the scattered field from the moving metal particle. (b) Shows two rectangular type coils L1 and L2 of the belt sensor connected in Helmholtz configuration to produce the dominant z-field components B_{1sum}^a and B_{2sum}^a at the surface of the belt for two possible excitation frequencies. 56
- Figure 4.2: Shows the calculated real and imaginary parts of N_ω for pure Cu ($\sigma=5.97e7$ S/m) and Brass (15% Zn, $\sigma =2.21e7$ S/m) for a disk radius of 3 mm and thickness 1mm. 58

- Figure 4.3: Shows the main field lines and induced effective magnetic moment for different particles. (a) $m_{z_{eff}}^{disk} \hat{z}$ of a flat and round disk (b) $m_{z_{eff}}^{plate} \hat{z}$ of a square flat plate which may be approximated by the round disk, i.e. $m_{z_{eff}}^{disk} \hat{z} = m_{z_{eff}}^{plate} \hat{z}$. (c) $m_{z_{eff}}^{block} \hat{z}$ of a high block-shaped particle with its as yet unknown parameter called the effective field projection A_{eff} . 61
- Figure 5.1: (a) A sketch of the belt sensor with two bias coils L1 and L2 and one z-field sensitive receiver coil L3. (b) Experimental set up of the belt sensor. 68
- Figure 5.2: (a) The pure-metal reference sample set S1 with Cu, Al and Brass, each with six generic shapes. (b) The sample set S2 with 114 real bottom ash scraps of Cu, Al, Brass and Zn with complicated shapes and unknown conductivity. 72
- Figure 5.3: Z-responses of the belt sensor using the particles in reference sample set S1 for a constant driving voltage of 8 Vpp of the signal generator for the bias coils. (a) At sufficiently low frequency around $f_1=5.0$ kHz. (b) At sufficiently high frequency $f_2=93.0$ kHz. 74
- Figure 5.4: Measured SNR (signal to noise ratio) of the demodulated z-response of the belt sensor using 114 scraps of sample set S2 at chosen operating frequencies $f_1 = 5.0$ kHz and 93.0 kHz. 75
- Figure 5.5: (a) An equivalent electrical circuit of the belt sensor including a voltage amplifier having 50 ohm output impedance between the Agilent signal generator and the bias coils of the sensor to boost up the sensitivity of the sensor unit. (b) The calculated value of the peak current i_p through the bias coils L1 and L2 for increasing frequency. 76
- Figure 5.6: Magnetic field distribution at operating frequency $f_1= 5.0$ kHz of the sensor. (a) Homogenous dominant z-field component B_{1zsum} . (b) Moderately weaker x-field component B_{1xsum} with two strong side lobes, (c) weak y field component B_{1ysum} . (d) The total applied field $|\mathbf{B}_{1sum}|$. 77
- Figure 5.7: Magnetic field distribution at operating frequency $f_2=93.0$ kHz of the sensor. (a) Dominant z-field component B_{2zsum} . (b) Moderately weaker x-field component B_{2xsum} with two strong side lobes. (c) Weak y-field component B_{2ysum} . (d) The total applied field $|\mathbf{B}_{2sum}|$. 78

- Figure 5.8: Calculated values of $C2$ using the Eq.(5.1) that show that $C2$ scales for the different shapes and sizes of the particles in the reference sample set S1. It also shows that $C2$ is relatively insensitive to the conductivity. 79
- Figure 5.9: (a) Measured CIF of the particles of sample set S1 using the Eq. (5.2). (b) Calibrated conductivity of the particles using the Eq. (5.3). (c) Calibration constant D_{metal} for three distinctive metals. (d) Error % in the estimation of conductivity of the particles of pure sample set S1. 81
- Figure 5.10: Calculated $A_{eff}=C2A_{disk}$ of the particles in sample set S1. 82
- Figure 5.11: Measured conductivity indication factor (CIF) using the Eq.(5.2) for the bottom ash scraps of Cu, Al, Brass and Zn shown in sample set S2. 84
- Figure 5.12: Sorting statistics based on the measured CIF values of the scraps using a hi-low and a hi-low-int sorting method. 86
- Figure 5.13: (a) Calculated conductivity using Eq. (5.3) of the scraps of sample set S2 without calibration constant D_{metal} . (b) Calibrated conductivity of the scraps of sample set S2 using the average calibration constant D_{metal} from Figure 5.9c. 88
- Figure 5.14: (a) Al scraps and (b) Cu scraps with complicated shapes, including cavities and contortions. The next panels show pre-processed and flattened particles of: (c) Cu scraps. (d) Al scraps. (e) Brass scraps and (f) Zn scraps. 90
- Figure 5.15: Measured conductivity of the pre-processed and flattened scraps of Figures 5.14(c), (d), (e) and (f) using the standard conductivity meter, model PSIG001. 90

Table of Contents

Acknowledgements	i
Declaration by candidate	iii
Declaration by candidate on corrections	iv
Co-supervisor's certification	v
Principle supervisor's certification	vi
Summary	vii
List of publications from this research to date	ix
List of acronyms and symbols	x
List of Tables	xii
List of Figures	xiii
Chapter 1: Introduction	1
1.1 MSWI bottom ash	1
1.2 Background of the thesis	4
1.3 The role of sensors in traditional sorting technique	7
1.4 Hybrid sorting technique and quality control	10
1.5 The goal of this thesis	12
1.6 The methodology of this research	13
1.7 Outline of this thesis	13
References	15
Chapter 2: Metal Grade Measurement Method and Hybrid Sensor	17
2.1 Introduction	17
2.2 Metal grade detection method	19
2.3 Sample materials	19
2.4 Hybrid sensor	21
2.4.1 Infrared sensor(IRS)	22
2.4.2 Electromagnetic sensor (EMS)	23
2.5 Characterization of the hybrid sensor	24
2.5.1 Limit sensitivity and detection threshold	24
2.5.2 Repeatability and count correction parameters (C^{IRS} , C^{EMS} , $C1$)	25
2.6 Verification of metal grade detection method	28
2.7 Case study: MSWI bottom ash	29
2.7.1 Size distribution and signal strength	29

2.7.2 k value and metal grade	30
2.7.3 Operational statistics	32
2.8 Conclusions	33
References	34
Chapter 3: Functionality Analyses of the Hybrid Sensor	35
3.1 Introduction	36
3.2 Materials and method	37
3.2.1 Sensor and ECS	37
3.2.2 Sample materials	39
3.3 Laboratory test results	40
3.4 In-situ test results	44
3.4.1 Dry feed bottom ash	45
3.4.2 Wet feed bottom ash	48
4. Conclusions	49
References	50
Chapter 4: Eddy Current Belt Sensor-Conductivity approach	52
4.1 Introduction	53
4.2 Applied field and setup	54
4.3 Magnetic moment of the reference particle	56
4.4 Conductivity approach for the belt sensor	58
4.5 Detected field of the z receiver	61
4.5.1 Detected field response	61
4.5.2 Conductivity indication factor (CIF)	64
4.6 Conclusions	65
References	66
Chapter 5: Experimental Results of the Eddy Current Belt Sensor	67
5.1 Details of the belt sensor and experimental setup	67
5.2 Sample materials	71
5.3 Experimental results	72
5.3.1 Operating frequency of the sensor	72
5.3.2 Calculation of the primary magnetic fields B_{1zsum} and B_{2zsum}	75
5.3.3 Conductivity indication factor (CIF) of pure sample set S1	79
5.3.4 A_{eff} of the particles of pure sample set S1	81
5.3.5 Conductivity indication factor (CIF) for bottom ash scraps	82

5.3.6 Sorting methodology and sorting statistics of the bottom ash scraps..	84
5.3.7 Conductivity of the scraps	86
5.4 Discussions	91
5.5 Conclusions	95
References	97
Chapter 6: Conclusions and Recommendations	98
6.1 Conclusions	98
6.2 Recommendations	101

Chapter 1

Introduction

It is a common practice in society that the people have their own styles and ways to store and reuse commodities, materials and resources. Now days material recycling demands vaster attention in the society for sustainable management of resources, conservation of energy as well as protecting ecological balance. Scientific management of different kind of wastes and necessity of proper recycling methods are considerably focusing ecologist, environmentalist, scientists and technologists altogether into a common platform for finding solutions in the interest of majorly saving the primary resources, making economically inexpensive quality products and reducing landfill to avoid dilapidation of green ecosystem. From global perspective of municipal solid waste (MSW) generation, the amount of MSW increases rapidly that would reach at 27 billion tons in 2050 from 13 billion tons in 1990 and presently more than one billion tons of MSW are discarded worldwide, although these numbers are uncertain and may vary from region to region (Karak et al., 2012; Vergara and Tchobanoglous, 2012; Sharholy et al., 2008). Moreover, urbanization and industrialization are escalating with the increase of world population that significantly upraises the use of e-waste or waste of electronic and electrical equipment (WEEE). Literature study shows the amount of WEEE in MSW is about 8 wt% where the content including iron, copper, aluminum, gold and other metals in WEEE is over 60 wt% with 0.2 tons of copper in one ton of e-waste and 1g of gold in a personal computer of recent generation (Widmer et al., 2005).

1.1 MSWI bottom ash

Municipalities of developed nations have taken enough legislation and a number of measures for recycling of valuable materials from waste as well as minimization of undesirable impacts of waste disposal in society. The MSW majorly contains both complex degradable biogenic and non-biogenic materials. The complex non-biogenic part of the solid waste possesses majorly glass, stone, ceramics, plastics, paper, wooden stuffs, demolished building concrete, electronic products and various goods containing lots of different metals. Figure 1.1 shows a

typical flow diagram of MSW recycling for material upgradation and recovery from some generation sites to the end of a typical waste treatment plant using eddy current separator (ECS) technology. Actually this is just an overview to see how advance waste processing and material recycling work in developed part of the world. Different kinds of companies with privet or public-privet partnership collect waste from different parts of society and sometimes they directly process the collected waste for energy recovery and material separation or the collected waste are sold out to a third party who works for further processing of waste for material recovery.

The processing and transformation of MSW is an art of energy recovery and material reuse in municipalities of many developed nations. Different types of technologies are used for the conversion and recycling of biogenic and non-biogenic materials in solid waste, where in Europe and Japan, incineration is the most popular technique for conversion of the MSW into heat and electricity which is one of the significant secondary source for energy solution in societal and environmental benefits (see Table 1 & Table 2, Vergara and Tchobanoglous, 2012). The incombustible residue after the incineration of the MSW is called as municipal solid waste incinerator (MSWI) bottom ash which is another complex materials containing a mix of organic and mainly inorganic materials as well as a significant secondary source of ferrous and nonferrous (NF) metals (ferrous \approx 10%, NF \approx 1%). It is notable here that the recycling of nonferrous metals from MSWI is profitable for saving the world resources as well as advantageous for the environment too. For example the recycling of aluminum cans requires 95% less energy and reduces emission of 95% greenhouse gas (GHG) as compared with the overall energy consumption scenario during the production process of raw aluminum from its natural source bauxite ore.

For technological adaptation the resulting MSWI bottom ash materials are sieved at different size fractions such as Size 1, Size 2 and etcetera although these are just symbolic representation of particle sizes in a crude way instead of telling the exact size in a plant. The different size fractions of the MSWI bottom ash are processed first by magnetic separation where the magnetic scraps of different materials majorly the iron and steel scraps are separated out. Afterwards the

aggregates are taken to a conveyor type eddy current separator (ECS) for upgradation of the NF scraps from the waste which is then called as ECS upgraded or concentrated NF fraction.

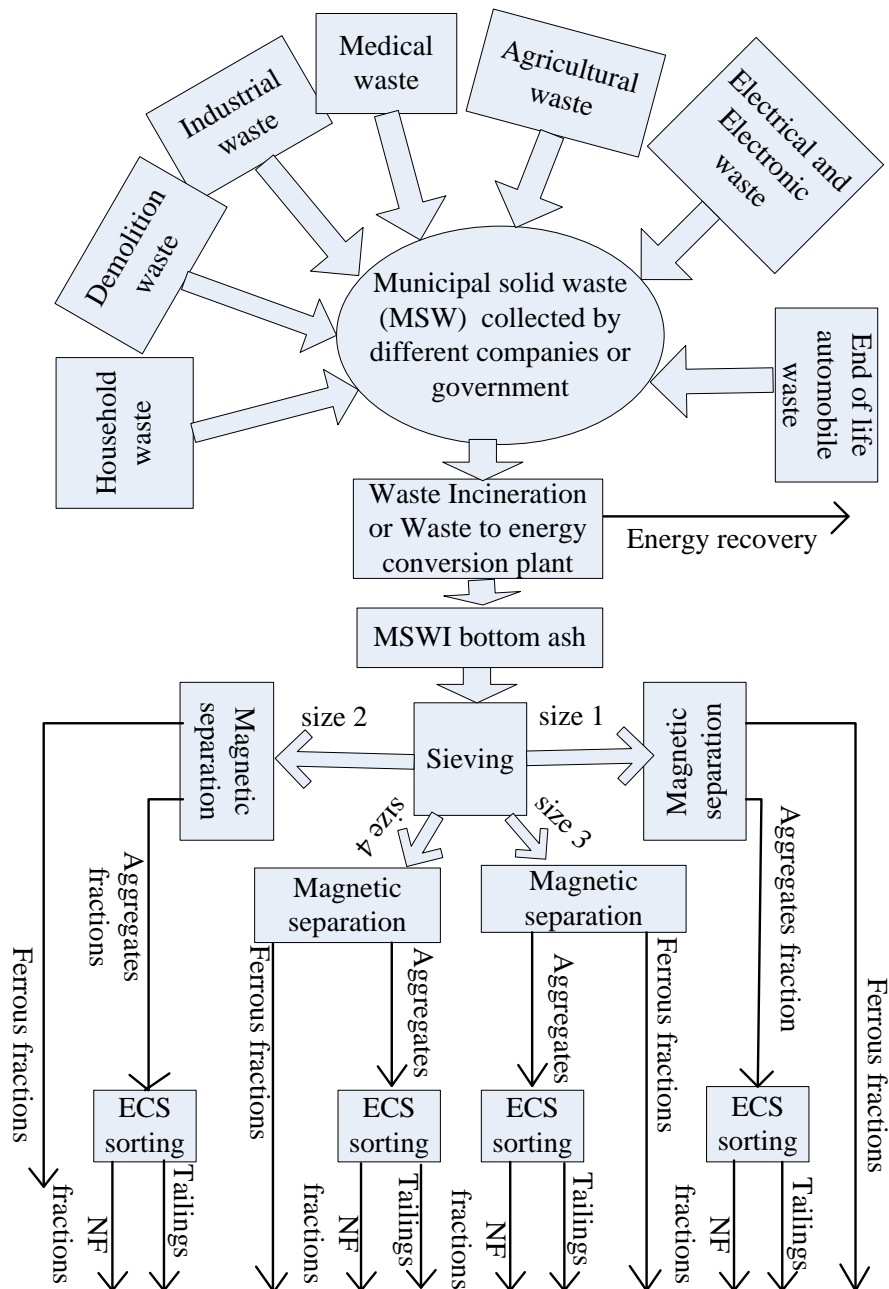


Figure 1.1: A typical flow diagram of municipal solid waste (MSW) recycling for material upgradation and recovery from various generation sites.

Figure 1.2(a) shows a typical naturally dried pile of MSWI bottom ash to be processed by an ECS in a plant where (b) shows the ECS upgraded moist NF fractions and (c) shows a mixer of manually analyzed NF metal contents from a subsample of (b). For manual analyses of NF metal contents the subsample is taken in a crusher that demolishes the nonmetal parts by producing fines and flattens the NF scraps of the sample. Therefore the crushed mixer contains demolished fines and flattened NF scraps which are then collected after sieving and removing the fines.

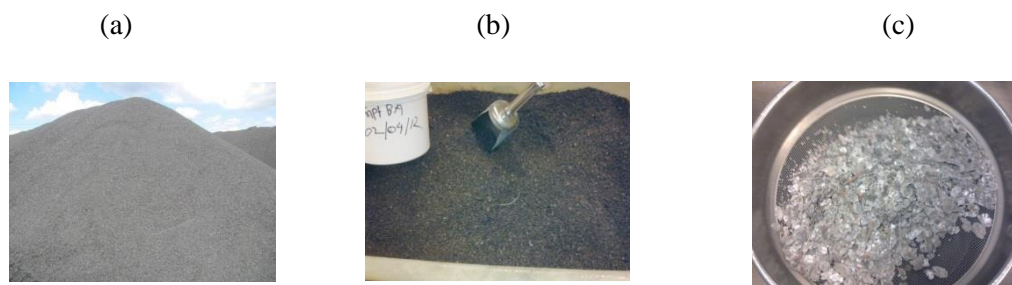


Figure 1.2¹: (a) A pile of naturally dried MSWI bottom ash, size fraction 0-6mm in a waste energy conversion plant that comes as a residue from an incinerator of a waste to energy conversion plant. (b) ECS concentrated moist NF fractions, size 0-6mm. (c) Manually analyzed NF metal contents from a subsample of (b).

1.2 Background of the thesis

Literature study shows that the bottom ash materials, size fraction up to 16mm is most relevant fractions which are concentrated to higher metal contents using an eddy current separator (ECS) (Gillner et al., 2011; Grosso et al., 2011; Schlomann 1975). It is also quite convincing from a literature study that one or two pieces of jewelry gold can be recovered by recycling per ton of MSWI bottom ash, size fraction 2-6mm (Muchova et al., 2009) although this conclusion may vary in some extent from region to region. The nonferrous metal content of municipal solid waste incineration (MSWI) bottom ash includes a significant

¹All sample materials and photographs presented in this chapter are prepared at Resources and Recycling Laboratory, Faculty of Civil Engineering and Geosciences, Delft University of Technology, Netherlands.

amount of heavy metals, such as Cu, Pb, Ni, Zn, and an even larger amount of light metals, mostly Al alloys (Kuo et al., 2007). From recycling point of view the MSWI bottom ash materials form a secondary source of valuable non-ferrous metals such as Cu, Al, Zn, Brass, Pb and Ni (Shen and Forsburg, 2003). For the recovery of the nonferrous metal contents from the MSWI bottom ash the eddy current separator (ECS) relies on a technique where a conveyor belt feeds the input bottom ash at a rate up to 15 ton/h to a magnetic field generated by rotating permanent magnets (Settimo et al., 2004).

Figure 1.3 (a) shows a sketch of a typical set up of an ECS machine for the separation of the nonferrous metal contents from the nonmetal/mineral fractions in the bottom ash as it is also mentioned in a publication of this research (Rahman and Bakker, 2013). This research primarily focuses on the issues for the nonferrous metals recovery from the MSWI bottom ash, size fraction <6mm, using traditional eddy current separator (ECS). Effective separation efficiency of an ECS for the small bottom ash particles, size fraction <6mm, remains unsatisfactory as it suffers from significant losses of nonferrous metals specifically the more valuable heavy metals (Hu et al. 2011, Hu and Rem, 2009; Rem et al., 2004) due to the fact that the magnetic force exerted by the ECS on the metal particles goes rapidly down with particle size (Braam et al., 1988, Schloemann, 1975), but also shape, electrical conductivity and mass density play a role (Zhang et al., 1999). As a result, metal particles show a wide fan of trajectories due to the spread in material properties and dimensions. On the other hand the mineral particles also display a fan of trajectories due to the variations in their ballistic properties, but the fan of the mineral particles is of course closer to the ECS drum.

Regardless of the advances in the development of eddy current separator (ECS) still the recovery of the nonferrous metals, size fraction <6mm is scant that needs technological mitigation and method for optimum recovery and quality control of the NF fractions of the ECS products (Rem et al., 2004, Settimo et al., 2004). As the bottom ash materials is very complex and it is not unusual that many metal products get contaminated with nonmetal/mineral particles and oxidation of some metal particles may degrade the true electrical properties of the

particles during the incineration process. Consequently depending on the composition of feed materials and also moisture content the trajectories of metal and mineral particles may overlap and the splitter position always plays a crucial role for effective separation of the metals and minerals. The effectiveness of the material separation may be monitored and improved by the availability of real-time information on the waste feed and output products and continuous adjustment capability of the splitter settings of the ECS machine. Several hybrid technologies, i.e. which employ a combination of different sensor principles, have been proposed for metals sorting (Koyanaka and Kenichiro, 2010; Mesina et al., 2007) or for characterisation of metal-composites (Helseth, 2011).

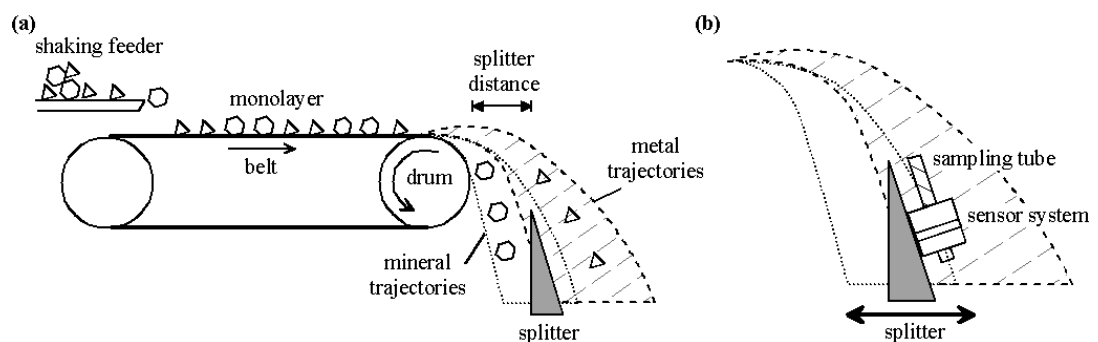


Figure.1.3: (a) Principle of ECS separation. Trajectories of small nonferrous metal and mineral particles overlap and the splitter must be set in a compromise. (b) The sensor system measures metal grade and amounts of metal and mineral particles, allowing for online quality assessment or online splitter control.

Till the commencement of this study no practical method does exist which could be implemented for the online quality control of the upgraded NF fraction in ECS products, size fraction <math><6\text{mm}</math>, which is the main key issue involved in this study what could be dealt with the implication of an inline hybrid sensor unit with the ECS i.e is shown in Figure 1.3(b). A qualifier for the adjustment of the splitter settings of the ECS is the metal grade of the NF concentrated stream which can be detected using a hybrid sensor that could facilitate to produce a feedback mechanism for automatic adjustment of the splitter settings although still now the splitter settings is commonly fixed up by a manual operator in the plant.

1.3 The role of sensors in traditional sorting techniques

Traditional pre-melt physical separation techniques are mostly mechanical type and manual operated. In this section author would like to present a short brief of traditional and emerging pre-melt physical separation techniques to the readers to give an impression about why the sensor sorting of waste is more advantageous over the traditional one. In all recycling techniques the wastes are shredded and sieved in advance at different size fractions for the requirements of the technological adaptation of the waste. Afterwards specific size fraction of the shredded waste, sometimes deliberately followed by a pre-processing step such as washing, wetting, drying and etcetera is conveyed to a chain of specific traditional technologies for physical separation by concentrating the different types of materials into high grade products and low grade tailings. For example in a typical aluminum sorting from automobile scraps, the magnetic method separates ferrous metals from the waste stream, then air sorting method blow out the lighter non-metallic particles such as plastics, foams from the stream that results a concentrated mixer of different nonferrous metals. After that the concentrated nonferrous fraction is processed by sink/float method for further physical separation of heavy and light NF metals and finally spectroscopic method is used for separation of Al scraps (see Figure 2. Gaustad et al., 2012).

Table 1.1 shows the list of a few traditional and emerging recycling techniques where most of the emerging technologies are sensor based that can facilitate online quantitative analyses and quality control of the separated yields with a luxury option for system automation. The infrared sorting system works for the separation of different kind of plastics based on absorption or reflection spectroscopic analyses of the materials whereas the color sorting system is one kind of hand picking system works based on the identification of visible colors of the waste particles on a conveyor.

Table 1.1: A list of traditional and sensor sorting techniques.

	Name of the technologies	Type	Online quality control	Major applications
Traditional Technologies	Magnetic separation	Mechanical	Not available	Magnetic fractions sorting.
	Air separation	Mechanical	Not available	Metals sorting from light non-Metallic particles.
	Eddy current separator (ECS)	Mechanical	Not available	NF metal separation from MSWI bottom ash, Al Can sorting.
	Sink float / heavy media separation	Mechanical	Not available	Heavy metal separation from light NF.
Emerging technologies	Near infrared spectroscopy	Sensor	Applicable	Different types of polymer separation.
	Color sorting/ hand picking	Sensor	Applicable	Relatively colorful object sorting.
	XRF sorting	Sensor	Applicable	Non-magnetic metals, ceramic glass and meatball sorting.
	LIBS	Sensor	Applicable	Metal sorting, concrete sorting.

On the other hand X ray fluorescence spectroscopy (XRF) and laser induced breakdown spectroscopy (LIBS) use X ray and high power laser source to illuminate the moving waste particles, respectively. In XRF system the secondary atomic spectra is recorded and analyzed by a high resolution spectrograph for the identification and composition analyses of target materials. In LIBS a diminutive portion of a moving particle is ablated to produce plasma from which characteristic emission is recorded for the identification and composition analyses of target materials. Another mechanical type of sorting technology is magnetic density separation (MDS) i.e. is basically a density separation like sink/float separation but employs magnetic liquid for separation of different kind of plastics and diamond from gangue (Rem et al. 2009, Wijmans et al. 2009).

However, the sensor based emerging techniques stance comparatively stronger attention to provide efficient separation of the materials as well as additional information for quantitative and qualitative analyses that offer lots of versatility and innovation for sustainable resource management. Although it is notable that the waste materials are so complex and not shiny enough, contain lubricant, paints, coating of different foreign materials and become more complicated after incineration. These are a couple of dilemmas and challenges for accurate sorting of the materials using the emerging technologies too. In addition a few emerging technologies like LIBS (laser induced breakdown spectroscopy) needs singulated feed of the particles that process the particles one by one along a line which is less preferable than the traditional high throughput mass feed system using a wide conveyor belt i.e. why unlikely still shipping of significant amount of metallic waste scraps increases from the developed world to the developing countries where hand picking and sorting of materials by color still remain cheaper and profitable (Gaustad et al., 2012). And again the hand picking and sorting technique fetches safety issues to the health of the working people in the operating plants, it is because, the complex waste may contain some sort of hazardous materials that can outbreak the public health through skin contact, especially through cuts and abrasions or through contact with the eye's mucous membrane, injection, through sharps injuries, absorption through hand-to-mouth contact (commonly experienced when eating, drinking or smoking) and inhalation through the lungs (Vergara and Tchobanoglous, 2012).

As the waste materials are so complex hence it is more rational for the implication of different kind of sensor units that results the sorting technique as a hybrid recycling technique. For example a color sorting system sometimes may not work properly if the color of the waste particles is not shiny enough then in addition a shape discrimination unit can be useful for making a decision more accurate from statistical pre-knowledge of the particle's shape and the type of the materials. Either on purpose inclusion of an induction sensor or a set of induction sensors with the XRF, camera and the LIBS system can improve the sorting accuracy and off course can widen the scope of the technologies.

1.4 Hybrid sorting technique and quality control

Either purely sensor sorting or addition of a sensor with the traditional sorting system is an emerging sorting system which is called as hybrid sorting system in this study. Figure 1.4 shows a general flow diagram of a hybrid sorting system that majorly composed of:

- A traditional sorting system with set parameters adjustment facilities;
- A set of online sensors attached with the traditional system;
- A DAQ module for signal acquiring from the sensors;
- Methods or algorithms for quality control or sorting decisions;
- A central processing unit for online data analysis and processing;
- A controller for producing control signals for the adjustment of machine settings for quality control or sorting.
- A display and storage unit for accumulating the processing data for statistical analyses of daily or weekly or yearly performance of the recycling plant.

The hybrid system is basically a closed loop system where the set of online sensors makes exclusive differences with the traditional one. The purposes of the online sensors are to detect some qualitative or quantitative parameters of a particle in a stream where the parameters can be either single type or a combination of multiple types from the followings:

- Material properties such as density, ductility, hardness, odor, electrical conductivity, magnetic permeability and etc.;
- Some physical features such as shape, size and color;
- Optical properties such as optical transmissivity or reflectivity;
- Spectroscopic properties such as absorption and emission spectra;
- Supplementary parameters such as moisture level, level of dust contamination and etcetera.

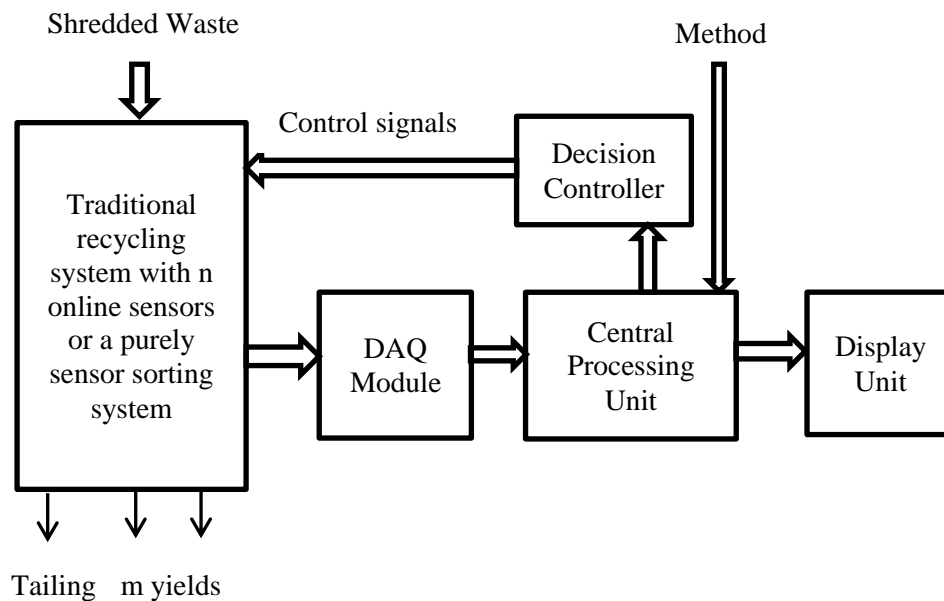


Figure 1.4: A flow diagram of pre-melt hybrid physical separation system.

The detection of a specific parameter can be done either before separation or after separation that depends on the adopted methods or algorithm for quality control of the output products. However, the use of a properly designed hybrid recycling system may achieve the followings:

- Improved sorting efficiency;
- Online quality control of the recovered materials;
- Quantitative or semi-quantitative analyses of the separated high grade products and tailing parts;
- Substitution of manual control to automation;
- Reduction of the likelihoods of the contamination of the hazardous materials directly to the environment.
- Enhanced safety for the working people in the waste processing plants.

1.5 The goal of this research

First the goal of this research is to develop a hybrid sensor for counting the nonferrous metal and non-metal particles in the ECS concentrated stream of the bottom ash materials. The aim of the hybrid sensor is to measure online metal grade (G) of the stream from these count data. The hybrid sensor in this regard focuses on principle, design and characterization of the sensor as well as on the development of a method for the measurement of the metal grade in the stream. Afterwards the functionality of the hybrid sensor with an ECS is tested in laboratory as well as in situ. The purpose of the implication of the hybrid sensor with the ECS is to analyze the online functionality of the sensor for the quality control of the NF metal concentrated bottom ash materials by ECS as explained in the Fig. 1.3.

Second, this hybrid sensor research is extended on the development of an eddy current belt sensor that leads a fundamental research for identification of nonferrous metal scraps on a conveyor. In order to do that a conductivity model for material classification is developed based on magnetic moment resulting from the induced eddy current in a particle on a conveyor. For that a disk model based on advanced eddy current theory is extended by an approximation to match the measured response of a particle of different shapes e.g. disk block, square plate, square block, rod and cylinder each of Cu, Al and Brass. This facilitate a new parameter called here conductivity indication factor (*CIF*) that can be used experimentally for the identification of different particles of different materials such as Cu, Al and Brass on a conveyor. Moreover, as an application of the belt sensor a representable amount of MSWI bottom ash, 6.5mm<sieve size <15mm is also tested to observe the performance of the sensor.

1.6 The methodology of this research

This thesis presents an applied research in its first part that focuses on the technological innovation and development of a hybrid and an eddy current belt sensors. The methodology consists of the analysis and design, experimental construction and characterization of the sensors in terms of detection sensitivity and data quality in terms of repeatability and accuracy, based on measured responses of the sensor. The data quality and understanding of results is facilitated by using both synthetic as well as real bottom ash sample materials. A method for the measurement of metal grade using the hybrid sensor is simulated and verified with synthetic sample materials. The method employs a mathematical technique that introduces a k -parameter, metal and nonmetal count data from the sensor for a specified sampling time from where the metal grade is calculated, where the parameter k is the average particle mass ratio between nonmetal and metal. The bottom ash sample materials, size fraction <6mm are collected from a bottom ash waste processing plant. Afterwards for analyzing the performance of the hybrid sensor a set of measurements is carried out as functionality tests with the full-scale ECS in the laboratory as well as situ where the laboratory offered controlled conditions and the situ tests are driven at full scale operational conditions for the ECS.

On the other hand in second part a fundamental research is presented where an approximate conductivity approach is formulated based on the eddy current principle for the identification of the different metals on a conveyor. This so-called eddy current belt sensor was designed, constructed and characterized in the laboratory. A set of synthetic samples S1 is tested with the belt sensor for the validation of the conductivity approach. Moreover as an application of the belt sensor a sample set S2 prepared from MSWI bottom ash materials is also tested.

1.7 Outline of this thesis

This thesis encompasses six chapters including chapter introduction and chapter conclusion. The chapter introduction deals majorly with the thesis background, sensor based and traditional sorting technologies, thesis goal as well as the research methodologies followed in this dissertation.

The Chapter 2 which is a published article from this research that focuses on the basic principle, design, construction and characterization of the developed hybrid sensor. The sensor characterization mainly encapsulates the sensitivity, capacity and data quality in terms of repeatability and accuracy of the sensor. A mathematical model for the measurement of online metal grade of a stream of particles is formulated in this chapter where the model takes the metal and total particle count data from the developed hybrid sensor and relates the count data with experimentally determined pre-knowledge of the k parameter of the particles for calculation of the metal grade of the stream. Model verification with synthetic sample of known k parameter and measured data with the test of MSWI bottom ash particles as an application of the sensor are presented in this chapter too.

The Chapter 3 is also a published article from this research that presents an immediate application of the developed hybrid sensor which deals with online functionality analyses of the sensor. For that online application the hybrid sensor is installed in laboratory and in-situ with the implication of an ECS. In the functionality tests the performance of the sensor is investigated for the measurement of the online metal grade of the ECS concentrated bottom ash stream with the pre-knowledge of the k parameter. The sensor performance is also discussed in this chapter and a method for quality control of the bottom ash stream is suggested in associated with the measured grade, non-metal count and splitter settings of the ECS.

The Chapter 4 deals with the deduction of the governing expressions of a belt sensor based on a crude approximation of advance eddy current theory of a particle of disk shape that proposes a model based on conductivity approach for the identification of different NF metal particles of different shapes on a conveyor. Accordingly an expression for the parameter CIF is deduced here in this chapter. Afterwards once the material CIF is known then an expression of conductivity σ of the particle is also presented for the calculation of the conductivity of the particle.

Subsequently the Chapter 5 deals with the design, construction, magnetic field simulation, characterization of the eddy current belt sensor as well as the experimental results using synthetic sample set S1 and MSWI bottom ash sample set (S2). The synthetic set S1 contains known type of particles of Cu, Al and Brass materials of different shapes and the bottom ash sample set S2 is a representable amount of nonferrous scrap metals of different materials e.g. Cu, Al, Brass and Zn collected from same batch of MSWI bottom ash materials. The synthetic set is used for validation purposes of the conductivity approach whereas the bottom ash sample set S2 is used as an application of the belt sensor. Finally the Chapter 6 focuses on the overall conclusions and recommendations for further advancement of this research.

References:

- Braam, B.C.**, van der Valk, H.J.L., Dalmijn, W.L., 1988. Eddy-Current Separation by Permanent Magnets Part II: Rotating Disc Separators. *Resources, Conservation and Recycling*, 1, 3-17.
- Gaustad G.**, Olivetti E. & Kirchain R. 2012, Improving aluminum recycling: A survey of sorting and impurity removal technologies, *Resources, Conservation and Recycling* 58, 79 – 87.
- Gillner, R.**, Pretz, T., Rombach, E., Friedrich, B., 2011. Non-ferrous metal potential in bottom ashes of waste incinerators [NE-Metallpotenzial in Rostaschenaus Müllverbrennungsanlagen], *World of Metallurgy - Erzmetall* 64 (5), 260-268.
- Grosso, M.**, Biganzoli, L., Rigamonti, L., 2011. A quantitative estimate of potential aluminium recovery from incineration bottom ashes, *Resour. Conserv. Recycl.* 55, 1178– 1184.
- Helseth, L.E.**, 2011. Contactless hybrid sensor for simultaneous detection of light reflectance and eddy currents, *Sens. Actuators, A*, Article in press.
- Hu, Y.**, Bakker, M.C.M., de Heij, P.G., 2011. Recovery and distribution of incinerated aluminium packaging waste, *J. Waste Manag.* 31, 2422–2430.
- Hu Y.**, Rem P. 2009, Aluminium alloys in municipal solid waste incineration bottom ash. *Waste Management Res.* 27, 251-257.
- Karak T**, Bhagat R. M. & Bhattacharyya P. 2012, Municipal Solid Waste Generation, Composition and Management: The World Scenario, *Critical Reviews in Environmental Science and Technology* 42,1509-1630, DOI: 10.1080/10643389.2011.569871.

- Koyanaka, S.**, Kenichiro Kobayashi, K., 2010. Automatic sorting of lightweight metal scrap by sensing apparent density and three-dimensional shape, *Resour. Conserv. Recycl.* 54, 571–578.
- Kuo, N.W.**, Ma, H.W., Yang, Y.W., Hsiao, T.Y., Huang, C.M., 2007. An investigation on the potential of metal recovery from the municipal waste incinerator in Taiwan, *J. Waste Manag.* 27, 1673–1679.
- Mesina, M.B.**, de Jong, T.P.R., Dalmijn, W.L., 2007. Automatic sorting of scrap metals with a combined electromagnetic and dual energy X-ray transmission sensor, *Int. J. Miner. Process.* 82 (4), 222-232.
- Muchova L.** Bakker E. Rem P. 2009, Precious Metals in Municipal Solid Waste incineration bottom ash, *Water Air Soil Pollute: Focus* 9, 107–116.
- Rahman Md. A.**, Bakker M. C. M., 2013, Sensor based control in eddy current separation of incinerator bottom ash, *Waste Management* 33, pp.1418-1424.
- Rem P.**, Solaria V. & Maio F. D., 2009, High-purity products from plastic waste: the W2plastics project, *Environmental Engineering and Management Journal* 8 (4), 963-966.
- Rem P.C.** De Vries C. Van kooy L. A. Bevilacqua P. and Reuter M. A. 2004, The Amsterdam pilot on bottom ash, *Minerals Engineering* 17, 363–365.
- Schlomann, E.**, 1975. Separation of non-magnetic metals from solid waste by permanent magnets. I., Theory., *J. Appl. Phys.* 46, 5012–5021.
- Settimo F.**, Bevilacqua P., Rem P. 2004, Eddy current separation of fine nonferrous particles from bulk streams, *Physical Separation in Science and Engineering* 13 (1), 15–23.
- Sharholly M.**, Ahmed K., Mahmood G. & Trivedi R. C. 2008, Municipal solid waste management in Indian cities – A review, *Waste Management* 28, 459–467.
- Shen H.** & Forssberg E. 2003, An overview of recovery of metals from slags, *Waste Management* 23, 933–949.
- Vergara S. E.**, Tchobanoglous G., 2012, Municipal Solid Waste and the Environment A Global Perspective, *Annu. Rev. Environ. Resour.* 37, 277–309.
- Weijmans F.**, Bakker E. & Rem P., 2009, Magnetic density separation of diamonds from gangue, *Environmental Engineering and Management Journal* 8 (4), 981-984.
- Widmer R.**, Krapf H. O., Khetriwal D. S. , Schnellmann M., Boni H, 2005, Global perspectives on e-waste, *Environmental Impact Assessment Review* 25, 436–458.
- Zhang, S.**, Forssberg, E., Arvidson, B., Moss, W., 1999. Separation mechanisms and criteria of a rotating eddy-current separator operation. *Resources, Conservation and Recycling* 25, 215–232.

Chapter 2

Metal Grade Measurement Method and Hybrid Sensor

This chapter presents a method for the measurement of the average metal grade G in a stream of falling solid waste particles. The contents of this chapter were published from this sensor research (Rahman and Bakker, 2012) and presented here with minor change. To verify the method a hybrid sensor is developed in this research. The method utilizes metal and non-metal particle count data from the developed hybrid sensor and relates the count data with the pre-knowledge of the average particle mass ratio (k) between metal and non-metal to provide the metal grade of the stream. Accordingly the chapter focuses on the sample materials, construction details and characterization of the hybrid sensor in terms of its sensitivity, repeatability and correction factors (C^{IRS} , C^{EMS} , CI) of the sensor using a representable amount of known synthetic sample materials of different values of k i.e are $k=0.24, 0.54, 1.23$ and 2.69 . Afterwards a representative amount of bottom ash materials, sieve size $<6\text{mm}$ was tested. The sensor performance was obviously repeatable and the error for the detection of the metal grade of falling bottom ash particles was $\pm 2.4\%$.

2.1 Introduction

Referring to the Figure 1.3b from Chapter 1 i.e. a hybrid sensor was introduced for online quality control of the recovered materials. In order to do that an important qualifier is the metal grade of the concentrated nonferrous metal product, which is commonly analysed by taking samples to the laboratory which is a time consuming and costly technique. Instead, in this work it is proposed to measure the metal grade in-line using a hybrid sensor system. The detected grade

may then be used either for quality control purposes or for real-time control of the ECS settings to improve recovery and grade of the metal concentrated product.

In this chapter a hybrid sensor system is proposed for grade measurement of a fine-grained particles stream. This technique is based on particles counting, which is achieved using a combination of an optic and an electromagnetic principle. Special attention went to the design of the electromagnetic sensor in terms of sensitivity for small particles with low conductivity and robustness against noise and interference. These conditions are typically found in the targeted ECS bottom ash application and plague commercial metal detectors and counters. Typical sources of interference are the electromagnetic fields produced by the rotating magnets of an ECS and ambient electromagnetic interference picked up by the coils. Moreover, the proximity of steel plating to the sensor is a source of offset in its signal output but it becomes even worse if the plates vibrate, which is unavoidable in practical large-scale recycling operations. These issues were dealt with using a balanced, high-frequency design that is sensitive within its centre through which the particles are fed, yet easily shielded from any outside interference by means of no more than a thin aluminium shield. Another advantage is that it produces an amplitude modulated signal, which allows for effective electronic suppression of noise interference in signal carrying cables.

Using synthetic samples the fundamental sensor properties such as sensitivity, reproducibility and influence and corrections for feed rate dependent factors are reliably determined and explained. As a complementary material and an important field of application bottom ash is used, where care is taken to use only material from same batch. The bottom ash presents a case study for the hybrid sensor under conditions where there is no accurate a-priori information about the physical properties and material composition of the sample. To eliminate uncertainty in the particles feed statistics all input materials are fed from the same feed height using the same vibrating feeder.

2.2 Metal grade detection method

The average metal grade of a representative number of particles from the waste particles stream is calculated from the sensor counts and the given average particle mass ratio k between non-metal and metal particles. The metal grade of the waste stream is from here on denoted as G , while m is the average particle mass and N^{IRS} , N^{EMS} are the sensor counts. A count correction factor is introduced for each sensor in view of the chance that it misses some particles, mainly due to particles falling simultaneously through the sensor. The metal grade may now be related to the hybrid sensor measurements as follows,

$$G = \frac{N^{EMS}C^{EMS}m^{metal}}{(N^{IRS}C^{IRS} - N^{EMS}C^{EMS})m^{non-metal} + N^{EMS}C^{EMS}m^{metal}} = \frac{Z}{(C1-Z)k+Z} \quad (2.1)$$

The Z ($0 < Z < 1$) denotes the ratio of sensor counts, $C1$ the ratio of sensor count correction factors and k the ratio of average particle masses, according to

$$Z = N^{EMS}/N^{IRS}, \quad k = m^{non-metal}/m^{metal}, \quad C1 = C^{IRS}/C^{EMS} \quad (2.2)$$

The count correction factors (C^{IRS} , C^{EMS}) and k can be determined in a calibration test using particle mixtures of known composition. For that purpose it is also useful to express Z directly in terms of the grade G .

$$Z = kGC1/(1 + Gk - G) \quad (2.3)$$

2.3 Sample materials¹

To test the sensor design, synthetic samples were prepared that allow for accurate control over the size, shape and homogeneity of the particles, as well as accurate control over the grade and number of particles in the used sample. To verify Eq. (2.1) these samples were prepared as a homogeneous mix of sand and either Cu or Al particles within specified size ranges to realize various values of k .

¹All sample materials presented in this chapter are prepared at the Resources and Recycling Laboratory, faculty of Civil Engineering and Geosciences, Delft University of Technology, Netherlands.

Table 2.1 shows the prepared set of four samples of each 100 g with $k = 0.24$, 0.54, 1.123 and 2.69. Figure 2.1a shows two such subsamples. Initially, each synthetic sample contained a fixed amount of 10 g metal after which the desired grade can be lowered by cumulative addition of sand. In this fashion eight grades were produced from 80% down to 10%. These values of k for synthetic samples are deliberately chosen so that the sample will be comparable with bottom ash materials. For the case study a sample of fresh bottom ash materials size fraction 0-10 mm with measured moisture content 7.1% was taken from the metal-concentrated product of an eddy current separator (ECS), where very few of coarse particles of size +6mm were an exception and those were filtered out by sieving at <6mm. The bottom ash materials are so complex that contains fines (<1mm), slag, sand, glass and nonferrous metals (e.g. Cu, Al, Brass, Zn) as well as some sporadic traces of organic matter (Muchova et al. 2009, Rem et al. 2004, Grosso et al. 2011). However, this means it does not contain any ferrous particles while the non-ferrous metal grade was thought to lie between 10-40% according to the ECS operator. Figure 2.1b shows a small subsample from this bottom ash.

Table 2.1: Four k -values using sand-metal particles mixtures.

Sand size range	Metal size range	Metal particles	
		k	
[mm]	[mm]	Cu	Al
2 - 3	2 - 3	0.54	1.23
3 - 4	2 - 3	-	2.69
3 - 4	5 - 6	-	0.24

(a)

(b)



Figure 2.1: (a) Synthetic sample material and (b) ECS concentrated bottom ash.

2.4 Hybrid sensor²

The hybrid sensor composed of two different sensors, namely first infrared sensor (IRS), second electromagnetic sensor (EMS). A schematic of the proposed hybrid system with the dataflow from its two sensors is shown in Figure 2.2a. The two sensors are centred on a vertical PVC tube (70 mm diameter) that guides the particles. The top section houses an infrared sensor (IRS) and the bottom an electromagnetic sensor (EMS). The IRS counts all the particles in the falling waste stream and the EMS counts only the metal particles. The output signal from the IRS is mono polar and that from the EMS is bipolar in nature, which polarity depends on the magnetic and conductive properties of the metal particles. The signal processing unit takes the raw data from both sensors and calculates the particle counts and subsequently the count ratio (Z) between EMS and IRS counts.

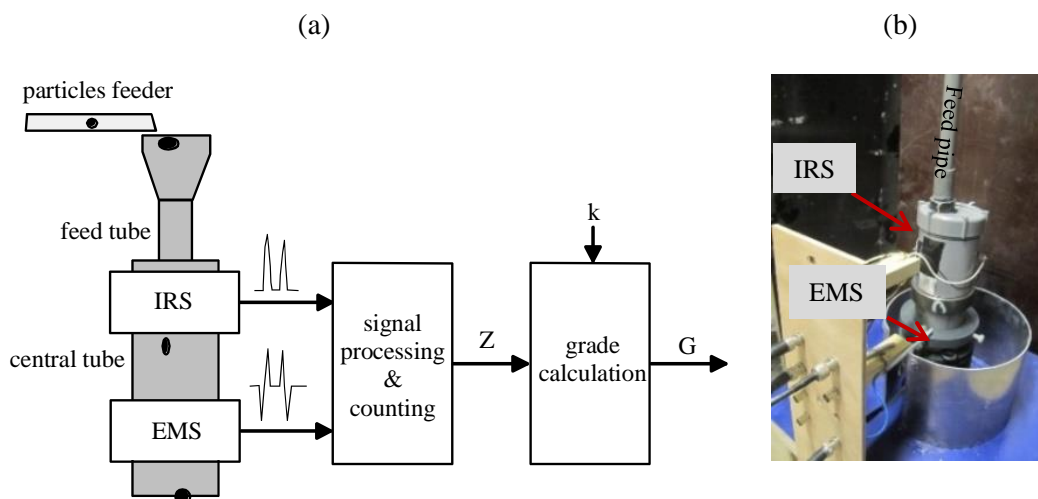


Figure 2.2: (a) The hybrid sensor main build-up and data flow and (b) the prototype unit with feed tube and an Aluminium shield for EMS.

The counting is preceded by setting a detection level. For a given average particle mass ratio k the metal grade of the falling waste stream can be calculated. Figure 2.2b shows the prototype where the waste particles are fed into the feed tube using a vibrating feeder. The height from the feeder to the IR sensor and to

²All experimental parts including design, construction and characterization of the presented hybrid sensor are completed at the Resources and Recycling laboratory, faculty of Civil Engineering and Geosciences, Delft University of Technology, Netherlands.

the top coil of the EMS is fixed at 600 mm and 720 mm, respectively. Actually the hybrid sensor system is aimed to deploy in a bottom ash processing plant in situ with a machine called eddy current separator (ECS) and these values are chosen in comprise with the real situation in situ and off course the sensitivity and throughput of each sensor are other two vital factors to fix these values. However, this results in a particle velocity of 3.4 m/s and 3.8 m/s at the centres of the two sensors, which velocity may get reduced by wall and particle-particle collisions inside the feed tube at higher feed rates.

2.4.1 Infrared sensor (IRS)

The IRS counts all the particles irrespective of the material type. Figure 2.3 shows the layout, which is based on the principle of detecting the shadow that a particle produces in a light fan beam. Using infrared at 950 nm has the advantage of decreased sensitivity to stray light during daylight operation. A single light emitting diode (LED) inside a slit emits a fan of infrared light towards a receiving diode array which is distributed along a part of the surface of the central tube. The array consists of only four diodes connected in parallel each of light-sensitive areas of $3 \times 3 \text{ mm}^2$. A PVC feed tube of 16 mm diameter is used to guide the waste particles towards the light fan. The spacing between the diodes leaves a chance that particles 1-2 mm (-1 mm particles are considered not important in this work) will not be detected. In fact these values are chosen by considering the real situation of ECS plant in situ where the developed sensor will be tested. In other words the fixation of these values is a compromise between sensor capacity and the real situation in situ. However, if particles are shiny enough, e.g. glass or metal, the light scatters to some degree which increases the chance of detection. Moreover, the sieve size of the -2 mm fraction (already a minor mass fraction) does not preclude that a substantial amount of particles are effectively longer than 2 mm which allows them to be detected anyway. Moreover in ECS the fine fractions (<1mm) is not so responsive for separation and that is why sieve sizes of >1mm will be tested and <1mm will be discarded (Rem et al 2000, Zhang et al. 1998,). The receiving diodes are connected in parallel, which keeps the required electronic circuitry and subsequent signal interpretation simple. Consequently, it creates the possibility that when several particles fall simultaneously they would produce only a single count. The probability of this count error is determined by

the vertical dimension of the receiving diodes (3 mm) and the method of feeding, but will always tend to increase with increasing particles feed rate.

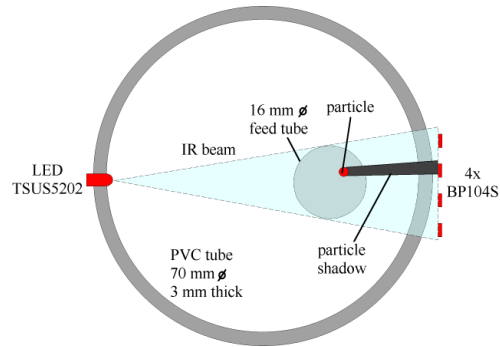


Figure 2.3: Layout of the infrared sensor (IRS).

2.4.2 Electromagnetic sensor (EMS)

The EMS is the complementary unit of the hybrid sensor and counts only the metal particles. The principle is based on a balanced, tuned transformer circuit in which the falling metal particles cause a disturbance resulting in amplitude modulated signals. Figure 2.4 shows the principle of the coils and the main data flow. The coils assembly consists of two bias coils of each 40 windings and a detector coil of 80 windings. The complete coil assembly is 61 mm high and is positioned on the central tube 120 mm below the IRS assembly. The effective vertical sensing length of the EMS is ~160 mm, taking into account the effect that the magnetic field extends outside the bias coils. These values are chosen experimentally by trial and error basis that the sensitivity of the sensor was sufficient for detection of +1mm metal particles. The excitation of the magnetic field is taken care of by the bias coils L_1 and L_2 that are connected in differential mode. An alternating bias current is supplied to the bias coils that produce two opposing magnetic fields B_1 and B_2 .

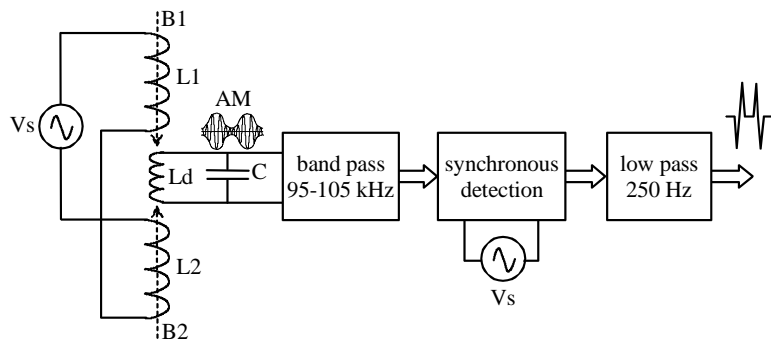


Figure 2.4: EMS detection principle and dataflow.

The thin detection coil L_d is centrally positioned, i.e. in the region where the opposing fields B_1 and B_2 cancel out. A capacitor C is connected in parallel with L_d to sensitively tune the EMS around the centre frequency of 100 kHz. This tuning produces a narrow-band, high frequency system that is insensitive to ambient noise and to adjacent metal surfaces, provided it is properly shielded for which a thin 1 mm aluminium shield proved quite sufficient (cf. Figure 2.2b). The voltage of the detection coil is mechanically tuned to zero to obtain balance. Then, if a conductive non-magnetic particle falls through the tube it produces an induction current which out-of-phase magnetic response causes an unbalance that is picked up by L_d . If a ferromagnetic particle falls through the tube it produces a strengthening of the magnetic flux, i.e. in-phase with the bias field, which also creates an unbalance that is picked up by L_d . Note that this results in two types of detected signal which are more or less 180 deg out of phase. A detected particle produces an amplitude modulated signal which is fed into a band pass filter for removing both low frequency and very high frequency noise picked up between the coil and the electronic unit. This cleaned signal is led into a synchronous detector and subsequently a low pass filter to produce the low-frequency output signal that can be used for counting. Note that the ferromagnetic and non-magnetic particles produce essentially oppositely phased signals, which allows for easy discrimination between the two types of metal if so desired.

2.5 Characterization of the hybrid sensor

2.5.1 Limit sensitivity and detection threshold

The limit sensitivity of the developed sensors here is related to the smallest sieve size range that still gives a detectable response above the noise. The limit sensitivity for the IRS proved to be 0.5-1 mm and for the EMS 1-2 mm. Based on this performance, and the fact that very small particles are of far less interest in metal recycling operations, further testing is limited to particles in the size fractions +1 mm by setting a threshold to the detected amplitudes. To determine the absolute threshold levels for both the synthetic samples and the bottom ash the size fractions 0.5–1 mm and 1–2 mm are fed through the hybrid sensor and the amplitude statistics were recorded. From the averages followed the thresholds listed in Table 2.2.

Table 2.2: Threshold detection voltage for +1 mm particles.

IRS [mV]		EMS [mV]	
synthetic sample	bottom ash	synthetic sample	bottom ash
188	180	7.01	6.00

2.5.2 Repeatability and count corrections parameters (C^{IRS} , C^{EMS} , CI)

The repeatability of the sensors is tested using synthetic samples at different feed rates. The feed rate was calculated by recording the feed time from start to stop where the total number of particles was known and a monolayer of the particles was maintained during the feed. A sample with 9.8% metal grade is prepared by homogeneous mixing of 1605 sand particles in the size fraction 2–4 mm and 300 Al particles in the size fraction 2-3 mm. Each test was repeated twice. Table 2.3 shows the data for the IRS and EMS for particle feed rate up to 39 per second. The repeatability of the sensor counts proves quite satisfactory with an average standard deviation of 10 particles (0.6%) for the IRS and 3 particles (1.1%) for the EMS. Using Eq. (2.2) the count correction ratio of the hybrid sensor calculated as $CI = 0.99$, 0.96 and 0.95 at particle feed rates of 8, 21 and 39 per second, respectively. Clearly, the individual count corrections increase faster with feed rate than their ratio, as the chance of simultaneously falling particles increases for both sensors. In order to measure the performance at higher throughputs the same synthetic sample of total 1905 particles (1605 sand + 300 metal) is used as well as a bottom ash sample. The higher feed rates may be of interest for practical sampling scenarios. A point was that it was easy to count by hand all the metal and non-metal particles in the synthetic sample, but for the bottom ash it was not.

Table 2.3: Repeatability test using a sample mixer of 1605 sand and 300 metal particles.

Input particles feed rate [s ⁻¹]	IRS					EMS					CI
	Measurement			std	C^{IRS}	Measurement			std	C^{EMS}	
	1	2	3			1	2	3			
8	1884	1883	1864	11	1.01	294	296	291	3	1.02	0.99
21	1843	1833	1849	8	1.03	286	281	276	5	1.07	0.96
39	1754	1746	1770	12	1.08	264	262	266	2	1.14	0.95
	Average:			10	1.04	Average:			3	1.08	0.96

To resolve that problem the bottom ash feed rate was increased from really slow, giving an assumed 100% certainty in counting, to quite fast while normalizing the IRS count by the maximum IRS count (say MaxCnt) that is obtained at the slowest feed rate of 4 p/s. By timing how long it takes to feed the sample in each test (say T sec), the so-called ‘maximum count rate’ is calculated to form the horizontal axis in Figures 2.5c and 2.5d according to MaxCnt/T . Figure 2.5a and 2.5c show the measurements of the IRS and EMS using the synthetic sample and bottom ash, respectively. For the synthetic sample at a particle feed rate of 7 per second the IRS counts 98.6% of all the particles and the EMS 97% of all the metal particles. Both samples produce the same downward trend towards high feed rates, albeit a bit stronger for bottom ash. The latter is most likely caused by the variability in particle shape and material properties that is typical for bottom ash. However, since these curves prove reproducible, the corresponding count correction factors shown in Figure 2.5b and 2.5d will be effective in compensating for the stationary counting error. On the other hand, the increase in stationary error is often also indicative of an increase in the stochastic spread, which here applies to the chance of simultaneously falling particles. This stochastic spread can only be suppressed by averaging the counts over larger numbers of particles.

On yet another note, in recycling practice the feed rate is commonly given in terms of mass rate rather than particle rate. This means that the particles rate for the IRS, but a bit more likely for the EMS, could change when the waste stream composition changes. Fortunately, the composition of large solid waste streams varies surprisingly little within a given batch and is expected to add only to the stochastic error, i.e. random variations, when applying the hybrid sensor at high feed rates.

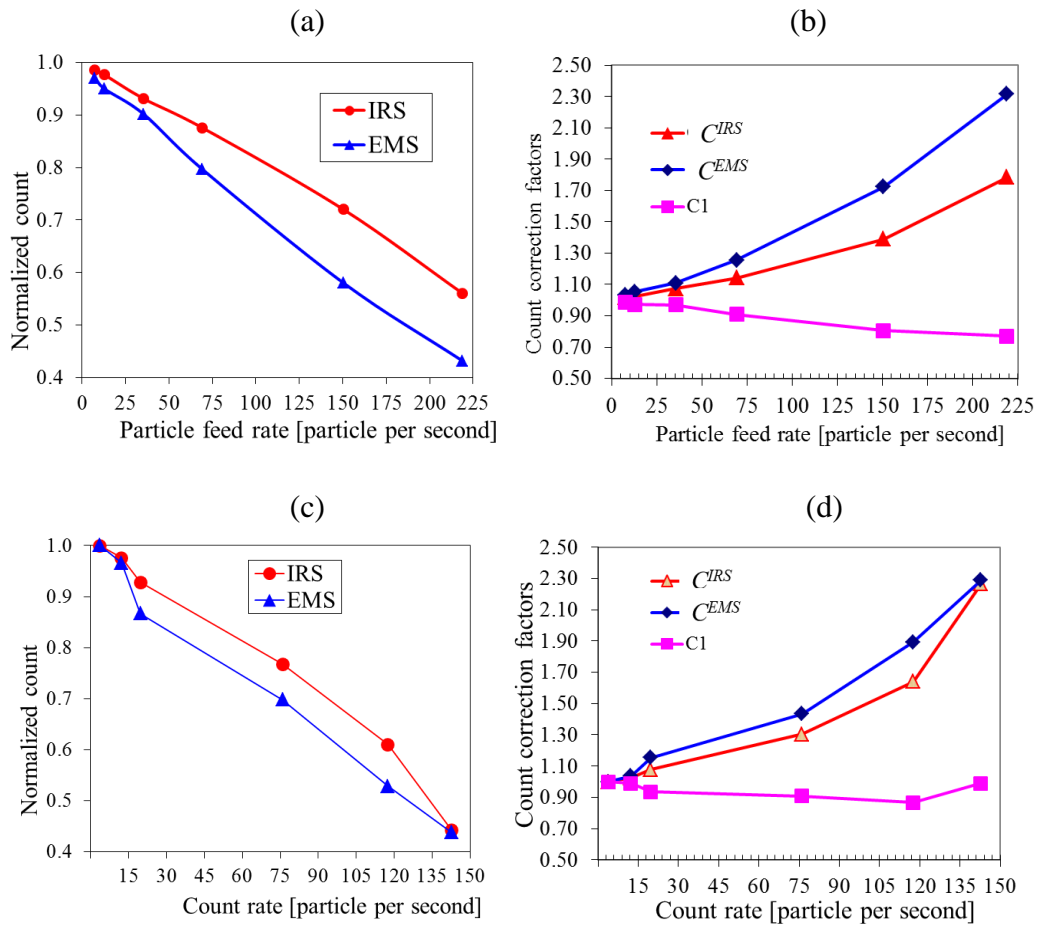


Figure 2.5: (a) Sensor counts against particle feed rate for the synthetic sample. (b) Count correction parameters for the synthetic sample counts in Figure 2.5a. (c) Sensor counts against maximum count rate for bottom ash (d) Count correction parameters for the bottom ash counts in Figure 2.5c.

It is also observed from Figures 2.5b and 2.5d that the count corrections change more rapidly between 12-35 particles per second for which mainly two mechanisms are responsible. First, the signal duration for a single particle puts a limit on how many particles per second can be counted by the electronic processing. For the IRS the signal duration is on average 1.7 ms and for the EMS it is on average 41.9 ms, noting that it depends on the particle velocity and for the IRS (only 3 mm diode height) also on the particle size. Theoretically these signal durations would allow for 588 and 23 particles per second, respectively, provided particles fall in perfect vertical alignment through the sensors. However, the second mechanism is the chance that particles actually fall simultaneously, i.e. within the given signal durations, which chance is related solely to the feed

mechanism. This chance proves to be detectable already at low feed rates and becomes a dominant factor after ~ 20 particles per second, because despite its large counting capability the IRS proves ineffective in maintaining an accurate count long before the 588 particles per second are reached.

2.6 Verification of metal grade detection method

To validate Eq. (2.3) the synthetic samples from Table 2.1 are first used at a constant low feed rate. In eight tests the calibrated grade is varied accurately from 80% to 10% by cumulative addition of specific amounts of sand while the metal content remained fixed. The sensor count ratio Z produced by these samples is shown in Figure 2.6a. The experimental values (markers) follow Eq. (2.3) (solid lines) within an average error of -0.007 , showing again that at low feed rates the hybrid sensor counts very accurately. Figure 2.6b shows the direct comparison between the measured and calibrated grade, which proves to be close to a perfect match for each k -value.

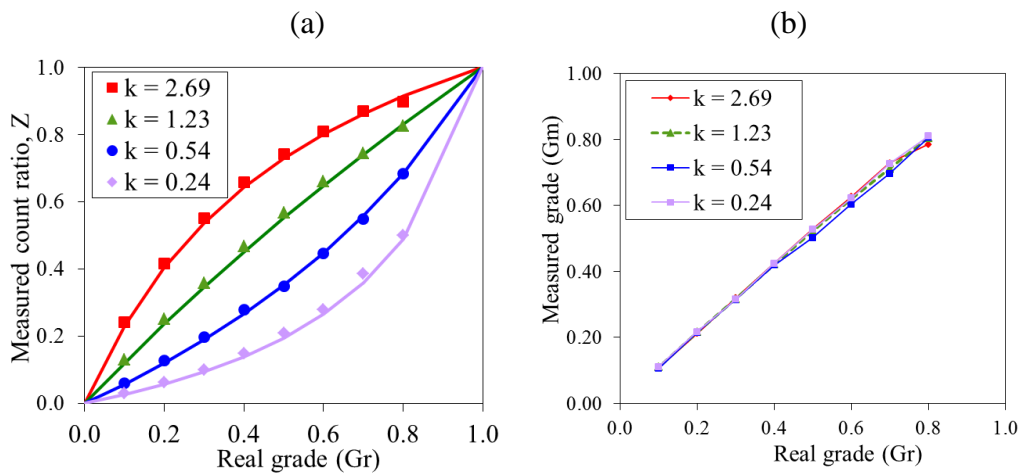


Figure 2.6: (a) Solid lines: prediction using Eq. (2.3) for $CI = 1$. Markers: Experiments using synthetic samples at a low feed rate with $CI = 0.99$. (b) Measured grade against the calibrated grade corresponding to (a).

2.7 Case study: MSWI bottom ash

2.7.1 Size distribution and signal strength

To estimate the influence of the particle size on the k -value it is important to assess the particle size distribution. Figure 2.7a shows the mass distribution of the bottom ash over the different sieve size ranges. For this purpose a fresh amount of 1 kg bottom ash sample was analysed whose measured moisture content was 7.1% which is quite in low level and it can be noted that the processability of the ash with low level moisture content is suitable for ECS bottom ash processing (Berkhout et al. 2011). For this sample the maximum content is found in the 5–6 mm size range and the minimum content in <1 mm.

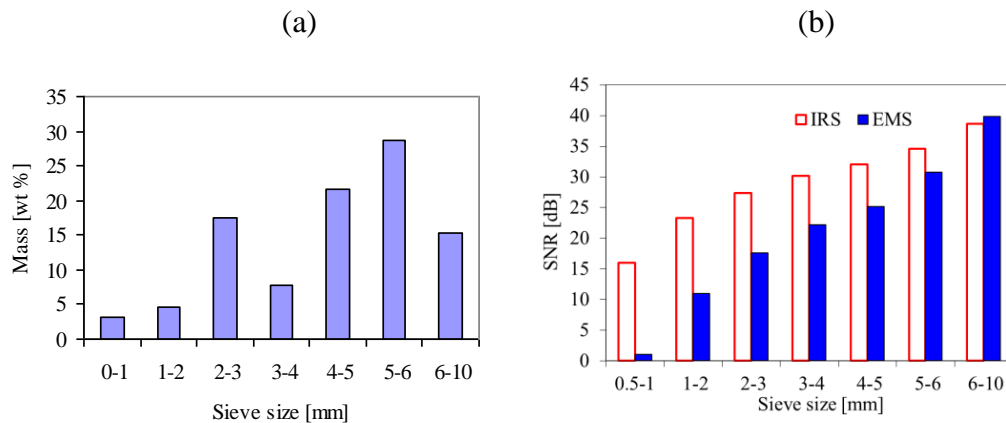


Figure 2.7: (a) Mass distribution over the sieve size ranges of the bottom ash sample. (b) Signal to noise ratio (SNR) in the sieve size ranges for bottom ash.

The fine particles, i.e. smaller than 1 mm and either already present or produced during testing, are suppressed in the sensor counts by using the >1 mm detection levels given in Table 2.2. The signal amplitude produced by the sensors depends on the size, shape and orientation of the falling particle, while the IRS amplitude depends also on optical properties and the EMS on electric and magnetic properties. This complicated set of dependencies comes together in bottom ash for which the sensor amplitude distributions have to be determined experimentally. For that purpose the two fine sieved fractions 0-1 mm and 0-2 mm from Figure 2.7a are fed to the hybrid sensor in a set of repeated tests in which the detected signal amplitudes are recorded. Figure 2.7b shows the signal-to-noise ratio (SNR) in the average of the detected signals. Note that the limit sensitivity for the IRS was 0.5-1 mm and for the EMS 1-2 mm. The near linear increase in SNR as a

function of particle size may present a possibility to obtain a rough estimate of the k -value from the time-averaged amplitude measurements if the average mass densities of non-metal and metal particles are known. In the Netherlands the average metal mass density of ECS non-ferrous metal concentrated bottom ash is dominated by Al alloys (~65%) and Cu, Zn, Pb (~35%). The average non-metal mass density is dominated by minerals such as sand, glass, brick and porcelain.

2.7.2 k -value and metal grade

A sample of 600 g bottom ash in the single size fraction 1-6 mm and 7.1% moisture was split up into six subsamples S1-S6 each of 100 g. Each subsample was used in a repeated test using the hybrid sensor at a low feed rate. After the sensor test, the metal content in each subsample was analysed manually after flattening the particles to remove some of the brittle contaminants and help reveal the ductile metal particles. It is noted that due to the complex composition of incineration bottom ash the manual analysis will also be at least a few percent off from the real pure metal grade. Flattening may cause some fine metal fragments that may escape visual analysis. Moreover, moisture and minerals and corrosion products (e.g. oxides) sticking to metal particles will unavoidably to some degree contaminate the manual analyses. It is noted the latter also affects the sensor measurements to the same degree as it tends to lower the k -value. It can be noted that the oxides can reduce the grade in a sample e.g. for the case of aluminium to aluminium-hydroxide as reported (de Vries et al. 2009).

Table 2.4 shows the manually determined metal grade and the average count data from the two sensors. The average metal and non-metal particle masses calculated as 97 +/- 18 mg and 48 +/- 11 mg, respectively. Note that both these absolute errors comply with ~20%, which shows that the metal and non-metal particle types were both sampled satisfactorily using the 100 g (once repeated) samples. The average value of k was 0.49 +/- 0.07 and this value was used in Eq. (2.1) to calculate the grades G_s with the hybrid sensor in Table 2.4. The correspondence between the measured and manually determined grade is quite satisfactory with an average deviation of 2.4%. The manual grade in sample S2 is significantly higher, probably due to the occurrence of a few big metal particles judging from the high metal particle mass and grade G_m . On the other hand, for

sample S6 the measured grade G_s is significantly higher, probably due to some exceptionally big non-metal particles judging from the corresponding high k -value. These outliers are typical for bottom ash and can only be suppressed by averaging over larger samples.

Table 2.4: Metal grade analyses of bottom ash samples, each of 100 g, sieve size 1-6 mm, particle feed rate 13 per second, $CI = 1$ is assumed, $k=0.49$ in G_s calculation.

Sample	manual grade (G_m)	IRS count	EMS count	metal particle mass	non-metal particle mass	k	measured grade (G_s)	Error $G_m - G_s$
	[wt %]			[mg]	[mg]		[wt%]	[wt%]
S1	23.9	2236	281	85.1	38.9	0.46	22.6	1.3
S2	32.2	1423	247	130	57.7	0.44	29.9	2.3
S3	21.3	2278	262	81.3	39.0	0.48	20.9	0.4
S4	23.5	2145	259	90.7	40.6	0.45	21.8	1.7
S5	22.5	1959	249	90.4	45.3	0.50	22.8	-0.3
S6	21.9	1418	211	104	64.7	0.62	26.2	-4.3
Average:				96.9	47.7	0.49	24.0	0.17
Standard deviation:				18.1	10.9	0.07	3.4	2.4

The previous test was performed at a low feed rate, but it is also of interest to evaluate the grade prediction at high feed rates to check if then the count correction ratio is also effective in compensating for the stationary error. For that purpose we reuse the calculated values of the count correction ratio CI for bottom ash shown in Figure 2.5d to calibrate the hybrid sensor. Note that all results in Figures 2.5c and 2.5d were obtained using the same bottom ash sample of 100 g that came from the same batch as those used for Table 2.4, which means $k=0.49$ was a good first estimate for the present sample. After the tests used for Figures 2.5c and 2.5d the metals in that 100 g bottom ash were manually analysed and gave a metal grade of $G_m = 23.2\%$. Table 2.5 shows the measured grade using the sensor counts and the correction ratio from Figure 2.5d at the various average particle rates. The measured grade is consistently 2.2% lower, which deviation vanishes when taking $k=0.43$ for this sample. Note that this k -value falls within the 1-std range 0.49 ± 0.07 found in Table 2.4. These tests show that indeed the count correction ratio is also effective as error compensation at high feed rates.

Table 2.5: Calculation of measured grade (G_s) using the data from Figures 2.5c and 2.5d. The manually analysed grade (G_m) was $G_m = 23.2\%$ and $k=0.49$ in G_s calculation (from Table 2.4).

IRS particles count rate	IRS count	EMS count	Count ratio (Z)	CI	measured grade (G_s)	Error G_m-G_s
[per sec]					[wt %]	[wt%]
4	2283	263	0.12	1.00	21.0	2.21
12	2228	254	0.11	0.99	21.0	2.21
20	2118	228	0.11	0.93	21.1	2.12
76	1752	183	0.10	0.91	20.9	2.27
118	1392	139	0.10	0.87	20.9	2.28
143	1009	115	0.11	0.99	21.0	2.22

2.7.3 Operational statistics

The count correction ratio shows that if both sensors miss the same relative amount of particles the hybrid sensor may still be quite accurate. The chance of missing one or more particles by simultaneous falling may perhaps be assumed to be the same for metal and non-metal particles if they are in the same sieve size. However, the precise statistics related to the chance of simultaneous falling depends on the feed mechanism, which has to be characterized as is done in this work in order to achieve a highly accurate grade measurement. The count correction ratio as demonstrated in Figure 2.5 and Tables 2.4 and 2.5 is in effect a compensation for the stationary error of the hybrid sensor due to simultaneous falling. What is left is a stochastic error resulting from the following influences:

- Fluctuations in the chance of simultaneous falling particles (affecting CI)
- Variations in feed material (affecting k)
- The sampling error

All three may be suppressed by employing an interval measurement strategy in which M samples are averaged with each N^{EMS} counted metal particles. If the hybrid sensor shows a stochastic error σ^{hybrid} (for example 2.4% in Table 2.4), the measurement error and sampling error resulting from such an interval measurement may be determined from

$$sampling\ error = 1/\sqrt{MN^{EMS}}, \quad measurement\ error = \sigma^{hybrid}/\sqrt{M} \quad (2.4)$$

Note that the sampling error is related solely to the number of counted metal particles and gives the expected variation in that number between different intervals. In other words, it shows how representative the relative number is for the real relative number of metal particles in the waste stream. The stochastic measurement error is effectively reduced by averaging multiple analysed samples, producing one highly accurate average sample measurement every $M\Delta t$ seconds, where Δt is the time it takes to analyse just one sample. For example, suppose the particle feed rate is chosen as 48 per second and CI has been properly calibrated ($CI = 0.92$, cf. Figure 2.5d). Further assume that $G = 20\%$ and $\sigma^{hybrid} = 6\%$. If the acceptable sampling error and grade measurement error are both given as 3%, then for $M = 4$ and $N = 1389$ ($N^{metal} = 278$ if $k = 1$) these accepted errors will be achieved. At the feed rate 48 per second one interval measurement will take about 2 minutes, which is already quite acceptable in ECS bottom ash processing. When the grade is higher the sample size N may be taken smaller and the measurement time will go down further.

2.8 Conclusions

Proposed is a hybrid sensor system for in-line detection of the metal grade of a stream of falling waste particles, and in particular bottom ash. The principle and capabilities of the IR and EM sensors making up the hybrid system were studied using both synthetic and bottom ash samples in the size fractions 1-6 mm. The hybrid sensor showed excellent performance with a 2.4% metal grade accuracy for a particle feed rate up to 13 per second. It is demonstrated that at higher feed rates the system starts missing significant amounts of particles due to simultaneous falling particles, but that number of misses proves quite repeatable. This gave the possibility to introduce sensor count correction factors to eliminate

the stationary error by calibration, even for a feed rate 143 per second. The remaining stochastic variations in the sensor grade measurement, i.e. feed and material composition variations and the sampling error, may be reduced to acceptable levels by employing averaging in an interval measurement strategy. In a practical setup the feed rate may simply be controlled by using a larger or smaller sample chamber opening inside the particles stream. As a potential application, the hybrid sensor could be implemented for either in-line quality control or for separation control, for example for an eddy current separator. The ability to measure the grade of the 1-6 mm bottom ash stream outside of a laboratory will constitute a major step forward in today's bottom ash metals recycling capabilities.

References:

- Bekhout S. P. M.**, Oudenhoven B. P. M., Rem P. C. 2011, Optimizing Non-ferrous Metal Value from MSWI bottom ashes, *Journal of Environmental Protection*, Vol. 2, 564-570.
- de Vries, W.**, Rem, P. and Berkhout, P., 2009, October. ADR: a new method for dry classification. In *Proceedings of the ISWA international conference*, Vol.12, pp. 103-113.
- Grosso M.**, Biganzoli L., Rigamonti L., 2011. A quantitative estimate of potential aluminium recovery from incineration bottom ashes, *Resour. Conserv. Recycl.*55, 1178– 1184.
- Muchova L.**, Bakker E., Rem P. 2009, Precious Metals in Municipal Solid Waste incineration bottom ash, *Water Air Soil Pollute: Focus* 9, 107–116.
- Rahman Md.**, Bakker M.C.M, 2012, Hybrid sensor for metal grade measurement of a falling stream of solid waste particles, *Waste Management* 32, pp. 1316-1323.
- Rem P.C.**, De Vries C., Van kooy L. A. Bevilacqua P. and Reuter M. A. 2004, The Amsterdam pilot on bottom ash, *Minerals Engineering* 17, 363–365.
- Rem, P. C.**, Zhang, S., Forssberg ,E., De Jong, T. P.R., 2000. The investigation of separability of particles smaller than 5mm by eddy-current separation technology part II: Novel design concepts. *Magnetic and Electrical Separation*, Vol. 10, pp. 85-105.
- Zhang S.**, Forssberg E., Bo Arvidson, Moss W.,1998, Aluminium recovery from electronic scrap by high-force eddy current separator, *Resources, Conservation and Recycling* 23 (1998) 225–241.

Chapter 3

Functionality Analyses of the Hybrid Sensor

This chapter presents a study into the possibilities for application of the hybrid sensor as developed in Chapter 2. The focus is on inspection of bottom ash materials from which the contents of this chapter was also published from this research (Rahman and Bakker, 2013) and presented here with minor change. An improved, robust prototype of the hybrid sensor was built and attached to the splitter of an eddy current separator machine, which placed the sensor in-line with a concentrated metals stream of 1-6 mm metal and mineral particles. The splitter distance from the ECS rotor was varied and the ability of the sensor to detect the metal grade as a function of distance is studied in the laboratory with a batch of moist bottom ash and in-situ with dry and wet bottom ashes. The grade measured by the sensor was compared to manual analysis of the materials, which were collected after falling through the sensor, and this proved to be both accurate and repeatable. However, the sensor data predicts quite accurately the trend of the metal grade of the particles stream with splitter distance, which is mandatory for sensor-based control of the ECS splitter position in bottom ash processing.

3.1 Introduction

Eddy current separation (ECS) is widely applied for concentration of non-ferrous metals from mixed waste streams. Referring to the Figure 1.3a from Chapter 1 i.e the optimum feeding method for the ECS maintains a uniform monolayer of material on the conveyor belt, which is critical for ECS-performance and typical ECS machine settings for fine grained materials (<10 mm) are 8-12 tons per hour feed capacity, 1.5-2 m/s belt speed and 2000-3000 rpm for the drum containing the permanent magnets (Maraspin et al., 2004). However, the main problem in an industrial operation is that the trajectory fans of metal and mineral particles change depending on the composition of the feed material and the moisture content. Therefore, feed variations should be responded to in real-time by effective adjustment of the splitter distance. This capability appears unsatisfactory in contemporary operator-controlled ECS processing, specifically for the <6 mm bottom ash as it was mentioned in the background part of this thesis (see Chapter 1).

As a part of EU strategy, the processing of bottom ash and the related grate furnace technology should comply with the best available technologies (Van Brecht and Konings 2011). However, acceptance of existing, advanced technologies and development of new technologies may be stimulated if it can be proven that the products, i.e. the secondary metals, comply with high quality demands. Quality opens up the market by creating wider acceptance of the secondary raw materials and stimulates innovation through sound economic incentives rather than by governmental subsidies. The quality aspect is therefore triggering research into new sensor technologies and applications (Pretz and Julius, 2011), of which the present work is an example. The drive towards more quality in secondary resources is in line with the European ambitions to define suitable end-of-waste criteria, defined in the EU waste frame directive, for bottom ash. This means that secondary resources of sufficient quality may be treated and transported on the same terms as primary resources.

A bottleneck in arriving at suitable criteria for bottom ash minerals is a proper assessment of the risks of leaching, especially in relation to the heavy metals content. Increasing the recovery of metals from bottom ash using sensor-based

optimization in eddy current separation will proportionally reduce the metal content of the mineral by-product. This may improve their suitability as a building material, for example as aggregate in new concrete (Ginés et al., 2009).

Proposed is to employ developed hybrid sensor system presented in Chapter 2 in the falling stream of the ECS metals concentrate to sample the metal grade and to detect ECS-dependencies of the metals product as the principle is depicted in Figure 1.3b. The sensor grade and particle counts give real-time information that may be useful for quality assessment and/or for control over the splitter distance. The sensor data may also be combined with manual recovery analyses, which are already performed regularly in an industrial operation for market purposes, to build up a database for different sources of feed material and to set out strategies for optimum value recovery. The sensor unit and its potential functionalities in an ECS setting are investigated both in the laboratory and in-situ at a bottom ash processing plant. The laboratory offers controlled conditions and allows accurate determination of the optimum sensor performance, while the in-situ tests may reveal the possible influence of extreme operational conditions. To widen the research scope, two different ECS machines and two different bottom ash sources were used, while the moisture content of the feed could be characterised either as dry, moist or very wet.

3.2 Materials and method

3.2.1 Sensor and ECS¹

The online hybrid sensor is composed of an electromagnetic and an infrared section. The first counts only the metal particles, while the infrared section counts all the particles that fall through the sensor sampling tube. The metal grade G of the stream may be calculated from an adequate sample size by integrating the sensor counts over a time interval using the Eqs (2.1) and (2.2) as presented in Chapter 2. Parameter k is obtained by calibration and depends on the average composition of the particle stream in which the sampling tube is placed. Its value therefore depends both on the feed and on the specific ECS behaviour

¹All experimental supports including ECS in laboratory and in-situ are provided by the Resources and Recycling Laboratory, faculty of Civil Engineering and Geosciences, Delft University of Technology, Netherlands.

and is a key parameter in this work. The parameter $C1$ corrects for the chance of particles falling simultaneously so the sensor misses counts, which chance is a function of particle feed rate through the sampling tube. The value of $C1$ may be picked up from a known calibration curve. All these details of the hybrid sensor are presented in Chapter 2 and may also be available in an earlier published work (Rahman & Bakker 2012, reference Chapter 2).

Some modifications to the first build laboratory prototype were necessary to accommodate the harsher physical conditions found in the bottom ash plant. For example, the sensor unit had to be encased to render it watertight and robust against wear from falling particles and electromagnetic interference. A data acquisition system, capable of transmitting the data through the internet, was incorporated to allow for continuous access to the sensor data. Figure 3.1a shows the improved prototype unit² installed in the laboratory ECS (type BM 29.713/118) and in Figure 3.1b the unit is installed in the in-situ ECS (type Steinert 6119). In all ECS tests the sensor sampling tube entrance is fixed to the middle-top of the splitter on the side of the metals product. In the laboratory the tube entrance was 100 mm wide and 50 mm long (in the direction away from the splitter). In-situ the tube entrance was round and 40 mm in diameter, which is effectively much smaller because the particle feed rate near the sampling tube proved up to twelve times higher than in the laboratory.

The sensitivity of the sensor unit has been adjusted to only detect particles larger than 1 mm, since finer material does not play a significant role in metals recovery from moist bottom ash and an ECS. To this end, the sensor sections are calibrated using a small batch of sieved <1 mm bottom ash and setting effective amplitude detection thresholds. In the laboratory tests a shaking feeder was employed to evenly distribute the bottom ash in a 250 mm wide monolayer on the conveyor belt at an effective mass feed rate of 700 kg/h per meter width of the feed belt. The belt and rotor speed of the laboratory ECS were set at 1.7 m/s and 3000 rpm, respectively.

² The improved prototype unit of the developed hybrid sensor is built by the electronic and mechanical support division (DEMO) of the Delft University of Technology, Netherlands.

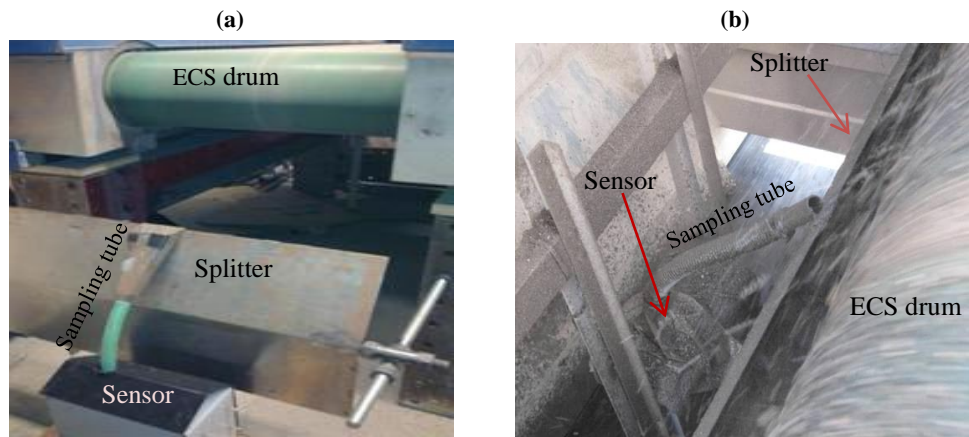


Figure 3.1: ECS settings with the sensor unit mounted on the splitter at the metal concentrate side. (a) In the laboratory. (b) In-situ at a bottom ash treatment plant.

3.2.2 Samples materials³

The feed material is the sieved 1-6 mm fraction of municipal solid waste incinerator bottom ash. It is noted that it is customary to first remove the ferrous metals to prevent damage to the ECS feed belt. The batch referred to as ‘batch L’ contained dry-sieved bottom ash with 10.7% moisture content and was used only in the laboratory. The batch referred to as ‘batch I’ contained wet-sieved bottom ash and was used in-situ. One part of batch I was dried in storage to 4.6% moisture content, while the complement was still quite wet with 13% moisture content. The metal content of the feed was 6.6% for batch L, 7% for the dry part of batch I and 7.4% for the wet part of batch I. Figure 3.2 shows the laboratory feed batch L (3.2a), the ECS metals concentrate sampled by the sensor (3.2b) and the metal content of the sensor sample after rolling to facilitate manual analysis of the metal content (3.2c). In each test, samples are taken from what went through the sensor and from what ended up in the product. In the laboratory the sensor sample and the data were collected in 100 second intervals, while in-situ five minute integration intervals were applied. In the laboratory the whole product and sensor bin contents from each 5 kg feed batch could be analysed. Thus, it proved that on average the mass in the sensor bin made up 32% of the total metals concentrate of sample bin plus product bin. During the in-situ tests, samples of the

³All supports for the sample materials presented in this chapter are provided and arranged by the Resources and Recycling laboratory, faculty of Civil Engineering and Geosciences, Delft University of Technology, Netherlands.

practically continuous ECS process had to be taken. During the measurement interval, all material falling through the sensor was collected and formed the sensor sample. In contrary, the product sample was collected by manually moving once per minute a collection bin to and fro through the wide product stream falling from the product conveyor belt. With this approach, both the sensor and product in-situ sample masses ranged from 0.5-1 kg for the dry feed to 0.14-0.8 kg for the wet feed. The metal content of the bins were evaluated manually by subsequently roller crushing of the sample to crush the minerals, handpicking the metals and weighing. In principle, the metal content is therefore determined on a wet basis since no drying was involved, but practice shows the moisture played a negligible role in the recovered metal mass.

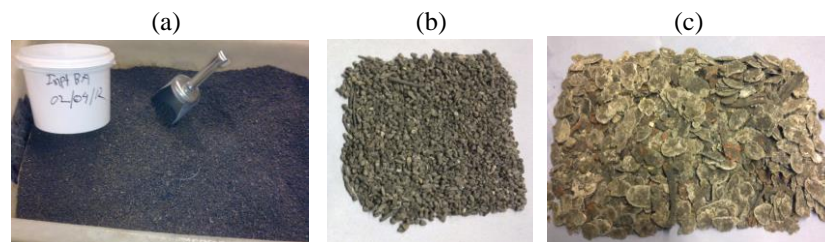


Figure 3.2: Bottom ash from batch L with size fraction <6 mm used in the laboratory tests. (a) Feed material. (b) Non-ferrous metal concentrate sampled by the sensor. (c) Metal content of the sensor sample after roll crusher to remove minerals.

3.3 Laboratory test results

Laboratory tests were conducted to accurately measure parameter k in Eq. (3.1) and to verify the accuracy of the sensor grade in a comparison with manual analysis. The value of k may be influenced by common variations in feed composition and by segregation due to the ECS. Foremost, the ECS separates non-ferrous metals from minerals in essentially two trajectory fans due to segregation from differences in electrical conductivity. The ECS magnetic lifting force depends also on the particle size and shape, which influences the trajectory of the metal particle. This results in segregation in which larger-sized metal particles tend to end up further from the ECS drum. This ECS behaviour may have a significant influence on the k -value as sampled by the sensor as a function of distance. Other, less strong segregation mechanisms for the +1 mm metal

particles are the ballistic effects when they become airborne from the feed belt and their trajectories get influenced by factors such as mass density and drag. These may also influence on the sampled k -value. The ballistic effects are quite probably the dominant cause of segregation for mineral particles, resulting in a fan of trajectories of their own.

Each of the nine ECS-sensor tests was conducted with 5 kg bottom ash. Before each test, the splitter was shifted 5mm relative to the estimated optimum splitter distance of 350 mm from the edge of the ECS drum, cf. Figure 3.1a. In addition to the sensor measurements, manual analyses were carried out on the contents of the sensor bin and the metals product bin. In the nine tests a combined total of 639 g material was measured by the sensor, which returned a count of 3800 metal particles out of a total of 8660 particles. Combined with the manual analyses of the metal content, the particle masses were found to have the averages of 105 mg for metals and 50 mg for mineral particles. The resulting average and standard deviation for k was 0.48 ± 0.04 . Figure 3.3a shows k of the sensor sample as a function of splitter distance. Judging from the small variations, the ECS segregation was not a strong factor in these measurements with the exception at 330 mm. There, the mineral stream (trajectory fan) becomes intense and k increases significantly. Note that k increases if on average the metal particles become smaller or if the mineral particles become larger, and both effects seem equally possible closer to the ECS. However, a plot of the average particle masses in Figure 3.4 reveals that it is the average mineral particles mass that increases the most at 330 mm. Another observation in Figure 3.4 is that the metal particles mass shows a tendency to increase at 370 mm, which is consistent with larger metal particles having a longer ECS particles trajectory.

The sensor grade is calculated using Eq. (2.1) and (2.2) for $k=0.48$ and shown in Figure 3.3b together with the manually determined grades of the sensor bin and product bin. The sensor grade follows the manual analyses within a few percent. The exception is again the position closest to the ECS where the real k -value is significantly larger than 0.48. The sensor bin grade is quite close to that of the product bin, indicating that the sensor sample was representative for the whole metals concentrate. The grade is practically a monotonic and increasing function

of splitter distance, since only metal particles tend to have longer particle trajectories. Despite the relatively small range of 40 mm in which the measurements were conducted, the grade is observed to vary significantly, showing that splitter distance is a sensitive parameter in this ECS application.

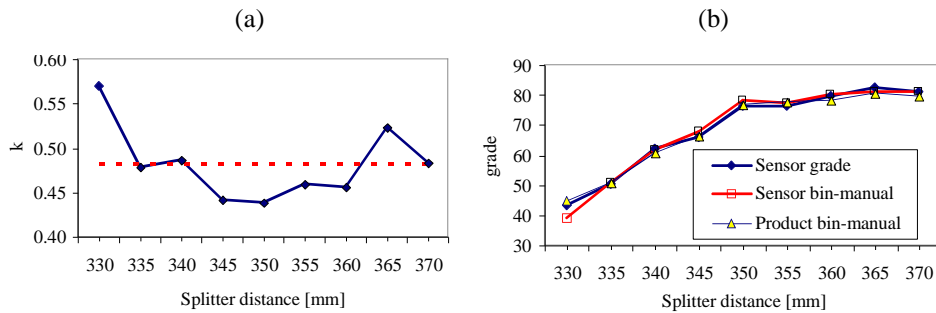


Figure 3.3: (a) Laboratory ECS tests for the average particle mass ratio k and its mean value (dotted line) for 1-6 mm moist bottom ash from batch L. (b) Comparison of the measured grade (sensor grade) and the manually analysed grades of the sensor bin and the product bin.

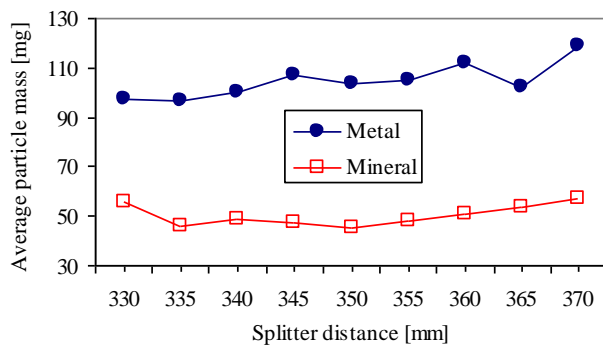


Figure 3.4: Laboratory measurements of the average particle mass of metals and minerals.

Figure 3.5 reveals that metal counts goes higher when splitter gets closer that means still the machine eddy current separator (ECS) is not that much efficient to escape out all that metal particles from the stream or it can be assumed that the metal particles those are closer to the ECS drum are very smaller <1mm but their population in terms of number may be higher. It was obvious most of the larger particles are escaped out quite farther from the ECS drum (cf.1.3, Page 6). On the other hand the non-metal counts abruptly drop if splitter moves away from the ECS drum. So the trends of sensor data vs. splitter distance are quite comparable and rational from theoretical point of view of an ECS machine (Rem et al. 2000, Maraspin et al. 2004, Schломann 1975).

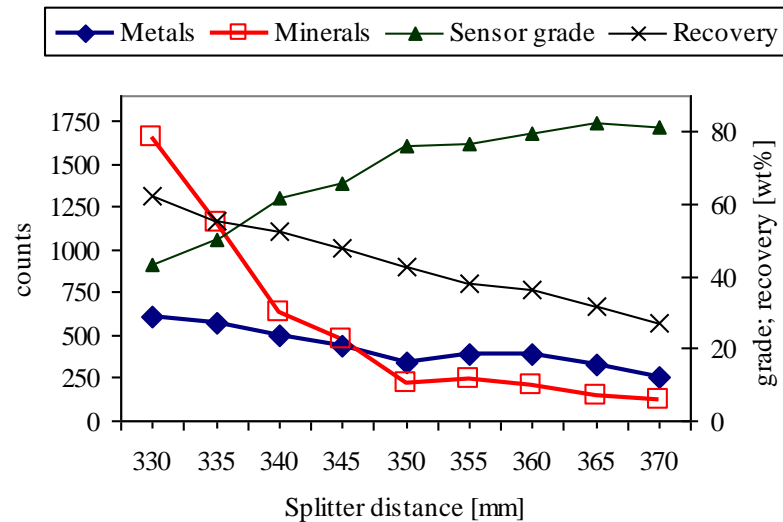


Figure 3.5: Laboratory test comparisons of metal and mineral sensor counts, sensor grade, and recovery of the complete metals concentrate. The feed grade was 6.6%.

However, Figure 3.5 shows trends and correlations between the metal and mineral particle counts, the sensor grade and overall metals recovery (metal mass in complete concentrate divided by metal mass in the 5 kg feed). The minerals count jumps up in Figure 3.5 when the splitter moves closer than 345 mm to the ECS, which is consistent with the increase in k in that range. The jump indicates the onset of the ECS trajectory fan described by the mineral particles. It is remarked that the mineral stream makes up ~97% of all the particles in the feed. The mineral particle count drops with distance up to 350 mm and then continues to follow the metal count curve instead of reducing further. A plausible explanation is that, on average, one out of three metal particles either carries or scoops up a mineral particle during launch from the ECS feed belt and delivers it to the product. Note that metal particles are on average two times heavier. An additional contributing mechanism is that some mineral particles bounce off the splitter's edge and into the product bin. These mechanisms explain the unexpected presence of relatively many mineral particles beyond the main minerals trajectory fan and the coupling of mineral and metal count numbers, while it does not conflict with the rather stable k -value above 350 mm in Figure 3.3a.

It was surmised that near the ECS drum only the smallest metal particles would be found due to segregation mechanisms, but it was unknown from which splitter distance onward this could be detected by the sensor. The metal counts in

Figure 3.5 increase towards the ECS drum, starting at 345 mm, though much less than the mineral counts. This indicates that on average there are more metal particles falling closer to the ECS drum, but they do not appear to be much smaller (i.e. less heavy) than further down the splitter range (cf. Figure 3.4). Moreover, the average value of 105 mg in Figure 3.4 complies with metal particles that are generally heavier than what is representative for the size range 1-3 mm. Therefore, it can be concluded that either the smallest metal particles give a minor contribution to the metal content of the feed, or the splitter did not move close enough to the ECS drum and most of the smaller metal particles are irretrievably mixed with the much larger mineral stream.

A last observation from Figure 3.5 is that the recovery is a monotonic function, just like the grade but with the opposite trend. In fact, between 330 and 350 mm the grade and recovery curves are practically linear with equal, but opposite derivatives and they cross at ~55%. The recovery and grade prove sensitive to the splitter distance, since a 10 mm shift may already result in 10% difference in recovery and/or 18% difference in grade.

3.4 In-situ test results

The in-situ tests were performed using both quite dry feed (4.6%) and quite wet feed (13%) to investigate the influence of these extremes on product quality. The ECS was running at full capacity 8-12 ton/h using a 1.5 m wide feed conveyor belt. The experienced ECS operator estimated the optimum splitter distance at 192 mm from the edge of the ECS drum for the dry feed and at 170 mm for the wet feed. Two series of tests were carried out for dry and wet feed bottom ash, respectively, in which the splitter distance was changed in either 5 or 10 mm steps relative to the estimated optimum, depending on the judgement of the experimenter. At each splitter distance, sensor data and samples were collected during a five minute interval from the sensor bin and from the metals concentrate falling from the product conveyor belt.

3.4.1 Dry feed bottom ash

Figure 3.6 shows the k for both the dry and wet feed. The measured k for dry feed of 0.60 ± 0.20 is 25% higher than for the laboratory tests. In order of probability this difference may be explained by the combination of ECS type, source of bottom ash and sieving method used to obtain the 1-6 mm fraction. Figure 3.7 shows the variations in the metal and mineral particle counts in combination with the sensor grade and the product bin grade for the dry material. The trends in the sensor counts are quite similar to the laboratory tests, except that here the splitter did not reach the distance where the mineral counts dive below the metal counts. The sensor grade is again a monotonic function but increases only from 27% to 49%, which is substantially lower than observed in the laboratory (43-82%).

However, there is significant offset between the sensor grade and the product. The offset variation at 182 mm may be attributed to the jump in k , but the offset remains consistently 21% for the other four splitter positions. This offset is due to the fact that the sensor sample was not representative for the grade in the complete product. In contrary to the situation in the laboratory, where the sensor sample contained on average 32% of the complete product, in the in-situ scenario the sensor sampled far less. The feed conveyor was 1.2 m wide and the product collection surface was 35 cm long while the sensor sampling tube entrance was only 4 cm in diameter.

However, the main reason for the difference in grade was not the sensor sample size, which was adequate, but the fact that many metal particles had trajectories that carried them further from the splitter compared to the laboratory setting. In other words, the in-situ ECS gave larger metal particles a longer trajectory in comparison to the laboratory ECS, resulting in a wider trajectory fan for the metal particles. This effective improvement in separation performance may quite likely be attributed to the eccentric magnet-drum positioning in the in-situ ECS. Placing the sampling tube deeper into the product area, i.e. away from the splitter, will render the sensor sample better representative for the total product. The sensor grade is evaluated at one minute integration intervals during five minutes in Figure 3.8, demonstrating that the sampling and sensor readings themselves are quite reproducible and accurate.

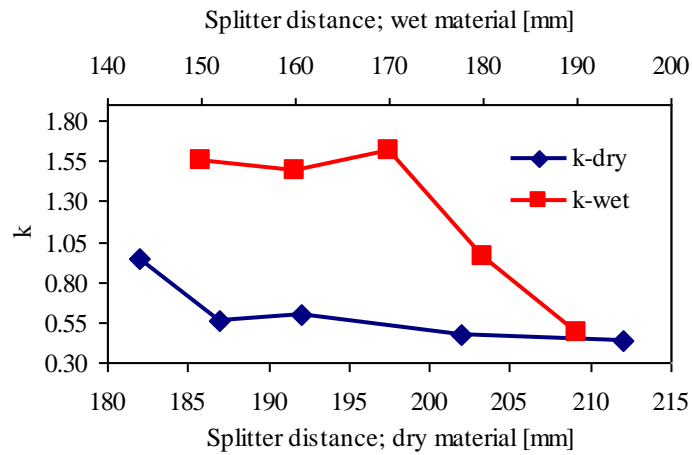


Figure 3.6: In-situ average particle mass ratio for dry and wet 1-6 mm bottom ash, measured at five different splitter distances. Notice that the wet particles landed on average 22 mm closer to the ECS drum.

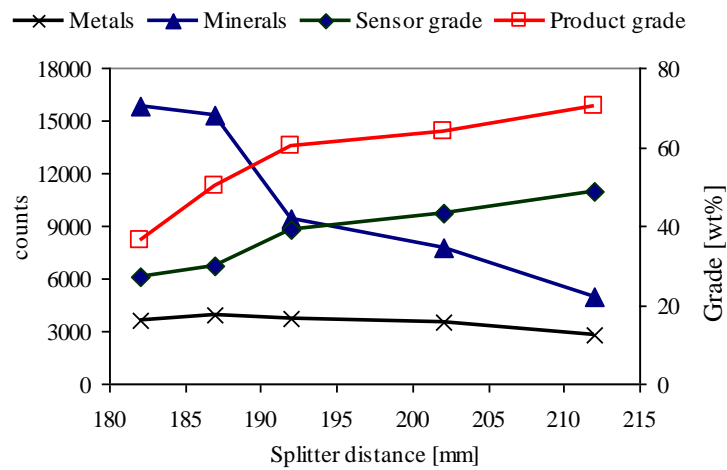


Figure 3.7: In-situ counts of mineral and metal particles, sensor grade and product bin grade for 1-6 mm dry bottom ash using $k = 0.60$.

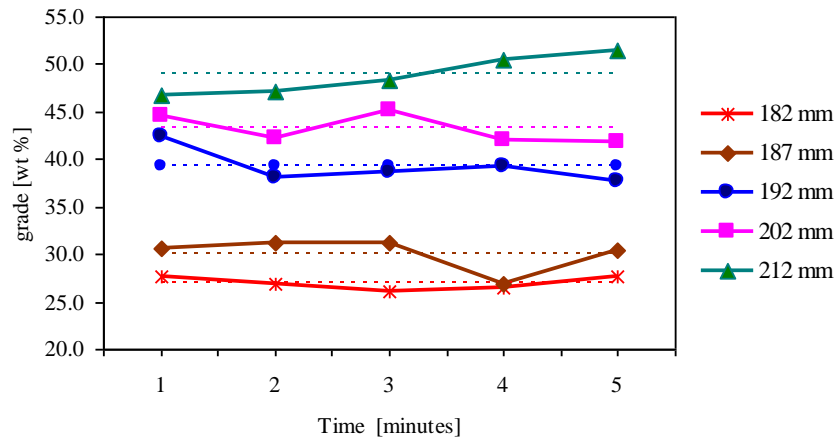


Figure 3.8: In-situ grade measurements integrated over one minute interval for $k=0.6$ at the five splitter locations for dry bottom ash. The average of five minutes is shown as a dotted line.

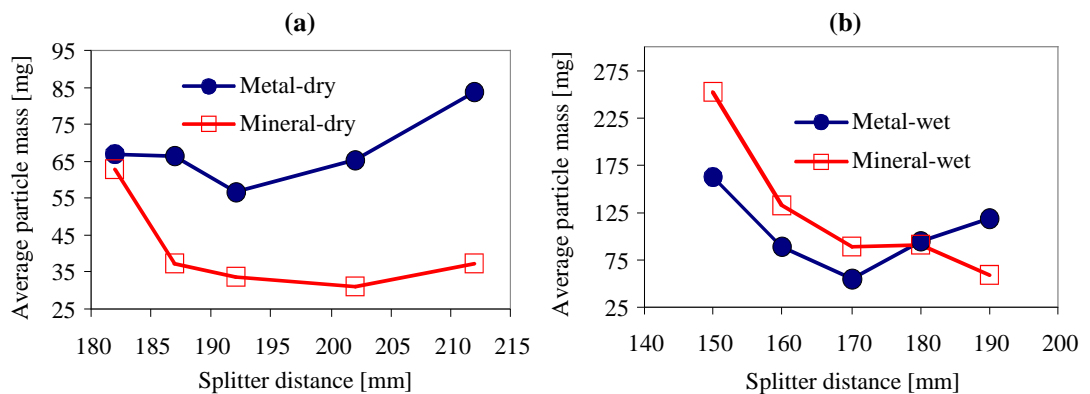


Figure 3.9: In-situ measurements of the average particle mass of metals and minerals. (a) Dry bottom ash. (b) Wet bottom ash.

Figure 3.9a shows the average particle mass for dry material, which ratio produced the k -curve in Figure 3.6. The cumulative averages are 68 mg for metals particles and 41 mg for the minerals. It is noted that especially the metals particles mass is considerably lower than for the moist laboratory material in Figure 3.4. Judging from the low grade in the sensor sample, cf. Figure 3.7, a plausible explanation is that the heavier metal particles are not properly sampled by the sensor as they had wider trajectories which landed them all mainly in the product. Consequently, the product would show on average a higher average metal particle mass than the sensor sample. An indication to this effect is the rising trend in metal particles mass with distance in Figure 3.9a. Note that the rise in the

minerals particle mass closest to the drum is again an indication that the splitter is moving into the mineral particles trajectory fan.

3.4.2 Wet feed bottom ash

The k -value for the wet part of batch I is shown in Figure 3.6. The differences with the dry part of batch I and the moist laboratory material in Figure 3.3a are striking. The k increased three-fold and only came down to values comparable to dry material farther from the ECS drum. The high values predominantly point to heavy mineral particles that are formed by surplus free water bonding larger mineral particles together, as deduced from the particle masses in Figure 3.9b. The cumulative averages are 104 mg for metals particles and 125 mg for the minerals. This means the particles in the sensor sample were on average 1.5 times (metal) and 3 times (mineral) heavier than for dry feed. The metal particles were probably somewhat heavier when airborne in their ECS trajectories, since the abundant mineral particles will also have adhered to metal particles on the feed belt. Any adhered mineral mass could not have contaminated the manually measured metals mass, since roller-crushing was applied before handpicking the metals.

However, this means that any metal-adhered minerals mass will have been added to the minerals, which lead to a slight increase of the average mineral particle mass in Figure 3.9b. The adhering of mineral particles due to excess water was already apparent on the ECS feed belt, where it was observed during the tests as a continuous feed disturbance in the form of empty patches in the monolayer. This self-organising ability of wet material negatively influenced the performance of the ECS. The most probable consequence was that the metals recovery dropped as many of the lighter metal particles bonded with minerals and ended up in the minerals bin. In fact, feed material was sticking to the wet conveyor belt and got scraped off underneath the belt into the minerals product. The particle counts in Figure 3.10 confirm this scenario, because the averages are only fractions of the numbers for the dry feed in Figure 3.7. From Figure 3.9b it is clear that only the largest of particles made it into the metals concentrate. The necessity to move the splitter on average 22 mm closer to the ECS drum, compared to dry material, was to maintain a minimum level of metals recovery and already an indication of the reduced effectiveness of the ECS.

The sensor grade for the wet material in Figure 3.10 is less accurate since the k varies substantially around the average 1.22, cf. Figure 3.6, and it is also not monotonic since the correct value drops with distance. Note that the product grade is monotonically increasing from 49% to 82%. The offset between the sensor and product grade has the same cause as for the case of dry feed. Here, the offset is much larger since also most of the smaller metal particles did not reach the sensor sample.

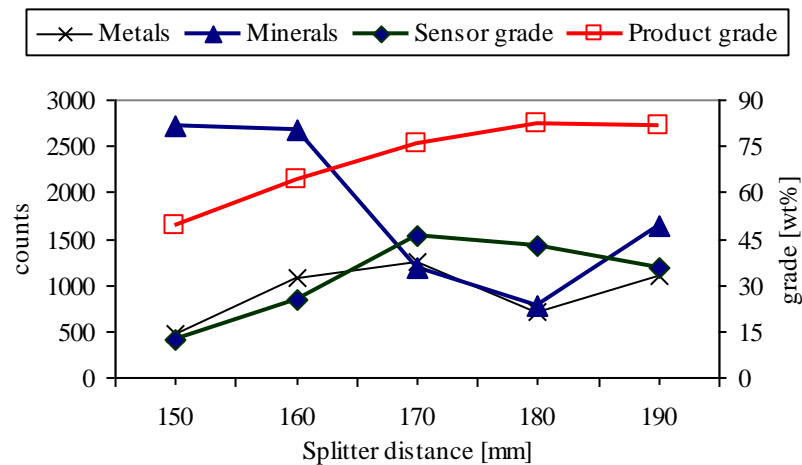


Figure 3.10: In-situ counts of mineral and metal particles, sensor grade ($k = 1.22$) and product bin grade for wet 1-6 mm bottom ash.

4 Conclusions

The functionality of the sensor unit was investigated for 1-6 mm ECS-processed bottom ash. The sensor data were integrated using a suitable time interval and measured grades were compared to manual analyses of the material that went through the sensor. The average and standard deviation for the differences in grade between the sensor measurements and the manual analyses were 0.0% +/- 1.8% using a moist batch in the laboratory with 10.7% moisture content, 1.5% +/- 6.0% in-situ using the dry ashes from batch I with 4.7% moisture content, and 3.1% +/- 11.8% in-situ using the wet ashes from batch I with 13% moisture content. A longer integration interval may average the variations in feed material more strongly. Crucial for measurement accuracy was the correct value of k , which is the ratio of average masses of mineral and metal particles. The measured average values and standard deviations were $k = 0.48 \pm 0.04$ in the laboratory, $k = 0.60 \pm 0.20$ in-situ for the dry ash and $k = 1.22 \pm 0.49$

in-situ for the wet ash. Using the average values for k proved sufficient for accurate grade measurement. The measurements and trends in sensor data from the laboratory and in-situ dry feed are quite comparable, considering the ECS machines were different and the bottom ashes came from different sources. The metals recovery (metals content ratio of product and feed) and grade both proved sensitive to the splitter distance. A 10 mm shift may produce 10% change in recovery or 18% change in grade, while over the range of 40 mm splitter distance the grade and recovery both change by at least a factor two. For wet feed the ECS segregation mechanisms changed remarkably, as k increased threefold and the number of counted particles reduces to a mere fraction of what was found for dryer bottom ash.

Consequently, when using very wet bottom ash the ECS effectiveness will drop as small metal particles either disappear in the intense minerals trajectory fan or stick to the feed conveyor belt and get scraped off directly into the minerals product. In-situ, the measured grade was consistently lower than the manually analysed product grade since the sensor sample was collected right next to the splitter, which was apparently not a representative spot for sampling the product grade. This may be resolved by moving the sampling tube further into the metal particles trajectory fan, dependent on the type of ECS. A differential behaviour in grade and overall metals recovery was found for increasing splitter distance. This implies that the optimum splitter distance to be used in ECS processing must be set, or controlled, on the basis of a sound compromise. In a commercial enterprise the compromise will of course be aimed at maximizing the revenues, which depend on product grade as well as on the recovery. In conclusion, the sensor unit may find its application in online product quality control or it may be used in automated control over the optimum ECS splitter distance.

References

- Ginés, O.**, Chimenos, J.M., Vizcarro, A., Formosa, J., Rosell, J.R., 2009. Combined use of MSWI bottom ash and fly ash as aggregate in concrete formulation: Environmental and mechanical considerations. *Journal of Hazardous Materials* 169 (1-3), 643-650.

- Maraspin, F.**, Bevilacqua, P., Rem, P., 2004. Modelling the throw of metals and non-metals in eddy current separations. *Int. J. Miner. Process.* 73 (2004) 1 – 11.
- Pretz, T.**, Julius J., 2011. Metal waste, in: Trevor M. Letcher and Daniel A. Vallero (Eds.), *Waste: A Handbook of Management*. Elsevier, ISBN: 978-0-12-381475-3, pp 95-99.
- Rahman Md. A.**, Bakker M. C. M., 2013, Sensor based control in eddy current separation of incinerator bottom ash, *Waste Management* 33, pp.1418-1424.
- Rem, P. C.**, Zhang, S., Forssberg ,E., De Jong, T. P.R., 2000. The investigation of separability of particles smaller than 5mm by eddy-current separation technology part II: Novel design concepts. *Magnetic and Electrical Separation*, Vol. 10, pp. 85-105.
- Schlomann, E.**, 1975. Separation of non-magnetic metals from solid waste by permanent magnets. I, Theory., *J. Appl. Phys.* 46, 5012–5021.
- Van Brecht, A.**, Konings A., 2011. Innovative and BREF proven material recycling of MSWI bottom ashes. Proceedings, second international valorisation symposium, 18 – 20 April 2011, Katholieke University, Leuven, Belgium.

Chapter 4

Eddy Current Belt Sensor-Conductivity Approach

This chapter presents the extension of the hybrid sensor research that led a fundamental research to the realization of an electromagnetic belt sensor for the identification of nonferrous (NF) metal scraps on a moving conveyor belt. This could facilitate, possibly in combination with other technologies, the multifunctional sensor sorting of metal scrap waste and related advanced waste materials processing. We focus here on developing the physical principle and methodology, building on the general principles of electromagnetic induction in conductive materials to enable the identification of NF metal scrap. A final design of the belt sensor and measured data will be presented in Chapter 5. The principle of the belt sensor has been presented details here and a method based on conductivity approach is formulated with a few assumptions for the identification of NF scraps on a conveyor. A parameter called conductivity indication factor (*CIF*) is defined on theoretical basis which is used for the identification of different NF metal scraps on a conveyor. The belt sensor involves two rectangular coils in Helmholtz configuration and a detector coil which is thought to be fixed underneath the belt. The Helmholtz coils generate two harmonic magnetic field components with a low and high frequency. The high frequency is defined as one for which the magnetic field is significantly influenced by the skin effect in the unknown metal particle, while the low frequency would fully penetrate the thickness of the unknown particle. The detector coil produces a voltage signal containing an amplitude modulated carrier wave (bias). The modulation signal is produced as the metal particle moves on the belt through the sensitive region between the two Helmholtz coils and afterwards the conductivity information is extracted by demodulation of the induced signal from the detector. However the contents of this chapter and the experimental results presented in Chapter 5 are neither published and nor presented anywhere to date but soon these will be submitted in a suitable journal.

4.1 Introduction

The non-contact detection of the conductivity of nonferrous (NF) metal particles translated on a conveyor belt is a challenge for online quality control and material processing, and specifically for the sorting of valuable nonferrous metals from waste streams. The eddy current technique is a vastly preferred method for the non-contact characterization of NF metals for its fast, simple and inexpensive outlook in this regard. The additional challenge is that also the shape, size and orientation of a target particle on the belt as well as lift-off between target and eddy current sensor these all have a strong influence on the detected signal. Despite the development of nondestructive eddy current sensors, for example for quality inspection, conductivity measurement, crack determination, and thickness measurement, still the technique struggles with the complexity in online applications if there is inherent variation in the types of metal particles being fed to the conveyor.

Quite a large number of publications deal with models for the eddy current setup, but commonly focus only on a specific particle shape. For example mathematical models for a perfect cylinder, plate or disk are useful for accurate calculation of the eddy current distribution (Krakowski, 1980 and 1979). Besides the limited validity for particle shapes, a disadvantage is that an accurate calculations of the eddy current using these models are time consuming and therefore not applicable for online quality inspection. It should be noted that in waste processing and sorting the conveyor belt carries the scrap metal particles at a velocity up to 1-2 meters per second and for that the effect of velocity on eddy current –is considered negligible (Nathan Ida 1988). Moreover, in waste streams the shape and size of scraps vary quite a lot. A commercial eddy current conductivity probe is more like a laboratory tool as it requires sample preparation according to specific size and shape. For example, the sigma-check conductivity probe model PSIG001 and sigmascope@smp10 are two latest model NDT probes that require sample preparation and specific measurement conditions which do not qualify for online testing in material processing and waste sorting.

This chapter presents the fundamental research for the proposed conductivity approach that applies the voltage data of an eddy current belt sensor. The sensor should be capable of noncontact identification of nonferrous (NF) metal particles translated by a conveyor belt through the field sensitive region of the belt sensor. This approach should enable the desired online quality control in material processing and waste sorting. The corresponding validation of the theory and test results using the experimental belt sensor and metal samples will be presented in Chapter 5.

4.2 Applied field and setup

This section presents details deduction of a sensor based detection system for identifying a NF metal particle on a conveyor belt by means of eddy current. Figure 4.1(a) shows the typical situation of the so called belt sensor, where a particle lays in its natural orientation on a conveyor and interacts with applied z-component dominating magnetic fields $\mathbf{B}_{1sum}^a = \mathbf{B}_{1sum} e^{-i\omega_1 t}$ and $\mathbf{B}_{2sum}^a = \mathbf{B}_{2sum} e^{-i\omega_2 t}$, associated with sufficiently low and high angular frequencies ω_1 and ω_2 . Two identical rectangular type bias coils L1 and L2 as shown in Figure 4.1(b) are used in a horizontal Helmholtz configuration to produce these fields, where L1 is placed below the belt and the L2 above it. A current of peak amplitude i_{p1} and i_{p2} for ω_1 and ω_2 , respectively, are fed from a voltage source with 50Ω internal resistance to L1 and L2. The total applied field at the surface of the belt is then \mathbf{B}_{1sum} at ω_1 and \mathbf{B}_{2sum} at ω_2 and can be broken down into vector components as:

$$\mathbf{B}_{1sum} = B_{1xsum}\hat{\mathbf{x}} + B_{1ysum}\hat{\mathbf{y}} + B_{1zsum}\hat{\mathbf{z}} \quad (4.1)$$

$$\mathbf{B}_{2sum} = B_{2xsum}\hat{\mathbf{x}} + B_{2ysum}\hat{\mathbf{y}} + B_{2zsum}\hat{\mathbf{z}} \quad (4.2)$$

Where for example B_{1xsum} is the vector sum of the peak amplitudes of the x components of the fields produced by the coils L1 and L2 simultaneously at ω_1 , and B_{2xsum} is the vector sum of the peak amplitudes of the x components of the fields produced by the coils L1 and L2 simultaneously at ω_2 , and so on.

The applied magnetic field components at a point in space, say $P(x,y,z)$, from the bias coils L1 and L2 can be calculated exactly using Matlab by summing the fields produced by each turn of the coils according to the literature (Herceg et al. 2009). Therefore the applied field components B_{1xsum} , B_{1ysum} , B_{1zsum} , B_{2xsum} , B_{2ysum} and B_{2zsum} can be expressed in the following way using the superposition principle:

$$B_{1xsum}\hat{x} = B_{1x}^{L1}\hat{x} - B_{1x}^{L2}\hat{x} \quad (4.3)$$

$$B_{1ysum}\hat{y} = B_{1y}^{L1}\hat{y} - B_{1y}^{L2}\hat{y} \quad (4.4)$$

$$B_{1zsum}\hat{z} = B_{1z}^{L1}\hat{z} + B_{1z}^{L2}\hat{z} \quad (4.5)$$

$$B_{2xsum}\hat{x} = B_{2x}^{L1}\hat{x} - B_{2x}^{L2}\hat{x} \quad (4.6)$$

$$B_{2ysum}\hat{y} = B_{2y}^{L1}\hat{y} - B_{2y}^{L2}\hat{y} \quad (4.7)$$

$$B_{2zsum}\hat{z} = B_{2z}^{L1}\hat{z} + B_{2z}^{L2}\hat{z} \quad (4.8)$$

Where for example B_{1x}^{L1} is the peak amplitude of the x component of the field produced on the belt surface by the coil L1 at frequency ω_1 , and B_{1x}^{L2} is the peak amplitude of the x component of the field produced on the belt surface by the coil L2 at angular frequency ω_1 , and so on.

The Helmholtz configuration is used specifically so that the field components B_{1zsum} and B_{2zsum} produced by the coils L1 and L2 are dominant at the surface of the belt compared to the field components B_{1xsum} , B_{2xsum} , B_{1ysum} and B_{2ysum} . Specifically, the configuration is designed such that the homogeneity of the fields B_{1zsum} and B_{2zsum} extends a region at least equal to the size of the largest metal particle used in the experiments. Therefore, for the symmetric homogeneous region on the belt surface, the total field can be approximated as

$$\mathbf{B}_{1sum} \cong B_{1zsum}\hat{z} \quad (4.9)$$

$$\mathbf{B}_{2sum} \cong B_{2zsum}\hat{z} \quad (4.10)$$

$$\mathbf{B}_{1sum}^a \cong B_{1zsum}\hat{z}e^{-i\omega_1 t} \quad (4.11)$$

$$\mathbf{B}_{2sum}^a \cong B_{2zsum}\hat{z}e^{-i\omega_2 t} \quad (4.12)$$

A symmetric z-field sensitive receiver, here a rectangular coil denoted as L3, is situated underneath the belt to detect the changes in the field due to a moving NF particle. The total field is the superposition of the applied field plus the scattered field produced by the eddy current running inside the NF particle. The size of the z-receiver L3 is sufficiently larger than the largest tested NF particle so it must will detect the main part of the produced scattered field.

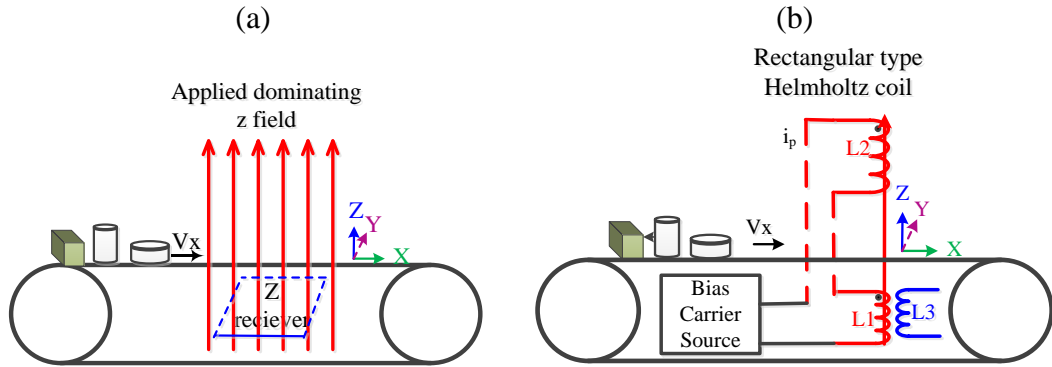


Figure 4.1: Typical situation of the belt sensor for the conductivity approach. (a) Shows the dominant and homogenous applied z-field for a certain frequency. A rectangular coil underneath to the belt detects the scattered field from the moving metal particle. (b) Shows two rectangular type coils L1 and L2 of the belt sensor connected in Helmholtz configuration to produce the dominant z-field components B_{1sum}^a and B_{2sum}^a at the surface of the belt for two possible excitation frequencies.

4.3 Magnetic moment of the reference particle

As a first step in the development of the full theory for the conductivity approach we introduce a reference type of particle: the thin metal disk. For this type of particle closed form analytical solutions exist for the effective (concentrated) magnetic moment generated by a uniform external magnetic field. The literatures (Rem 1999, Krakowski 1980 and 1979, Englert 1989) for an intuitive background of the four assumptions those have been made here to extent this solution for the particles of slightly other shapes and sizes and to obtain workable analytical expressions under two extreme frequency regimes in our experimental set-up. Therefore the four assumptions are:

1. The self-induction (i.e. the field coupling produced by eddy current in the same particle) exhibited by a thin metal disk is correctly accounted for in the approximating analytical expressions for the effective magnetic moment which are taken directly from the scientific literature. This

means the related complex impedance of the thin disk represents realistically its inductance (imaginary part) and energy absorption (real part) properties. When extending this magnetic moment to particles that have slightly other shapes and are slightly thicker, the expressions are assumed to remain valid.

2. The effect of mutual induction between the combined impedance of the power source and transmission coils and the particle is negligible. This assumption relies on the field scattered by the particle being much weaker than the applied magnetic field at the location of the particle, which is mainly challenged by the larger and highly conductive metal particles.
3. The eddy current at the high frequency ω_2 are fully concentrated at the surface according to a strong skin effect, meaning the particles are considered ‘thick’ at each point of their surface.
4. On the other hand the skin depth for the low frequency ω_1 is larger than the thickness of the particle, meaning the particles are considered ‘thin’ at each point of their surface.

In accordance with the preceding assumptions, the two angular frequencies ω_1 and ω_2 of the applied fields are chosen such that ω_1 is sufficiently low and ω_2 is sufficiently high for the case of a uniform disk particle. The radius is R_{disk} , the thickness $d_{disk} < R_{disk}$ and $A_{disk} = \pi(R_{disk})^2$. The z-component of the effective magnetic moment for this reference particle are denoted as $\mathbf{m}_{1z\text{eff}}^{disk}$ at ω_1 , and $\mathbf{m}_{2z\text{eff}}^{disk}$ at ω_2 and can be approximated by (Rem 1999, pp.123):

$$\mathbf{m}_{1z\text{eff}}^{disk} \cong -(1/8\pi)(A_{disk})^2 d_{disk} \sigma \frac{dB_{1sum}^a}{dt} \quad [\text{A.m}^2] \quad (4.13)$$

$$\cong -i(1/8\pi)(A_{disk})^2 d_{disk} \sigma \omega_1 \mathbf{B}_{1sum}^a \quad [\text{A.m}^2] \quad (4.14)$$

$$\cong -i(1/8\pi)(A_{disk})^2 d_{disk} \sigma \omega_1 B_{1zsum} \hat{\mathbf{z}} e^{-i\omega_1 t} \quad [\text{A.m}^2] \quad (4.15)$$

$$|\mathbf{m}_{1z\text{eff}}^{disk}| \cong (1/8\pi)(A_{disk})^2 d_{disk} \sigma \omega_1 B_{1zsum} \quad [\text{A.m}^2] \quad (4.16)$$

and

$$\mathbf{m}_{2z\text{eff}}^{disk} \cong -(8/3) (A_{disk}/\pi)^{(3/2)} \mathbf{B}_{2sum}^a / \mu_0 \quad [\text{A.m}^2] \quad (4.17)$$

$$\mathbf{m}_{2z\text{eff}}^{disk} = -(8/3) (A_{disk}/\pi)^{(3/2)} B_{2zsum} \hat{\mathbf{z}} e^{-i\omega_2 t} / \mu_0 \quad [\text{A.m}^2] \quad (4.18)$$

$$|\mathbf{m}_{2z\text{eff}}^{disk}| \cong (8/3) (A_{disk}/\pi)^{(3/2)} B_{2zsum} / \mu_0 \quad [\text{A.m}^2] \quad (4.19)$$

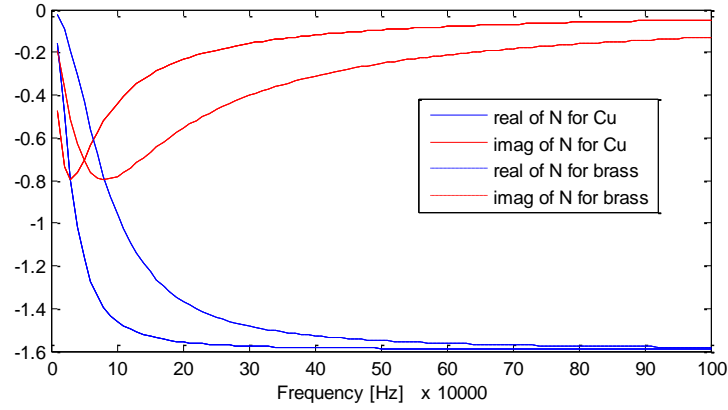


Figure 4.2: Shows the calculated real and imaginary parts of N_ω for pure Cu ($\sigma=5.97e7$ S/m) and Brass (15% Zn, $\sigma=2.21e7$ S/m) for a disk radius of 3 mm and thickness 1mm.

The dependence of the disk particle response on frequency may be investigated through its complex magnetic field impedance N_ω :

$$N_\omega = R_\omega + iI_\omega \quad (4.20)$$

$$R_\omega = -\left(0.6\pi d_{disk} \frac{x^2}{R_{disk}}\right) / \left\{64 + (0.6\pi d_{disk})^2 \frac{x^2}{R_{disk}^2}\right\} \quad (4.21)$$

$$I_\omega = -8x / \{64 + (0.6\pi d_{disk})^2 x^2 / R_{disk}^2\} \quad (4.22)$$

$$x = \mu_0 \omega \sigma R_{disk}^2 \quad (4.23)$$

Figure (4.2) shows an example of the real and imaginary components of the impedance for varying frequency. Clearly, in this case below ~ 20 kHz the N_ω is complex and holds both particle size and conductivity information. On the other hand, above ~ 30 kHz the real part of N_ω dominates and holds information only on the effective calibrated projection $C2$ of the disk particle as the eddy current are confined to a few skin depths at the particle surface.

4.4 Conductivity approach for the belt sensor

In theory, each type of particle produces its own unique field pattern. However, due to the technical limitations to the size, possible positions and sensitivity of magnetic field detectors, different particles may in fact produce quite similar field data. For example, the field from a flat copper particle with a square base and the field for a flat one with a round base and same base surface size turn out to be quite similar. Also, if two copper particles have the same base

size and height and only quite small cross sectional variations the magnetic field may turn out to be quite similar. However, for visibly larger deviations in cross-section shape of two particles, even if they are the same height, the magnetic response may vary more substantially. In contrary, two similar shaped particles of brass and copper remain quite different whatever the particle height. These insights lead to the following three assumptions that form the basis for the full theory behind the conductivity approach:

Conductivity approach assumption 1:

The effective magnetic moment of a flat disk with thickness d_{ref} may represent the moment of a different flat particle with a more complicated base shape, provided they have the same effective radius and thickness. For example, Figure 4.3(a) and (b) shows the example for a rectangular and a disk shaped plate. Assumption 1 implicitly involves that the self-induction of the particle and the mutual-induction between the particle and the power source-transmission coils remain practically the same if the particle size remains overall the same and the shape varies only within reasonable limits. These implicit assumptions are thought to be quite acceptable in view of the design of the experimental setup and the envisioned industrial application to bottom ash metals.

Conductivity approach assumption 2:

The height of an arbitrary metal scrap particle influences the scattered field and thus the effective magnetic moment. The amplitude enhancing influence of the particle height on the detected voltage is approximated by departing from the reference disk model, using the disk thickness d_{ref} , and scaling the disk magnetic moment by replacing the true disk surface A_{disk} by the projection of the magnetic field onto the z-receiver surface, which is parallel to the belt surface. The experimental value for the projected surface may for example be estimated from the peak amplitude of the demodulated signal of the particle (to be denoted as V_z^p). Note therefore that the particle is translated by the belt over the receiver surface. However, this new parameter cannot be interpreted in absolute form, and should therefore be weighed against the known (calibrated) projection produced by a reference flat disk particle. In conclusion, the approach to account for the height influence of an

arbitrary particle when using the equations for a reference flat disk particle is to multiply the true surface A_{disk} of the reference flat disk particle by a parameter $C2$, which states how much larger the projected surface of the unknown particle is with respect to the reference particle:

$$C2 = A_{eff} / A_{eff}^{disk} \quad (4.24)$$

Here A_{eff} denotes the projected field surface for the unknown particle and A_{eff}^{disk} is the calibrated (measured) projected field surface for the reference flat disk particle. Figure 4.3(c) shows the example of a block-shaped particle with magnetic moment $m_{z_{eff}}^{block} \hat{\mathbf{z}}$. Assumption 2 implicitly involves that the effect of mutual induction between the larger particle and the power source-transmission coils remains negligible. It also implicitly assumes that the effect of self-induction of the true magnetic moment for the larger particles will scale with the detected increase in the signal received from the larger particle. The accuracy of the latter implicit assumption has to be tested in Chapter 5, because the precise effects of an increase in particle size as well as some arbitrary change in its shape on the complex particle impedance is rather difficult to predict.

Conductivity approach assumption 3:

The effective surface A_{eff} for a high particle and therefore parameter $C2$ are practically the same for both frequencies ω_1 and ω_2 . This assumption allows further on for an explicit analytical solution to be derived for $C2$.

For the block particle in Figure 4.3(c) the height $h > d_{ref}$ and the eddy current induced in the vertical surface of the block create a stronger and wider magnetic field than for a thin disk. However, in accordance with our above full theory assumptions, we will depart from Eqs. (4.13) to (4.19) and use them also for the high particles by using the effective parameter $C2$ to scale the real field strength of the block particle. To this end, Eq.(4.15) and (4.18) are rewritten for the case of a high particle with $A_{eff} = C2A_{disk}$, where the subscript ‘disk’ now refers to the exact properties of the reference flat disk particle:

$$\mathbf{m}_{1z_{eff}}^p \cong -i(1/8\pi)(C2A_{disk})^2 d_{disk} \sigma \omega_1 B_{1zsum} \hat{\mathbf{z}} e^{-i\omega_1 t} \quad [\text{A.m}^2] \quad (4.25)$$

$$\mathbf{m}_{2z_{eff}}^p \cong -(8/3) (C2A_{disk}/\pi)^{3/2} B_{2zsum} \hat{\mathbf{z}} e^{-i\omega_2 t} / \mu_0 \quad [\text{A.m}^2] \quad (4.26)$$

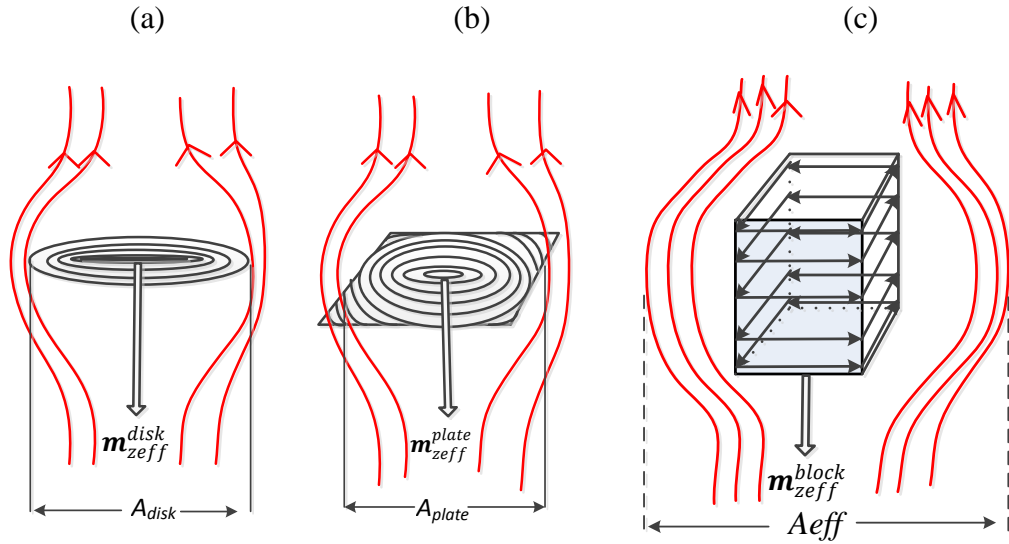


Figure.4.3: Shows the main field lines and induced effective magnetic moment for different particles. (a) $m_{z_{eff}}^{disk} \hat{z}$ of a flat and round disk (b) $m_{z_{eff}}^{plate} \hat{z}$ of a square flat plate which may be approximated by the round disk, i.e. $m_{z_{eff}}^{disk} \hat{z} = m_{z_{eff}}^{plate} \hat{z}$. (c) $m_{z_{eff}}^{block} \hat{z}$ of a high block-shaped particle with its as yet unknown parameter called the effective field projection A_{eff} .

These point sources (magnetic moments) form the basis for the conductivity approach by which unknown particles on a conveyor shall be characterized from field measurements. It is noted that for experimental validation in Chapter 5 we will restrict the range of possible metal particles to generic shapes such as the flat disk, flat plate, disk block, square block, rod and cylinder, and the materials copper, brass and aluminum.

4.5 Detected field of the z-receiver

4.5.1 Detected field response

The next step is to calculate the particle magnetic field received by the z-receiver that is positioned below the belt and symmetrical with respect to the Helmholtz coils. To this end we introduce the vector potentials, A_{1z}^p and A_{2z}^p at a point P (x, y, z) inside the z-receiver surface. The origin (0,0,0) of the coordinate system is here chosen on the surface of the belt and symmetrical with the center of the z-receiver. The vector potentials appear in vector products that are computed since the particle is effectively replaced by a magnetic source whose strength is equal to its effective magnetic z-moment:

$$\mathbf{A}_{1z}^p = \frac{\mu_0}{4\pi r^2} (\mathbf{m}_{1z\text{eff}}^p \times \hat{\mathbf{r}}) \quad (4.27)$$

$$\mathbf{A}_{2z}^p = \frac{\mu_0}{4\pi r^2} (\mathbf{m}_{2z\text{eff}}^p \times \hat{\mathbf{r}}) \quad (4.28)$$

Here $r = \text{sqrt}(x^2 + y^2 + z^2)$ is the scalar distance from the origin (0,0,0) on the surface of the belt to the point P(x, y, z) and $\hat{\mathbf{r}}$ is the unit vector. It is noted the origin is chosen on the belt surface in a point of symmetry with respect to the z-receiver. The scattered particle magnetic fields \mathbf{B}_{1z}^p and \mathbf{B}_{2z}^p inside the z-receiver point P(x, y, z) for ω_1 and ω_2 , respectively, can be calculated by taking the curl (Evgeny V. André Thess V. 2012) of Eq.(4.27) and Eq.(4.28):

$$\mathbf{B}_{1z}^p = \frac{\mu_0}{4\pi r^2} \nabla \times \mathbf{A}_{1z}^p \quad (4.29)$$

$$\mathbf{B}_{1z}^p = \frac{\mu_0}{4\pi} f_1 \mathbf{m}_{1z\text{eff}}^p \quad (4.30)$$

$$\mathbf{B}_{1z}^p = -i(1/32)(C2A_{\text{disk}})^2 d_{\text{disk}} \sigma \mu_0 \omega_1 B_{1z\text{sum}} f_1 \hat{\mathbf{z}} e^{-i\omega_1 t} \quad (4.31)$$

$$|\mathbf{B}_{1z}^p| = (1/32)(C2A_{\text{disk}})^2 d_{\text{disk}} \sigma \mu_0 \omega_1 B_{1z\text{sum}} f_1 \quad [\text{V.S.m}^{-2}] \quad (4.32)$$

and

$$\mathbf{B}_{2z}^p = \frac{\mu_0}{4\pi r^2} \nabla \times \mathbf{A}_{2z}^p \quad (4.33)$$

$$\mathbf{B}_{2z}^p = \frac{\mu_0}{4\pi} f_1 \mathbf{m}_{2z\text{eff}}^p \quad (4.34)$$

$$\mathbf{B}_{2z}^p = -(2/3) (C2A_{\text{disk}})^{3/2} B_{2z\text{sum}} f_1 / \pi^{5/2} \hat{\mathbf{z}} e^{-i\omega_2 t} \quad (4.35)$$

$$|\mathbf{B}_{2z}^p| = (2/3) (C2A_{\text{disk}})^{3/2} B_{2z\text{sum}} f_1 / \pi^{5/2} \quad [\text{V.S.m}^{-2}] \quad (4.36)$$

$$\text{Where } f_1 = 3z^2/r^5 - 1/r^3 \quad (4.37)$$

The total magnetic flux density detected in the point P(x,y,z) for a fixed angular frequency is the vector sum of the applied field and the scattered field produced by the particle. By integrating over the whole z-receiver surface the total detected voltage shall be obtained. Without a particle present, the receiver voltage is determined only by the applied field, resulting in a bias voltage. When a particle is translated by the belt (belt speed is V_x) in and out of the applied z-field, the particle's response changes the total magnetic field in the z-receiver, which effectively modulates the amplitude of the bias carrier voltage. In the following we neglect the amplitude effects when the particle moves in and out the z-receiver surface, and we may leave out the trivial time-dependent term

(complex exponent) to calculate the total received voltage for frequencies ω_1 and ω_2 by the finite z-receiver for a coil with one turn as:

$$V_{1z}^{tot} = - \left\{ \omega_1 \oint_{-l_y/2}^{l_y/2} \oint_{-l_x/2}^{l_x/2} (|B_{1sum}^a| - |B_{1z}^p|) dx dy \right\} \quad [\text{V/turn}] \quad (4.38)$$

$$V_{2z}^{tot} = - \left\{ \omega_2 \oint_{-l_y/2}^{l_y/2} \oint_{-l_x/2}^{l_x/2} (|B_{2sum}^a| - |B_{2z}^p|) dx dy \right\} \quad [\text{V/turn}] \quad (4.39)$$

The bias carrier voltage due to the terms $|B_{2sum}^a|$ or $|B_{1sum}^a|$ is of much higher frequency than the modulated amplitude response of the particle crossing the z-receiver. This must be utilized to efficiently filter out the bias by means of a suitable amplitude demodulation technique plus low-pass filter to isolate the peak amplitude response of the particle. After substituting Eq.(4.32) and (4.36) in Eq.(4.38) and (4.39) respectively, the demodulated peak particle response voltages are denoted by V_{1z}^p and V_{2z}^p for frequencies ω_1 and ω_2 can be written as

$$V_{1z}^p = (1/32)(C2A_{disk})^2 d_{ref} \sigma \mu_0 \omega_1^2 B_{1zsum} \left\{ \oint_{-l_y/2}^{l_y/2} \oint_{-l_x/2}^{l_x/2} f_1 dx dy \right\} [\text{V/turn}] \quad (4.40)$$

$$V_{2z}^p = (2/3) (C2A_{disk})^{3/2} \omega_2 B_{2zsum} \left\{ \oint_{-l_y/2}^{l_y/2} \oint_{-l_x/2}^{l_x/2} f_1 dx dy \right\} / \pi^{5/2} [\text{V/turn}] \quad (4.41)$$

Note that a minus sign in both demodulated peak voltages is omitted because it has no bearing on the data interpretation. The integral (I) in these equations was evaluated in Maple using the known dimensions of the square experimental z-receiver L3: 30 mm by 30 mm, located at -8 mm below the origin (i.e. the belt surface). It is assumed here without loss of generality that point P lies in the center of the z-receiver, so its coordinates are P(0,0, -0.008). This integrates to $I = 274.72 \text{ [m}^{-1}\text{]}$.

Therefore, Eq. (4.40) and Eq.(4.41) can be simplified to:

$$V_{1z}^p = 8.59 (C2A_{disk})^2 d_{disk} \sigma \mu_0 \omega_1^2 B_{1zsum} \quad [\text{V/turn}] \quad (4.42)$$

$$V_{2z}^p = 10.5 (C2A_{disk})^{3/2} \omega_2 B_{2zsum} \quad [\text{V/turn}] \quad (4.43)$$

These equations represent the signal peak amplitude of the demodulated and filtered z-field response of a particle at ω_1 and ω_2 . This leaves only $C2$ and σ to be determined as the unknown particle parameters that characterize the unknown particle from two voltage measurements. Note that the choice for the reference disk surface A_{disk} is not critical, but it should ideally be close to that of the unknown particle. Therefore, it is expected the conductivity approach will be more accurate if the unknown metal particles fall in a smaller size range, for example by sieving the metal scraps and choosing the optimum size-matched reference disk particle for each size category. On the other hand, it is mandatory that d_{disk} is thin (large skin depth) for ω_1 and thick (small skin depth) for frequency ω_2 . After measuring the calibration value A_{eff}^{disk} for the reference disk particle, the $C2$ of the unknown particle shall be obtained from the high-frequency measurement of the unknown particle using Eq. (4.43). Now solving for real root of $C2$ from Eq.(4.43) that yields:

$$C2A_{disk} = A_{eff} = 0.208(V_{2z}^p B_{2zsum}^2 \omega_2^2)^{2/3} / (B_{2zsum}^2 \omega_2^2) \quad (4.44)$$

Using the Eq.(4.44) the $C2$ from high frequency response of a particle will be measured that states how much larger or smaller the projected surface field of a particle of an arbitrary shape with respect to the reference disk. So the $C2$ is expected to be different for every high particle of different shapes. Then, by substituting $C2$ into the low frequency equation Eq. (4.42) the conductivity will be calculated, which concludes the characterization of the unknown particle.

4.5.2 Conductivity Indication Factor (CIF)

As an alternative to substituting the measured $C2$ directly into Eq. (4.42) it is instructive to introduce the parameter CIF as a ratio of the high- and weighted-low frequency response, leading to equivalent expressions:

$$CIF = V_{1z}^p / \left(V_{2z}^p (C2A_{disk})^{1/2} d_{disk} \right) \quad (4.45)$$

$$= 0.818 \mu_0 \omega_1^2 B_{1zsum} / (\omega_2 B_{2zsum}) \sigma \quad (4.46)$$

The Eq.(4.46) shows ideal linear relation between CIF and conductivity that must be the conductivity which will be experimentally measured with the help of the Eq.(4.45) for conductivity classification purposes because it is independent of the

particle shape. Once the *CIF* of a given particle is measured we can solve Eq.(4.46) for σ , according to:

$$\sigma = 1.222 \text{ CIF } \omega_2 B_{2zsum} / (\mu_0 \omega_1^2 B_{1zsum}) \quad (4.47)$$

Moreover, by taking measurements of ideal flat plates with known conductivities at the two frequencies and known magnetic fields, one may build a database of tested conductivities and *CIF* classes for a more robust statistical identification of the unknown metal type.

4.6 Conclusions

This chapter presents the methodology, assumptions and approximations leading to explicit equations for the detected magnetic fields from which an unknown NF metal particle will be characterized on the basis of two unknowns from two frequency measurements. The conductivity approach requires the measurement of only the z-field component of the scattered field produced by the moving metal particle at two frequencies. The high applied frequency results in a very small skin depth and the low applied frequency in a very large skin depth in a reference flat disk particle, allowing for high and low approximations of the produced scattered field. The theory is built by approximating the magnetic moment of a true particle by modifying the approximated moment of the reference disk particle. The field produced by the magnetic moment is then integrated over the finite receiver surface (square coil) to yield the detected peak voltage signal. The high frequency bias voltage due to the applied field is efficiently removed from the received signal using amplitude demodulation and a low pass filter.

The first unknown in the resulting expressions for the detected voltage Eq. (4.42) and (4.43) is a shape and height dependent factor *C2* and the second the conductivity σ . While the latter may in principle be sufficient in many applications, for waste materials there is larger uncertainty in the conductivity measurement due to the large range of possible alloys. Fortunately, the shape and size of a waste metal scrap are often both correlated due to the original

functionality of the metal scrap. For example, wires are mostly copper and sometimes aluminum or non-magnetic stainless steel. Therefore, the combination of the two parameters produced by the conductivity approach make it possible to apply more robust statistical methods using correlation and classification, which is usually done in combination with calibrations using documented samples. It is remarked that this is beyond the scope of the present work.

The voltage expressions may be manipulated to derive Eq.(4.45) with a parameter (*CIF*) that allows the conductivity to be measured through a calibration approach or indirectly by using statistical methods. The approximations leading up to Eq. (4.46) state that the conductivity may be estimated from just two measurements at two different frequencies, independent of the physical and geometrical properties of the unknown NF metal particle. It is intuitively clear that this could only be accurate if the size, shape and conductivity of the unknown particle stay within certain limits. Therefore, the main challenge for Chapter 5 is to experimentally explore the ranges of validity of the conductivity approach and thus of the assumptions and approximations behind Eq. (4.42) to (4.46).

References:

- Englert G.W.**, 1989, Parametric study of power absorption from electromagnetic wave by small ferrite spheres, NASHA Technical Paper 2949.
- Evgeny V. André Thess V.** 2012, Interaction of a magnetic dipole with a slowly moving electrically conducting plate, J. Eng. Mathematics, Vol. 53(2), ISSN 0022-0833.
- Herceg D., Juhas A. and Milutinov M.**, 2009, A Design of a Four Square Coil System for a Bio-magnetic Experiment, SER. ELEC. ENERG.Vol.22(3), pp.285-292.
- Krakowski M.** 1980, Eddy Currents in Solid Induced by Time -Harmonic Magnetic Field, Buletine De L'Academie Polonaise Des Sciences Series Des Sciences Techniques, Volume XXVIII (9-10).
- Krakowski M.** 1979, Eddy Currents in Thin Plates Induced by Time -Harmonic Magnetic Field, Buletine De L'Academie Polonaise Des Sciences Series Des Sciences Techniques, Volume XXVII (12).
- Nathan Ida**, 1988, Modeling of velocity effects in eddy current applications, J. Appl. Phys. Vol.63, 3007; <http://dx.doi.org/10.1063/1.340929>.
- Rem P. C.** Eddy Current Separation, Eburon, ISBN 90-5166-702-8, copyright©1999 P.C. Rem.

Chapter 5

Experimental Results of the Eddy Current Belt Sensor

This chapter presents the experimental results of the belt sensor where the approximate theory behind the conductivity approach as explained in Chapter 4 is evaluated with the measured response of the sensor unit using two representative samples of non-ferrous (NF) metal particles. However, in order to do that, first the belt sensor is characterized in terms of its operating frequencies, bias current, distribution of the magnetic field components on the surface of the belt, and sensitivity for detecting the sample particles. The two samples sets S1 and S2 are used to observe the performance of the sensor for the identification of different NF metals based on their measured values of *CIF* values (conductivity indication factor) using the Eq.(4.45) as explained in Chapter 4. The sample set S1 consists of the pure metals Cu, Al, and Brass, and each metal is used for particles of these six generic shapes: disk, disk block, square plate, square block, rod and cylinder.

On the other hand the sample set S2 contains a representative amount of bottom ash metal scraps that is used as an application of the belt sensor for the identification of different true scrap metals (Cu, Al, Brass and Zn) in the bottom ash material. As a first step towards an application of the belt sensor, this chapter also presents a logical sorting statistics of the bottom ash scraps based on their average *CIF* values. Moreover, the calculated and calibrated conductivity values of the metal scraps using only the belt sensor are also presented.

5.1 Details of the belt sensor and experimental set up¹

This section aims to presents the constructional details of the belt sensor. Figure 5.1(a) and (b) show a sketch and the built experimental set up of the belt sensor, respectively. The two identical rectangular coils L1 and L2 both have 53 windings and are symmetrically connected in series in a Helmholtz configuration

¹All experimental parts including design, construction, and characterization of the presented eddy current belt sensor are completed at the Resources and Recycling laboratory, faculty of Civil Engineering and Geosciences, Delft University of Technology, Netherlands.

to act as the magnetic bias field coils of the sensor unit. The reason for using the Helmholtz configuration is to produce a net z-dominating homogenous magnetic field from its components $B_{1zsum}\hat{z}$ and $B_{2zsum}\hat{z}$ on the surface of the belt at two operating frequencies f_1 and f_2 . Table 5.1 shows the geometrical and electrical specifications of the coils. The fields $B_{1zsum}\hat{z}$ and $B_{2zsum}\hat{z}$ are produced separately by supplying a peak bias current, denoted as $i_{p1}(f_1)$ and $i_{p2}(f_2)$, from an Agilent signal generator, powered by an external amplifier. The output voltage of the signal generator was the same for each frequency but the current were off course different at different frequencies. The resulting magnetic field distribution is presented in Section 5.3.2.

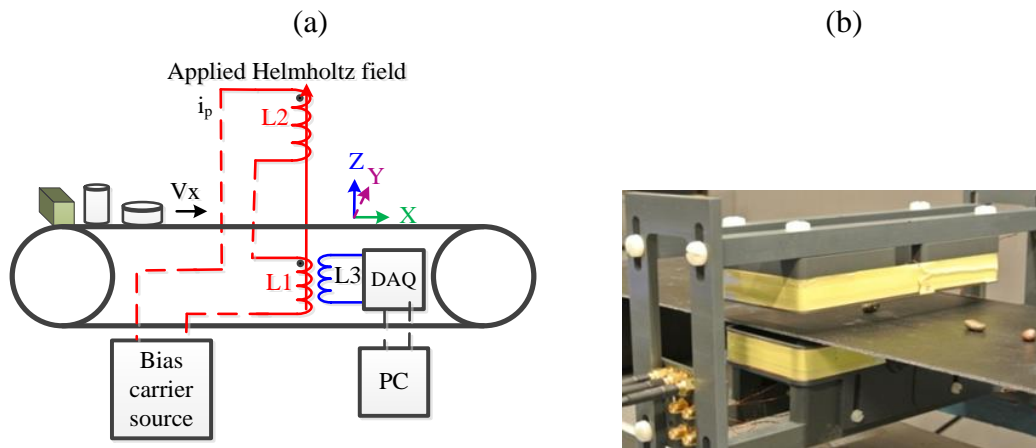


Figure 5.1: (a) A sketch of the belt sensor with two bias coils L1 and L2 and one z-field sensitive receiver coil L3. (b) Experimental set up of the belt sensor.

Table 5.1: Specifications of the belt sensor

Coil	l_x	l_y	l_z	$R_{Heq.}$	h	z_0	n	f_1	f_2	i_{p1}	i_{p2}
	[mm]	[mm]	[mm]	[mm]	[mm]	[mm]	--	[kHz]	[kHz]	[mA]	[mA]
L1	30	75	9	53.2	38	-8	53	5.0	93.0	411.6	66.3
L2	30	75	9	53.2							
L3	15	15	0.5	--							

Where,

z_0 = the vertical z distance measured from the symmetric center point on the top surface of the belt to the center point of the thin z receiver coil L3;

l_x =half-length along x axis of the coils;

l_y =half-length along y axis of the coils;

l_z =half-length along z axis of the coils;

R_{Heq} =equivalent radius of the rectangular Helmholtz coil cross section;

h =center to center z-distance between the coils L1 and L2;

The width of the belt (along the y-axis) was slightly smaller than the y-length of the rectangular Helmholtz coils, which helped to keep the field homogeneous along the whole width of the belt. The calculated value of the bias coil inductances was $L1=L2=240.4 \mu\text{H}$ using the appropriate values of the coefficients for short and long coil approximations (cf. Grover W. F., 1973). A vertically thin-wounded z-field sensitive receiver coil L3 with 53 windings, called z-receiver for short, is aligned horizontally with L1 and is placed just underneath the belt. A desktop computer is used to log the data through a DAQ module connected with the z-receiver. For convenience the working expressions of the belt sensor as deduced in Chapter 4 are summarized below:

$$C2A_{disk} = A_{eff} = 0.208 V_{2z}^{p2/3} / (B_{2zsum}^2 \omega_2^2)^{1/3} \quad (5.1)$$

$$CIF = V_{1z}^p / \left((C2A_{disk})^{\frac{1}{2}} V_{2z}^p d_{disk} \right) \quad (5.2)$$

$$\sigma = 1.222 CIF \omega_2 B_{2zsum} / (\mu_0 \omega_1^2 B_{1zsum}) D_{metal} \quad (5.3)$$

Where,

D_{metal} = multiplicative calibration constant to convert to accurate conductivity values, determined as the average calibration value for a known sample set of one specific type of metal.

$C2$ = effective parameter which is used to calculate the effective projected field surface of a particle with respect to a disk as observed by the z-receiver;

V_{1z}^p = peak amplitude per turn of the demodulated signal of a particle detected by the z receiver at the operating frequency f_1 ;

V_{2z}^p = peak amplitude per turn of the demodulated signal of a particle detected by the z receiver at the operating frequency f_2 ;

B_{2zsum} / B_{1zsum} = peak amplitude of the dominating z-field component of the Helmholtz coils on the surface of the belt, which is the vector sum of the z-components of the fields produced by the individual coils L1 and L2 at operating frequency f_2 / f_1 ;

A_{disk} = surface area of the reference disk;

$\omega_2 = 2\pi f_2$;

CIF = Conductivity indication factor, which is characteristic for the identification of the NF metal particles;

d_{disk} = thickness of the reference disk;

σ = conductivity;

$\omega_1 = 2\pi f_1$;

μ_0 = magnetic permeability of free space.

The Eq. (5.1) is used to measure the parameter $C2$ of a particle with respect to the effective projected surface of a reference disk at the natural (most probable) orientation of the particle on the flat belt. The Eq. (5.2) is used to produce a statistical database of average CIF values (conductivity indication factor) for the purpose of identifying nonferrous metals as based on the conductivity approach discussed in Chapter 4. The Eq.(5.3) is used to calculate the conductivity of a nonferrous particle using the measured CIF value. It is also instructive to eliminate the parameters $C2$ and CIF from Eq. 5.1 to 5.3 and leave out the calibration D_{metal} . That shows that the final conductivity is obtained in terms of ratios of the incident and detected fields, as

$$\sigma = 2.69 (B_{2zsum}\omega_2)^{(4/3)} / (B_{1zsum}\omega_1) \times V_{1z}^p / (V_{2z}^p)^{(4/3)} \times 1 / (\omega_1\mu_0 d_{disk}) \quad (5.4)$$

5.2 Sample materials²

Two sets of samples, named S1 and S2, are prepared for different purposes. Figure 5.2 (a) shows the sample set S1 that is used as a reference set (the known particles set). It consists of total 18 particles of the basic shapes of different materials Cu, Al and Brass. The sizes and generic shapes of the samples are listed in Table 5.2 where it is noted the block particles were more than 3 times higher than the flat plate or flat disk particles. These reference particles are used to validate the conductivity approach for the identification of the different nonferrous metals using the measured *CIF* values. On the other hand, Figure 5.2(b) shows the sample set S2 of different types of nonferrous metal scraps of various shapes and sizes as collected by manual sieving of a batch of real bottom ash metal scraps to the size range 6.5 mm to 15 mm. This batch S2 contained 114 metal scraps in composition: Cu=24, Al=30, Brass=41 and Zn=19. It is noted that in batch S2 the Cu scraps were relatively small while the Al scraps were relatively flat and looked more like droplets due to their low melting temperature and stay in the incineration furnace. The true conductivity of the scraps in sample set S2 was completely unknown at forehand.

Table 5.2: Specifications of pure sample set S1. Circular particles have a diameter of 11.3 mm and square ones have a cross section of 10 x 10 mm.

Sample	Cross section type	Base surface	Height
Disk	Circular	100 mm ²	3mm
Disk block	Circular	100 mm ²	10mm
Plate	Square	100 mm ²	3mm
Square block	Square	100 mm ²	10mm
Rod	Circular	100 mm ²	10mm
Cylinder	Circular	100 mm ² with wall thickness 3mm.	10mm

²All sample materials presented in this chapter are prepared at the Resources and Recycling Laboratory, faculty of Civil Engineering and Geosciences, Delft University of Technology, Netherlands.

Moreover, the conductivity could not directly be measured using the standard NDT conductivity probe because for that purpose the scraps would have to be heated and flattened by hammering to fit with the NDT probe sample requirements. However, the latter preprocessing would have destroyed the sample set in terms of shape and size, and could also have affected the conductivity of the scrap in its original form. Therefore, the calibration with the reference NDT probe could only be done after it was sure all the relevant measurements were taken with the belt sensor. The sample set S2 is used to study the nonferrous bottom ash scraps of inherently complicated shapes and sizes as a step towards the application of the belt sensor for sorting of metal waste materials on the basis of measured *CIF* values.

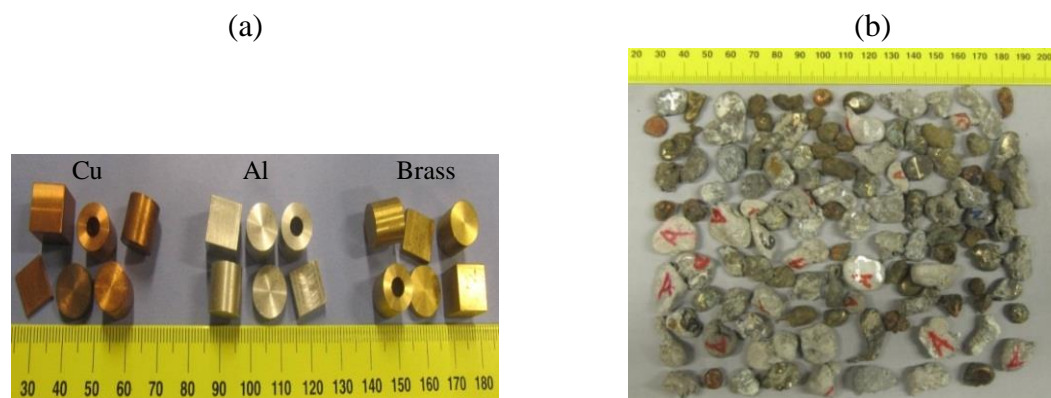


Figure 5.2: (a) The pure-metal reference sample set S1 with Cu, Al and Brass, each with six generic shapes. (b) The sample set S2 with 114 real bottom ash scraps of Cu, Al, Brass and Zn with complicated shapes and unknown conductivity.

5.3 Experimental results

5.3.1 Operating frequency of the sensor

The aim of this section is to determine the two most appropriate operating frequencies f_1 and f_2 of the sensor in accordance with the assumptions made for the conductivity approach described in Chapter 4. In a pragmatic approach, the detection sensitivity of the sensor should be sufficient as to allow for a clear and distinguishing magnetic response of the sample particles. The sensor response is investigated at various frequencies using the reference particles of the sample set S1. Per metal type, the six generically shaped particles were adhered to the belt in

a stable natural position using sticky tape with some spacing in between as to prevent cross-talk between the subsequent particle responses. It is noted the tape prevented the particles from moving when starting up the conveyor belt, but in a continuous operational process this would of course not be required. Next, the belt is moved at the constant velocity $V_x = 0.35$ m/s and the particles interact with the sensor during their journey through the Helmholtz bias field and induce an amplitude modulated signal in the z-receiver. Each measurement is repeated at least once and the measurements are stored and later analyzed in Matlab. Amplitude demodulation technique is used to extract the responses of the particles in each set of measurements.

The observed modulation depths at the frequencies ω_1 and ω_2 varied from 1.1% to 2.1%, which was strong enough to eliminate the noise. Figure 5.3(a) and (b) show the demodulated signals of the particles of sample set S1 at sufficiently low frequency around $f_1=5.0$ kHz and at sufficiently high frequency $f_2=93.0$ kHz, respectively. At the low frequency the conductivity information of the particles appears to be noticeable in the signal amplitudes, but at the high frequency it is not. This implies that at low frequency response the magnetic field impedance N_ω is complex and at high frequency it is real (cf. Figure 4.2 in Chapter 4). The effect of the height of the block particles is quite noticeable in the signal amplitudes at both frequencies, but the effect of the shape of the particles is not. To verify, the sensor was also investigated around 3.0 kHz, 4.0 kHz, and 8.0 kHz and those tests confirmed that the conductivity information gradually disappears as the frequency increases.

In fact, the conductivity information was quite prominent in the signal amplitude at relatively low frequencies. In a compromise with an adequate signal to noise ratio, the $f_1 = 5.0$ kHz was chosen as the appropriate low operating frequency for the sensor, and is in agreement with the conditions for the conductivity approach explained in Chapter 4. As the frequency increases the signal amplitude is more pronounced and $f_2=93.0$ kHz was chosen as the appropriate high operating frequency of the sensor in agreement with the conditions for the conductivity approach in Chapter 4.

Next, 114 scraps of sample set S2 are tested in random order at the two chosen operating frequencies ($f_1=5.0$ kHz and $f_2=93.0$ kHz) to determine the signal to noise ratio (*SNR*) of the sensor. The measured *SNR* of these bottom ash scraps are shown in Figure 5.4, which shows that the sensitivity of the sensor for these bottom ash scraps seems very good. Judging from these results, and assuming 12 dB is the minimum workable *SNR*, it may be approximated from the particle-volume dependence of the magnetic signal strength that particles of halve the size (5x5 mm cross section) may still yield acceptable *SNR* values. However, this extrapolation must be taken with care, because the particles still have to comply with the magnetically ‘thin’ and ‘thick’ conditions at the two chosen operating frequencies in accordance with the model assumptions in Chapter 4.

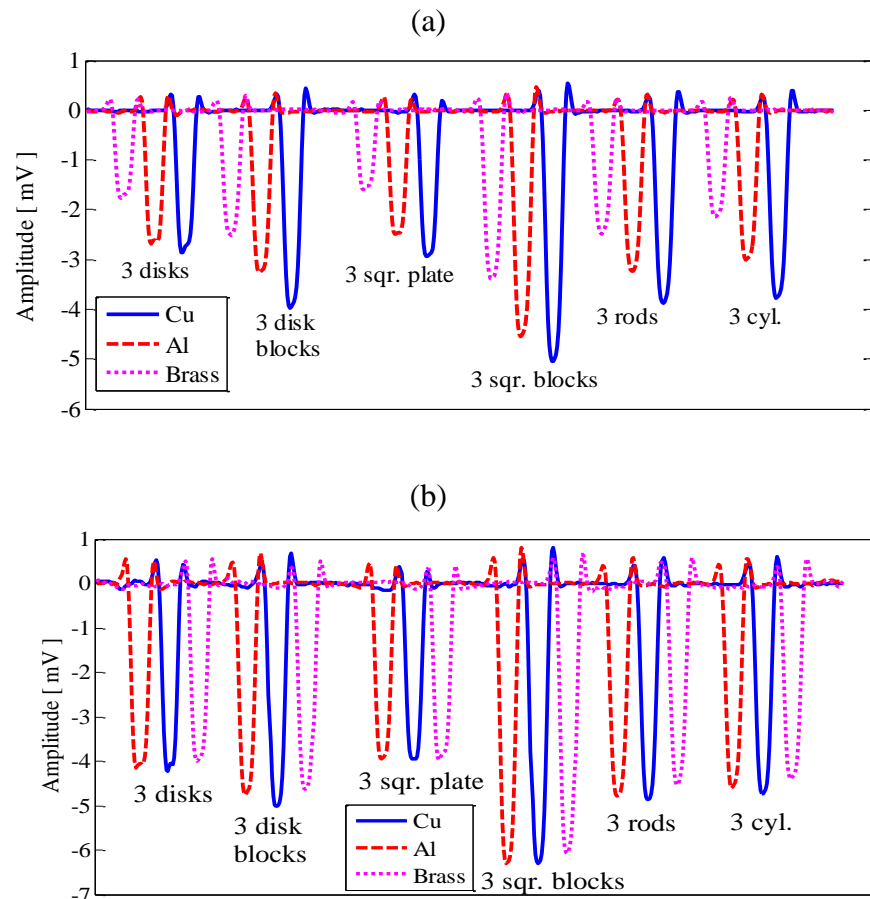


Figure 5.3: Z-responses of the belt sensor using the particles in reference sample set S1 for a constant driving voltage of 8 V_{pp} of the signal generator for the bias coils. (a) At sufficiently low frequency around $f_1=5.0$ kHz. (b) At sufficiently high frequency $f_2=93.0$ kHz.

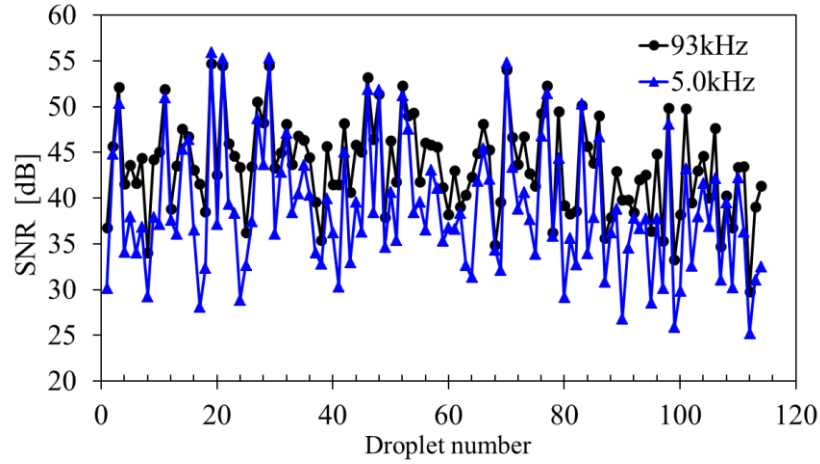


Figure 5.4 Measured SNR (signal to noise ratio) of the demodulated z-response of the belt sensor using 114 scraps of sample set S2 at chosen operating frequencies $f_1 = 5.0$ kHz and 93.0 kHz.

5.3.2 Calculation of the primary magnetic fields B_{1zsum} and B_{2zsum}

This section aims to present the spatial distribution of the magnetic field components of the sensor, especially on the surface of the belt. In order to do that the peak value of the bias current through the bias coils L1 and L2 are calculated using the equivalent circuit shown in Figure 5.5(a), where it is noted that the used voltage amplifier had an output impedance of also 50Ω . Figure 5.5(b) shows the calculated peak value of the bias current for increasing frequency without amplification and with amplification to boost the bias current and sensitivity of the sensor. The calculated value of the amplified peak bias current i_{p1} and i_{p2} at the operating frequencies around $f_1=5.0$ kHz and $f_2=93.0$ kHz are shown in Table 5.1. Here, with $L1=L2=240.4 \mu\text{H}$, the total wire resistance of the two coils combined is $r_w=10.4$ ohm and the used calculated magnetic field coupling constants are $k12=k21=0.42$. This gives the current in the cases with and without voltage amplifier.

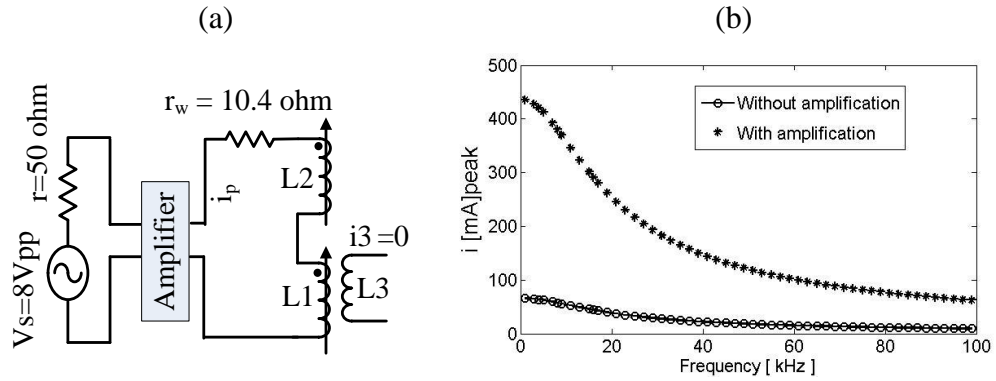


Figure 5.5: (a) An equivalent electrical circuit of the belt sensor including a voltage amplifier having 50 ohm output impedance between the Agilent signal generator and the bias coils of the sensor to boost up the sensitivity of the sensor unit. (b) The calculated value of the peak current i_p through the bias coils L1 and L2 for increasing frequency.

Now the applied magnetic field components of the rectangular like Helmholtz coil at a point in space say $P(x,y,z)$ on the surface of the belt, as expressed in the Eqs.(4.3) to (4.8), are calculated in Matlab at operating frequency $f_1=5.0\text{kHz}$ and presented in Figure 5.6. From Figure 5.6 it is obvious that the z-field component $B_{I_{zsum}}$ is dominant over $B_{I_{xsum}}$ and $B_{I_{ysum}}$. The same conclusion applies for the operating frequency $f_2=93.0\text{ kHz}$ that is shown in Figure 5.7. The z-distance is here defined w.r.t. the center of the bottom coil L1 where the field inside the coil L1 is stronger and the calculated average value of the fields on the surface of the belt at the distance $z = l_z+z_0$ are $(9+8)\text{ mm} = 17\text{mm}$ and $B_{I_{zsum}}=451.0\text{ }\mu\text{Tesla}$ and $B_{2zsum}=72.7\text{ }\mu\text{Tesla}$. It appears that both fields $B_{I_{zsum}}$ and B_{2zsum} are quite homogeneous on the surface of the belt within the horizontal domain $x=-20\text{mm}$ up to $x=20\text{mm}$. The same applies to the field across the width of the belt, because the y-length of the bias coils is even longer than the x-length.

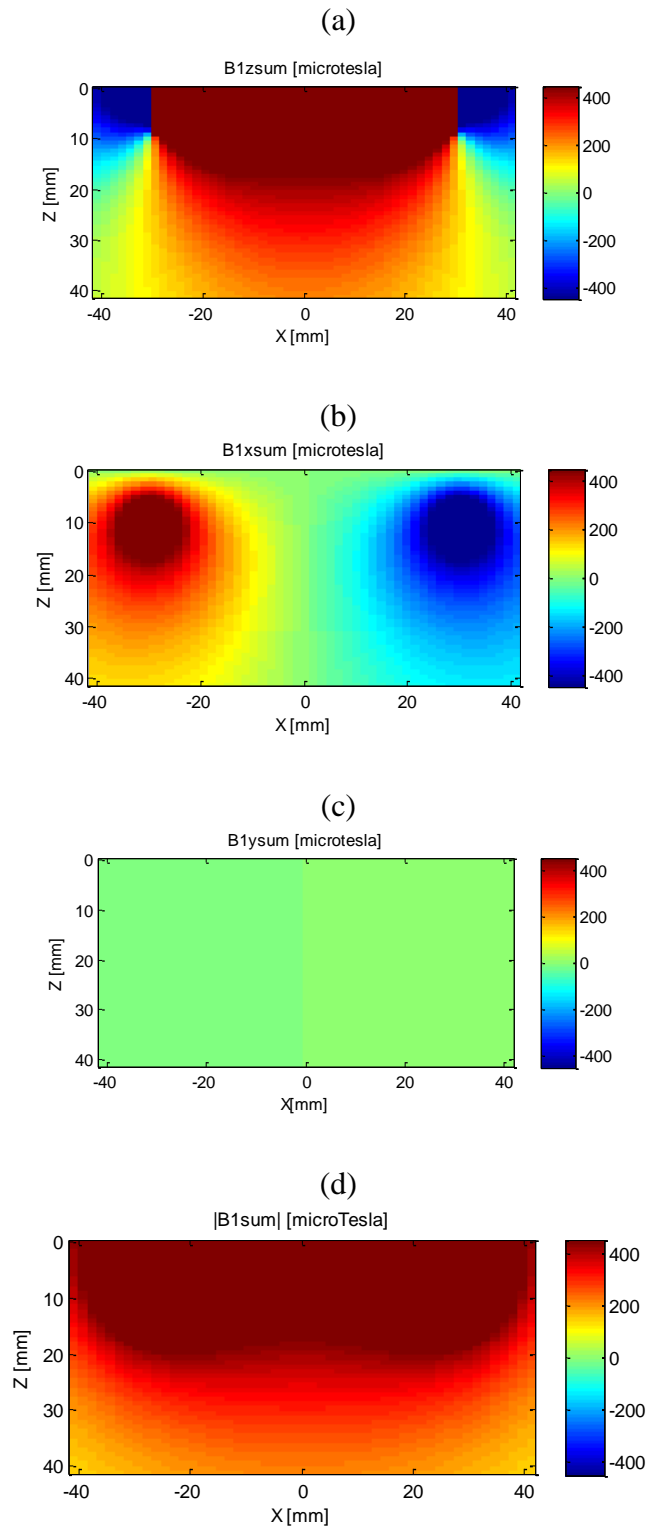


Figure 5.6: Magnetic field distribution at operating frequency $f_1 = 5.0$ kHz of the sensor. (a) Homogenous dominant z-field component B_{1zsum} . (b) Moderately weaker x-field component B_{1xsum} with two strong side lobes, (c) weak y field component B_{1ysum} . (d) The total applied field $|B_{1sum}|$.

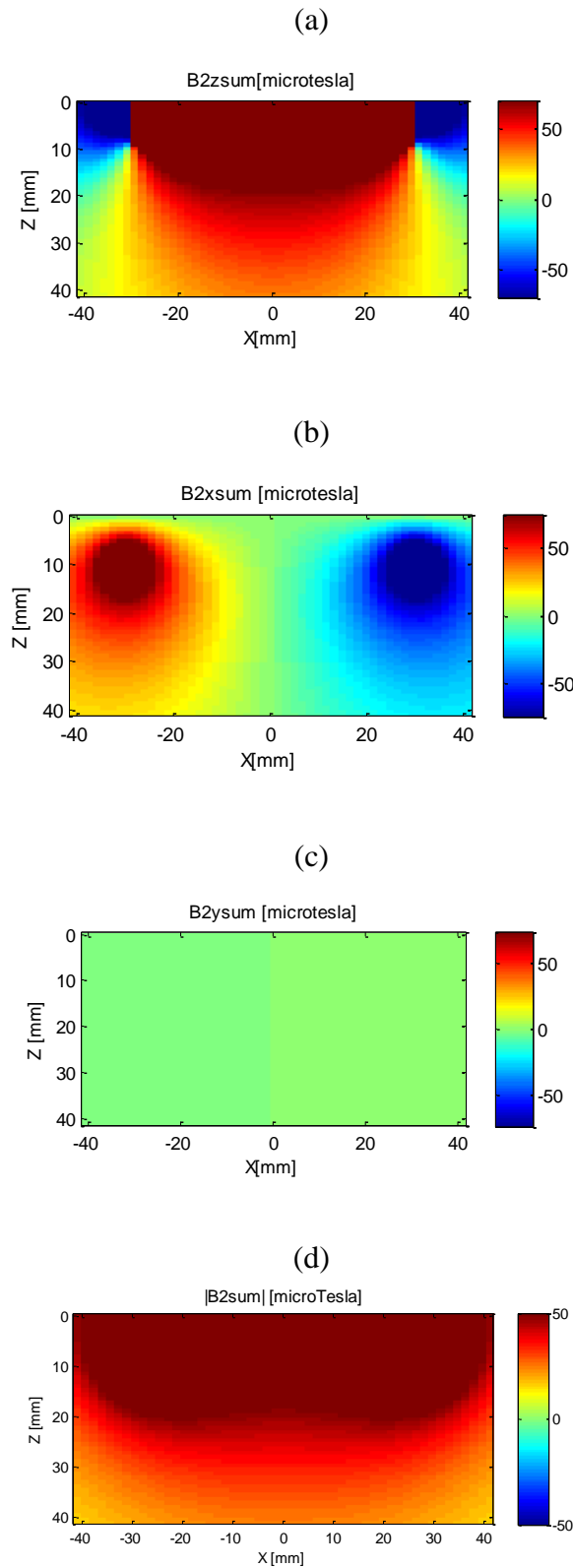


Figure 5.7: Magnetic field distribution at operating frequency $f_2=93.0$ kHz of the sensor. (a) Dominant z-field component B_{2zsum} . (b) Moderately weaker x-field component B_{2xsum} with two strong side lobes. (c) Weak y-field component B_{2ysum} . (d) The total applied field $|B_{2sum}|$.

5.3.3 Conductivity indication factor (*CIF*) of pure sample set S1

This section presents the calculated *CIF* values of the particles in the reference sample set S1 where a subset of six particles per material type is translated on a conveyor belt through the pre-magnetized region of the sensor unit. The responses for each subset are recorded and later analyzed. Figure 5.8 shows the calculated values of *C2* using the Eq.(5.1). The value of *C2* is relatively independent of the conductivity but it does vary significantly with the shape and the orientation of the particles (e.g. standing upright or laying down flat on the belt). This validates the usefulness of *C2* as an independent parameter to characterize the typical shape and height of a metal particle. Evidently, the *C2* for a disk and a square plate are practically the same because they have a similar physical base surface size. On the other hand, for the case of a block particle the *C2* changes significantly as a result of its greater height, but also the base shape and the particle orientation have an influence. Therefore, within the occurring peak amplitude variations, the *C2* is effectively a parameter that scales with particle height and base shape.

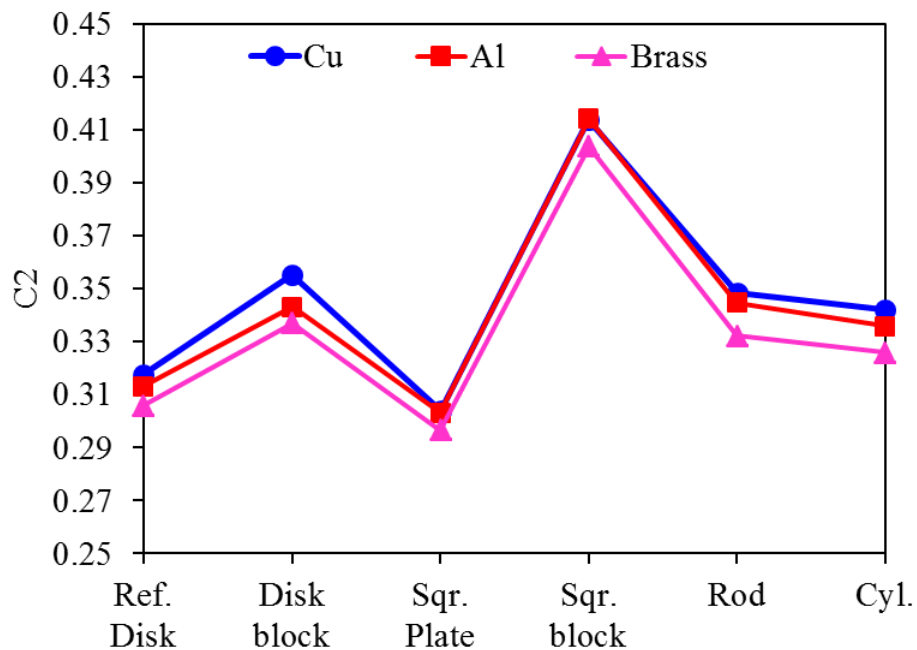


Figure 5.8: Calculated values of *C2* using the Eq.(5.1) that show that *C2* scales for the different shapes and sizes of the particles in the reference sample set S1. It also shows that *C2* is relatively insensitive to the conductivity.

Using Eq. (5.2), the *CIF* for each metal type is calculated and presented in Figure 5.9(a). The *CIF* of each material emerges at a distinct level that is independent of the shape of a particle. An exception is the *CIF* of the Cu disk that drops down to the value of Al. When later on checking the true conductivity of the particles using a standard sigma check NDT probe model no. PSIG001, the conductivity of the Cu disk was indeed found to be quite low compared to pure Cu as it proved to be a low grade Cu alloy as in (CDA publications 1998). The measured and (NDT probe) calibrated conductivity of the particles of the reference sample set S1 is presented in Figure 5.9(b). This figure shows convincingly how sensitive the *CIF* is with respect to the specific conductivity of a particle. Clearly, the average *CIF* for low conductive particles like Brass is certainly low enough to distinguish them from the high conductive particles of Cu and Al. The calculated average *CIF* with one standard deviation of the metal was $CIF_{Cu} = 43499 \pm 1555$, $CIF_{Al} = 38183 \pm 635$, $CIF_{Brass} = 28850 \pm 2237$.

Once the *CIF* of a particle is known then using Eq.(5.3) the conductivity will be determined and converted to an accurate value by multiplying it with the average calibration constant D_{metal} for the specific metal type. Figure 5.9(c) shows the average calibration constant where the calculated average value of D_{metal} was $D_{Cu} = 14.7 \pm 0.54$, $D_{Al} = 7.75 \pm 0.60$ and $D_{Brass} = 5.35 \pm 0$, which show there is a significant dependency of D_{metal} on the type of the metal or, more precisely, on the conductivity of the metal. It should be remarked here that in a blind test the metal type and therefore the appropriate calibration constant D_{metal} is of course unknown at forehand.

However, based on Figure 5.9a, the *CIF* which is based only on the measurements is already determining for which type of metal one is dealing with. The calibration constant D_{metal} therefore serves only to get a more accurate conductivity value for the formerly unknown metal particle. It is noted here that to calibrate the calculated Cu disk conductivity the average D_{Al} is used instead of D_{Cu} . If the particle was truly unknown as in a blind test this choice would also make sense because the *CIF* value of the Cu disk alloy was quite close to that of Al particles. Figure 5.9(d) shows the average relative error between the calibrated conductivity in Eq. (5.3) and the conductivity measured with the NDT conductivity probe.

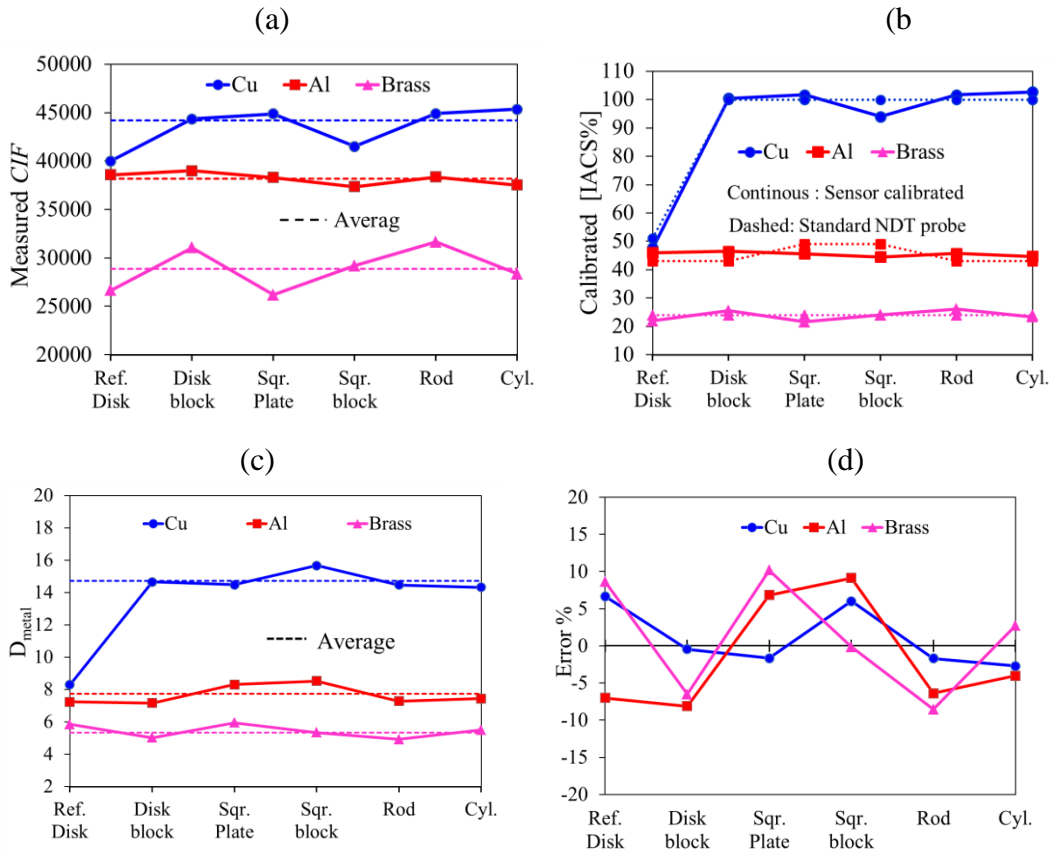


Figure 5.9: (a) Measured CIF of the particles of sample set S1 using the Eq. (5.2). (b) Calibrated conductivity of the particles using the Eq. (5.3). (c) Calibration constant D_{metal} for three distinctive metals. (d) Error % in the estimation of conductivity of the particles of pure sample set S1.

5.3.4 A_{eff} of the particles of pure sample set S1

This section presents the calculated effective surface A_{eff} of the particles of the reference sample set S1. Doing so, we can also test a few aspects of the conductivity approach assumptions from Section 4.4. Using the Eq. (4.23) the A_{eff} can be calculated which is presented in Figure 5.10. Here, the A_{eff} for the flat round reference disk and flat rectangular plate are quite close, confirming the assumption 1 in Section 4.4. However, the disk and square block particles show significant differences even though their base size is identical. This means that the sensitivity to particle shape increases noticeably with particle height, improving the capability of the conductivity approach to distinguish differently shaped particles. This observed shape sensitivity for higher particles does not

affect the assumption 2 in Section 4.4, meaning that the scaling method for higher particles is not impaired where it comes to the estimation of the conductivity of such high particles. In fact, when calculating the conductivity the shape-sensitive parameters $C2$ and A_{eff} do not play an explicit role, but only the ratios of the bias fields and of the detected voltages at the two operating frequencies (cf. Eq. 5.4). This expresses the fact that the shape dependence of the particle is effectively eliminated from the conductivity calculation, as should be the case.

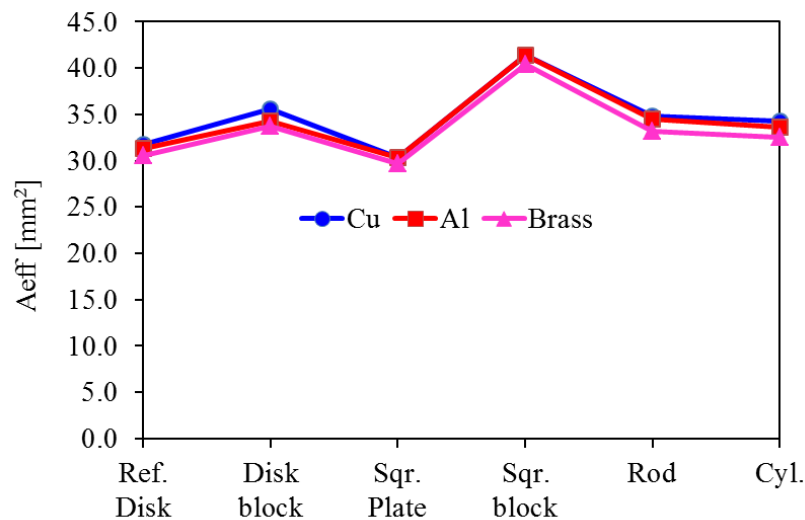


Figure 5.10: Calculated $A_{\text{eff}}=C2A_{\text{disk}}$ of the particles in sample set S1.

5.3.5 Conductivity identification factor CIF for bottom ash scraps

As an application in sensor sorting of metal scrap, a sample set S2 with bottom ash scraps were tested with the belt sensor. The specifications and a photograph of the sample set S2 are shown in Section 5.2. S2 is a representative sample of 114 scraps of different materials such as Cu, Al, Brass and Zn are selected from a batch of bottom ash, size fraction 6.5mm to 15mm. The scraps are randomly mixed up and split into 19 subsets containing six scraps in each subset with an identification mark on each scrap using a letter followed by a number. The letter indicates the material type and the number provides the numerical information of the scrap within the population of the subset. So each subset is a mixer of six scraps of different materials. For example a scrap is marked by A2 i.e. “A” represents the type of the scrap which is aluminum and “2” represents the number of same type in the population of that subset and so on. Afterwards the

scraps of each subset of the sample set S2 are adhered with tape onto the conveyor belt in their natural orientation as it was done for the test of sample set S1. The measurements for all the subsets were recorded. The recorded responses of the subsets were subsequently processed and analyzed in Matlab.

The measured *CIF* of the scraps are sorted in alphabetic order, e.g. Al, Brass, Cu and Zn, which results in a plot of the measured *CIF* shown in Figure 5.11. The average *CIF* line for Cu scraps remains at the highest level and for Al at the intermediate level, followed by Zinc and Brass at the lowest levels. The level of the average *CIF* lines for the bottom ash metals correspond to the a descending order of their conductivities and are just as well separated as in the case of pure metals in the reference sample set. The average *CIF* lines for Brass and Zn are observed to be very close to each other, due to the fact that Brass and Zn both are low conductive metals with Zinc being just a little more conductive than Brass. The fact that the average *CIF* line for Zinc is just above Brass makes it more evident that the *CIF* is a reliable measure of the conductivity. The average *CIF* lines for the metal scraps are $CIF_{av}^{Cuscrap} = 38711 \pm 10174$ (+/-26%), $CIF_{av}^{Alscrap} = 29750 \pm 5746$ (+/-19%), $CIF_{av}^{Brassscrap} = 20302 \pm 4943$ (+/-24%) and $CIF_{av}^{Znscrap} = 21892 \pm 4784$ (+/-22%).

The relative spread in the *CIF* values for the different metals is quite close and lies in the narrow range of 19-26%. Typical commercial alloys are Beryllium Copper, copper strip, cast copper, wrought copper, cast aluminum, wrought aluminum, and aluminum bronze. It is reported that each of these may show significant variations in conductivity (CDA publications, 1998). Despite these natural variations in conductivity, it cannot be completely ruled out that incidentally a very unusual shaped scrap could have influenced the measurements and caused it to show up at the wrong *CIF* level. Physically speaking, this means that such unusually shaped scraps may either produce self-shielding effects, such as through cavities or contortion which distorts the bias field, or such scraps violate the magnetically ‘thin’ or ‘thick’ conditions at the two operating frequencies.

Next we rely on the bottom ash metals sample set at hand, but off course using the *CIF* for a very large number of scraps test will produce better statistically converged results. Thus, the average *CIF* lines are used to provide an effective way for sorting of the different valuable metals from the bottom ash materials.

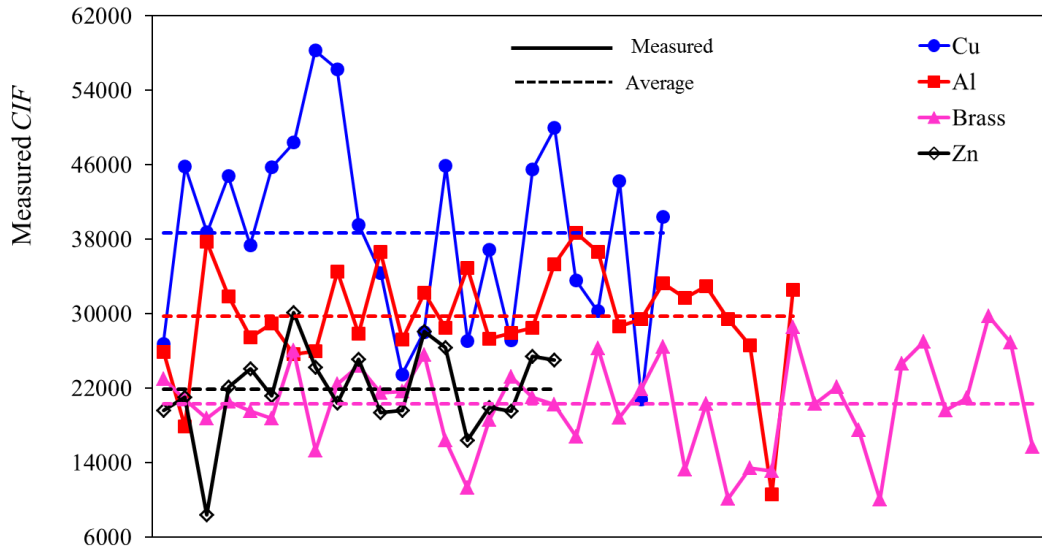


Figure 5.11: Measured conductivity indication factor (*CIF*) using the Eq.(5.2) for the bottom ash scraps of Cu, Al, Brass and Zn shown in sample set S2.

5.3.6 Sorting methodology and sorting statistics of the bottom ash scraps

This section presents a statistics for sorting the scraps of different metals based on their measured average *CIF* values, shown as lines in Figure 5.11. It is noted that the sample set S2 contains 114 metal scraps of which Cu=24, Al=30, Brass=41 and Zn=19. Two sorting methods are applied, first high-low (hi-low) conductive sorting and second high-low-intermediate (hi-low-int) conductive sorting, which options are shown in Figure 5.12. The hi-low method produces two products streams; Collector1 collects the high conductive metals and Collector 2 collects all the lower conductive metals. The second method produces three products streams: Collector 3 collects the high conductive metals, Collector 4 collects the low conductive metals, and Collector 5 collects the intermediate conductive metals. For the hi-low method a detection threshold is based on the

average CIF level of the Brass scraps, and is assigned as $CIF_{threshold}^{hi-low} = CIF_{av}^{Brassscraps} + STD = 25246$, where the STD represents one standard deviation of that average CIF line. For the hi-low-int sorting method an additional detection threshold is taken based on the average CIF level of the Al scraps as $CIF_{threshold}^{hi-low-int} = CIF_{av}^{Alscraps} + STD = 35496$. Next, a logical test is carried out on the measured CIF values of the scraps to count the particles that end up in the different collectors for a specific method.

Figure 5.12 shows the calculated sorting statistics using the hi-low and hi-low-int methods where using hi-low method the Collector 1 contains mainly the high conductive scraps (91.7% of the Cu and 93.3% of the Al scraps) and only a few low conductive scraps, as based on the logical test $CIF > CIF_{threshold}^{hi-low}$. On the other hand the logical test $CIF \leq CIF_{threshold}^{hi-low}$ gives the scraps into the Collector 2 that mainly contains low conductive scraps (78% of the Brass scraps and 78.9% of the Zn scraps). For an industrial metal smelter the highest added value is obtained with a pure Cu product (Cu production), or with a relatively lower value the combination product of Brass-Cu-Zn (Brass production). In either case the main sorting objective is to separate the Al particles from the rest. Here it is noted that in industry purity is related to the mass (i.e. grade), and not to the relative amounts of particles of different types. In this method the Collector 2 provides probably an interesting Brass product, but Collector 1 is still a lower valued Cu-Al mix with still a high amount of the most valuable pure Cu particles. Note therefore that Al is ~3 times lighter than Cu.

Next, it is attempted to improve the sorting with the high-low-int method by adding another level $CIF > CIF_{threshold}^{hi-low-int}$ and thus adding another collector. Collector 3 is essentially a Cu product, but the probably the Al content is a bit too high to speak of a high value Cu product. Collector 4 is more of an Al product but is essentially still a lower valued Cu-Al mix. Collector 5 provides an interesting Brass product with relatively low Al contents. Summarizing, both sorting methods yield at least one valuable Brass product, but the obtainable recovery of the individual metals is not very high in either method. Though this may be

improved slightly by optimizing the used separation levels, the result is mainly influenced by the large spread in conductivity of the bottom ash metal particles.

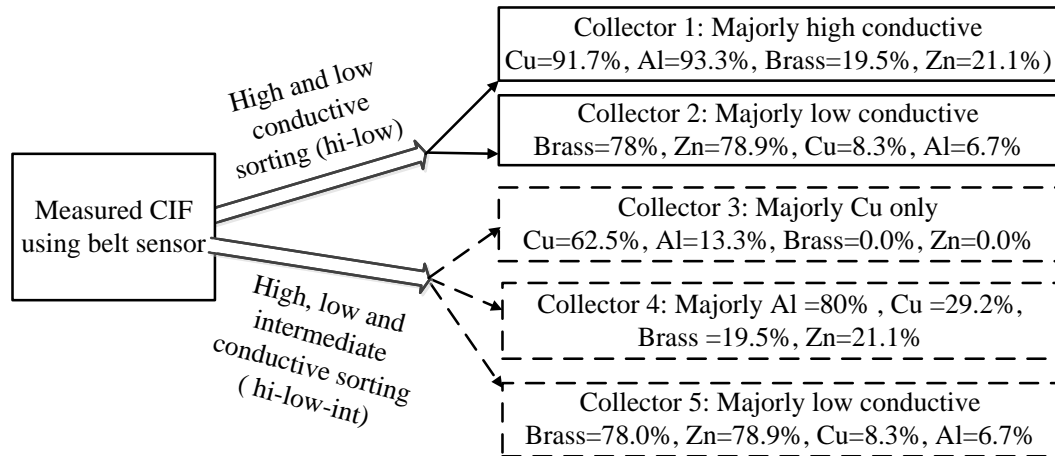


Figure 5.12: Sorting statistics based on the measured *CIF* values of the scraps using a hi-low and a hi-low-int sorting method.

5.3.7 Conductivity of the scraps

This section presents the calculated conductivity of the bottom ash scraps of sample set S2 using the Eq. (5.3). Figure 5.13 (a) shows the results, which are quite offset from the true values. Therefore the value of the average calibration constant *D* shown in Figure 5.9c can be used to scale the conductivity of the scraps for each metal to the correct level, which is shown in Figure 5.13(b).

Figure 5.13b reveals that the bottom ash metals have quite some variation in electrical conductivity. This is to be expected for mainly two reasons. First, these scraps originate from many different end-of-life products, for which the original manufacturers used a wide range of possible alloys and pure metals. For example, due to the development of material science and technology Cu sheets with conductivity higher than 100.0 IACS% is attainable by advanced processes that can remove even the most minute impurities and defects (Simon et. al 1992).

Second there is the waste mixing and the thermal and chemical conditions in the municipal solid waste incinerator, including temperatures of around 1000 C°. Such conditions can create several effects in a metal. On the one hand certain alloying elements may diffuse outwards, changing most noticeably the surface conductivity of a metal scrap for which the high frequency in the proposed sensor unit is the most sensitive. On the other hand, foreign elements may fuse with the metal, again causing most noticeably changes in conductivity at the surface of a scrap.

The relative spread in the conductivity for the different metals in Figure 5.13 b is the same as in the *CIF* values in Figure 5.11 and lies in the narrow range of 19-26%. This finding about bottom ash scraps is new and has not been reported before, because to date only the proposed belt sensor technology is capable of measuring the conductivity of such bottom scraps in larger numbers in their original shape. Nevertheless, the reasons for why these spreads are so uniform for the different pure metals and alloys are beyond the scope of this research. As noted before, some bottom ash particles have such a complex shape that their calculated conductivity does not reflect the true value. But also contaminations with for example oxides or other foreign materials can influence the measured conductivity. As an example, a few scraps of complicated shapes are presented in Figure 5.14(a) and (b). Nevertheless, these complex shapes are exceptions and are not expected to be a statistically important fraction among the bottom ash metals.

Coming back to Figure 5.13b, it is not realistic that some bottom ash scraps have a conductivity well above 120.0 IACS%. This means that the accurate measurement of the highly conductive copper scraps using the belt sensor model shows a deficiency. When turning to Sections 4.3 and 4.4, the model assumed that mutual induction could be ignored and self-induction will scale proportional to the detected voltage. However, ignoring these effects will result in larger calculated eddy current which in turn are associated with a higher conductivity than is realistic.

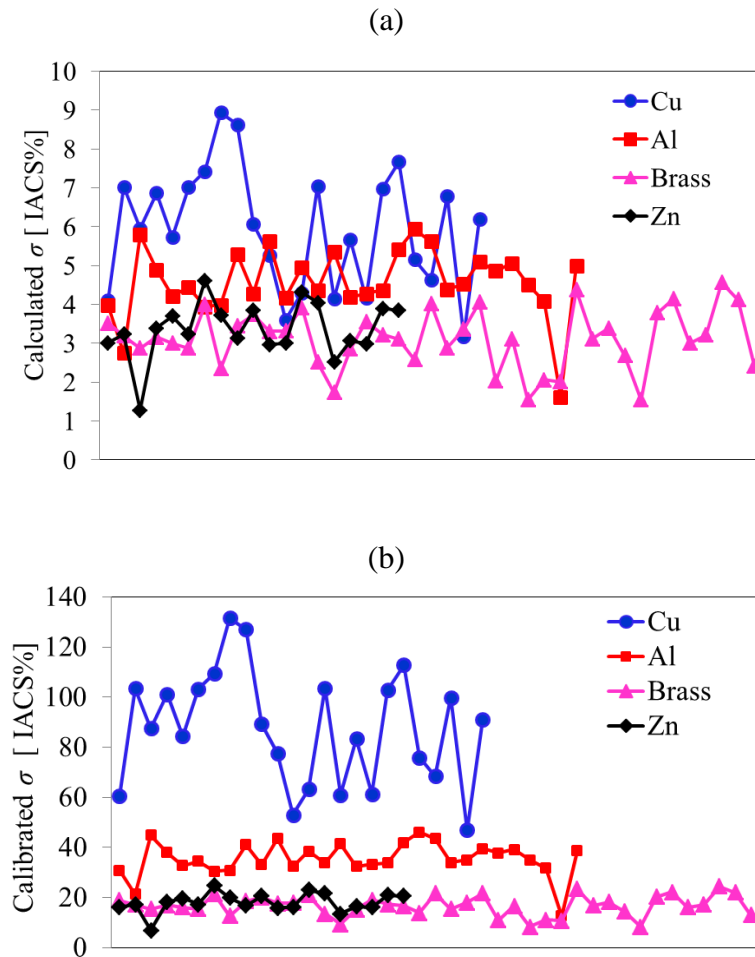


Figure 5.13: (a) Calculated conductivity using Eq. (5.3) of the scraps of sample set S2 without calibration constant D_{metal} . (b) Calibrated conductivity of the scraps of sample set S2 using the average calibration constant D_{metal} from Figure 5.9c.

After the conductivity tests a representative number of Al, Brass and Zn scraps from batch S2 and a few Cu scraps from a different bottom ash batch of relatively larger size, all with suitable shape and size, are collected and flattened by heating and hammering to render them suitable for conductivity measurement using the commercial NDT conductivity probe. The aim of using of these measurements is to have an idea about where is the true conductivity of the bottom ash scraps and the standard NDT probe provided the only reference available to us. The conductivity for these preprocessed scraps is presented in Figure 5.14(c), (d), (e) and (f). Note that these flattened samples are relatively larger compared to the original sample set S2. It is noted that the conductivity of the scraps shown in Figure 5.14(a) and (b) could not be measured using the

standard probe, because their shapes were exceptionally complex and these particles broke up during the heating and flattening. Figure 5.15 shows the measured conductivity of the preprocessed scraps of Figure 5.14(c), (d), (e) and (f) using the standard conductivity probe, model PSIG001. From the Figure 5.15 it is obvious too that the conductivity of the scraps varies quite a lot and that is the reason why some of the scraps entered another *CIF* level (see Figure 5.11).

Another observation from Figure 5.15 is that the pure copper particles are far less conductive and show relatively more spread in conductivity than when using the belt sensor in Figure 5.13b. This is attributed to the effects of the heating and hammering that tended to contaminate and modify the crystalline copper. This can result in a significantly lower measured conductivity than what the scrap had in its original shape. Also, keeping contact with a sufficiently large and flat surface is vital for an accurate NDT probe measurement, which was not easy since the hammered particles were not really perfectly flat or smooth. It is remarked that an alloy such as brass is apparently less susceptible to the effects of heating and hammering.

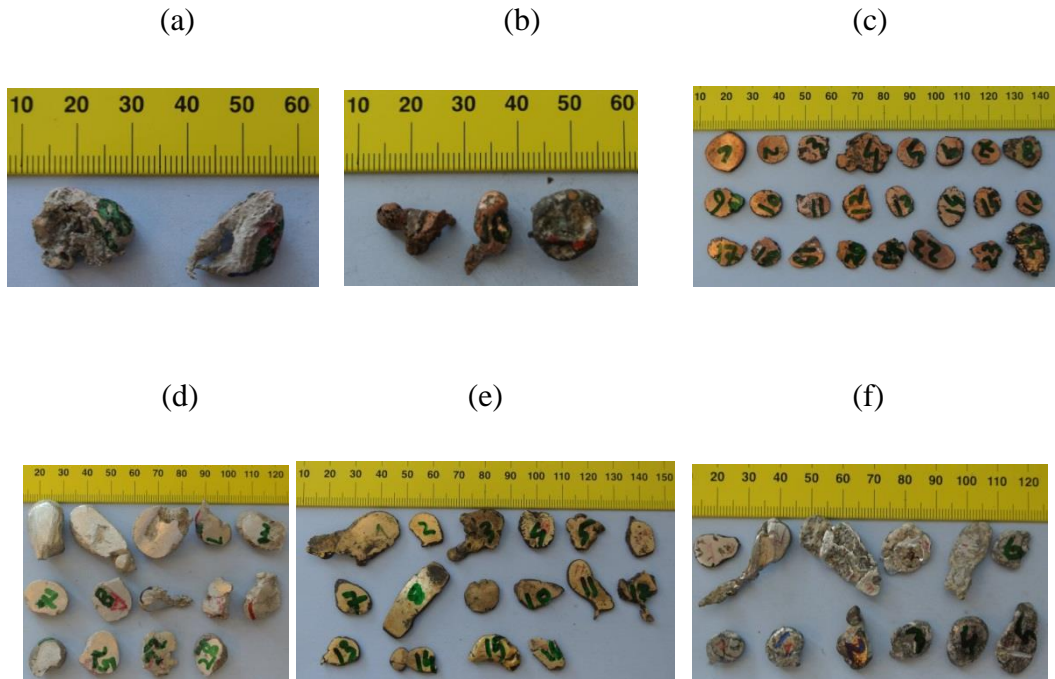


Figure 5.14: (a) Al scraps and (b) Cu scraps with complicated shapes, including cavities and contortions. The next panels show preprocessed and flattened particles of: (c) Cu scraps. (d) Al scraps. (e) Brass scraps and (f) Zn scraps.

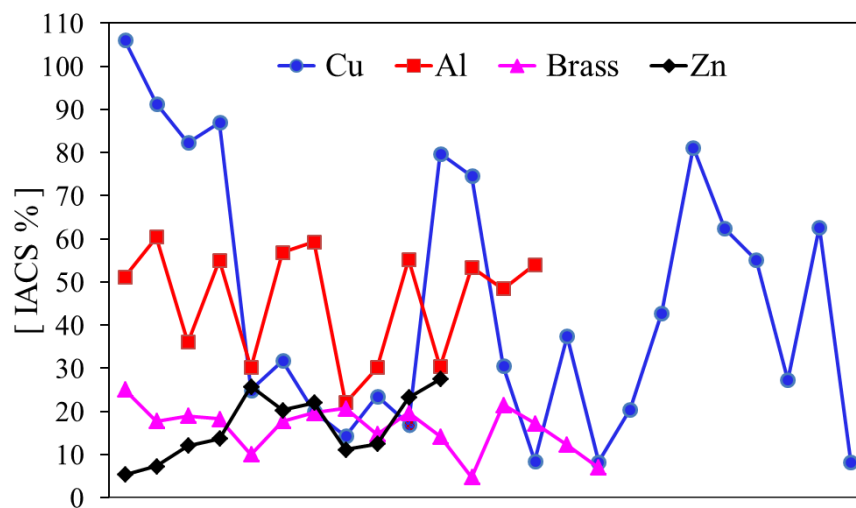


Figure 5.15: Measured conductivity of the preprocessed and flattened scraps of Figures 5.14(c), (d), (e) and (f) using the standard conductivity meter, model PSIG001.

5.4 Discussions:

The calibration constant D_{metal} was found to be different for different types of metal. In fact, the average values found were $D_{Cu} = 14.7 \pm 0.54$, $D_{Al} = 7.75 \pm 0.60$ and $D_{Brass} = 5.35 \pm 0$ (see Figure 5.9c). The causes for this behavior point mainly to deviations related to the magnetic moment model assumption 2 in Section 4.3 and the conductivity approach assumption 2 in Section 4.4: mutual induction with the power source-transmission coils was to be neglected and the self-induction for thicker particles would scale with the detected response. To explain the implications, let us consider the Eq.(5.4) where the ratio of applied magnetic fields in the first factor stems from the induction fields induced at the particle according to the model in Section 4.3. To introduce the effect of self-induction of the particle, or similarly the effect of mutual induction between the particle eddy current and the Helmholtz coils, a factor $k < 1$ is used to multiply those field components. Thus we can obtain a corrected expression for Eq. 5.4 and by focusing only on the effect of the k -factors for the two operating frequencies we conveniently write the corrected expression in a simple form as

$$\sigma \sim k_2^{4/3} / k_1 \quad (5.5)$$

Note that in essence we state here that the right hand term in Eq. 5.5 is equal to $1/D_{\text{metal}}$. Two cases are now discussed. In the first case we assume that k is related to the particle self-induction only. The effect of self-induction is to increase the impedance (inductance) of the particle and therefore it lowers the induced eddy current (so $k < 1$). To simply matters we assume in this case that the frequency has little or no bearing on the degree of field-coupling, so $k_1 = k_2$. The factor k is unity ($k=1$) for thin disks for which the self-induction is taken correctly into account in the analytical expressions. However, if the particle becomes larger and/or changes shape the effect of self-induction may become relatively stronger than for a thin disk, while also the eddy current become stronger which increases energy absorption. As such, the complex impedance of the particle may change significantly with respect to the reference disk particle. This change is taken into account in the conductivity approach only by scaling the reference disk magnetic moment according to the increase in the detected signal

voltage for the test particle. It is also remarked here that the experiments involve only a single z-receiver below the conveyor belt, which gives in some ways a limited amount of information about the total magnetic field produced by the particle. Nevertheless, the effect self-induction on the resulting complex impedance is expected to become relatively stronger for particles other than a thin disk, because in a disk the eddy current run only in two opposite parallel surfaces which limit the degree of coupling that can take place. In contrary, in larger and more complex shaped particles the eddy current will run in several different directions of the various particle surfaces (e.g. different eddy current are more within 'visual range') which gives rise to a higher degree of coupling that increases the effect of self-induction. This causes that the increase in the detected signal voltage is lower than one would expect, leading to an underestimation of the true increase in size and/or conductivity of the larger particle. The result is that $k < 1$ in Eq. (5.5). This conclusion appears consistent with the finding that the conductivity is estimated too low for all the real metal particles in our experiments, which is evident from the calibration constant D being larger than unity for all metal scraps.

In the second case we assume k in Eq. (5.5) to be a coupling factor that is related only to the mutual induction between the particle and the power source-transmission coils. In essence, this is an effect similar to impedance matching which effect also limits the maximum power available to the particle eddy current. Here it is reminded that in this work the Helmholtz coils are steered using a voltage source, meaning that the applied current (and thus the power delivered to the magnetic field) has no possibility to increase beyond a certain level and accommodate the possibly larger power required for the better conductive and/or the larger particles. Also, the power absorbed by the particle increases as the square of the frequency, meaning the effect of mutual inductance is much larger for the higher frequency ω^2 . This implies $k_2 < k_1$. This mutual inductance effect explains why D_{metal} increases for increasing conductivity (thus decreasing ratio k_2/k_1) of the metal scrap particles. The magnetic field at the particle is 'drained' from energy and becomes significantly smaller than the magnetic field was during absence of the particle. Thus the particle eddy current become smaller, which is

effectively modeled in Eq. (5.5) by letting the ratio k_2/k_1 become smaller as it mostly affects the higher working frequency.

When regarding the results in this chapter, it appears that self-induction is the lesser problem that could be overcome with a calibration method. The nonlinear effect of mutual induction is much more of a nuisance, but may be minimized in the experimental setup by using current steering for the Helmholtz coils which allows the source voltage to change freely. This type of power source will allow for a theoretically unlimited power flow to the magnetic field to feed eddy current, while maintaining a reference level of the applied magnetic field near the metal particle that is linked to the electrical current sent through the transmission coils. Another possible improvement of the model in Chapter 4 concerns the parameter C_2 in Eq. 4.23. There we chose to use just the one parameter in both the high and low frequency field relations in Eqs. 4.24 and 4.25. Moreover, we chose to derive the C_2 in the easiest way by using the high-frequency measurement (see Figure 5.8) which, as discussed above, is more susceptible to mutual induction influences. Possibly, by matching a separate parameter C_2 for the high and low frequency fields an improved match with the measurements may be obtained, after which the ‘Conductivity approach assumption 3’ in Chapter 4 can be eliminated.

Another issue that may have affected the accuracy of the model calculations is related to the magnetic moment model assumptions 3 and 4 in Section 4.3 that the metal particles must be ‘magnetically thick’ at the high operation frequency, but ‘magnetically thin’ (i.e. easy penetrable) at the lower frequency. Specifically for the lower frequency this may not be achieved for all particles in the bottom ash scraps experiments. For example, the depth of magnetic penetration of the pure Cu, Al, and Brass is related to 3 skin depths as listed in Table 5.3 for the cases where the magnetic field is applied either at one side or at two sides of the particle, where the latter is the most relevant in the present setup.

Table 5.3: One and two sided magnetic penetration depths (3 skin depths) for three metal types.

Metal	One side		Two sides	
	5 kHz	93 kHz	5 kHz	93 kHz
Cu	2.8 mm	0.65 mm	5.6 mm	1.3 mm
Al	3.6 mm	0.83 mm	7.2 mm	1.6 mm
Brass	5.2 mm	1.2 mm	10.4 mm	2.4 mm

When comparing with Table 5.2 it shows the sizes of the designed flat reference samples comply very well with the thick and thin conditions. Seemingly, the Cu and Al block particles did not comply at the lowest operating frequency, but the measurement results showed that full magnetic penetration at the low frequency may not be required to get a satisfactory result. However, it was also not technically possible in the present setup to lower the frequency any further without significant loss of sensitivity. Of course, no such design care could be taken for the real bottom ashes sample set S2 and it is quite likely that some particles did not comply, especially where it concerns the thin condition at the high operating frequency. The uniqueness of detection, which is a theoretically fundamental problem in the identification of objects using sensor measurements, is in this particular case that two very different metal scraps may have practically the same magnetic moment or, equivalently, the same complex impedance. Fortunately, looking at other technologies for object detection such occurrences prove to be rare and it is also not believed to pose an obstacle for successful application of the presently proposed metals scraps identification technology.

5.5 Conclusions:

This chapter presents the results of a belt sensor that successfully brought an experimental verification of the conductivity approach for the identification of the NF metals being translated on a conveyor belt. The conductivity approach is built on pragmatic approximations of the exact eddy current theory where a disk model is extended to represent a scaled model of particle with six generic shapes: disk, disk block, square plate, square block, rod and cylinder, called reference sample set S1. Using these pure samples the belt sensor showed the assumptions made in the conductivity approach were valid and the calculations came very close to the sensor data. The belt sensor was tested with the sample particles of the reference sample set S1 and a sample set S2 with real bottom ash metal scraps. The sensor performance was quite repeatable and sensitive enough to detect the change in conductivity. For example, it was observed for the case of one Cu disk particle, which unexpectedly had a lower conductivity, that it correctly entered the *CIF* level of Al particles (see Figure.5.9). For the particles of the pure metals sample set S1 the average value of the *CIF* lines were $CIF_{Cu} = 43499 \pm 1555$, $CIF_{Al} = 38183 \pm 635$, $CIF_{Brass} = 28850 \pm 2237$ that can be used for the identification of different particles of different metals.

Once the material *CIF* is known then the conductivity of the particles can be calculated using the Eq.(5.3) with the average accuracies $-0.1 \pm 3.5\%$ for Cu, $-1.6 \pm 7.9\%$ for Al and $1.0 \pm 7.5\%$ for Brass, where the average value of the calibration constant *D* was $D_{Cu} = 14.73 \pm 0.54$, $D_{Al} = 7.75 \pm 0.60$ and $D_{Brass} = 5.35 \pm 0.42$ (see Figure.5.9c). The causes of this calibration factor have been linked to basic assumptions behind the magnetic moment model, but also other potential improvements to the setup and issues related to the proposed conductance model have been discussed.

As an application of the sensor the *CIF* of the sample set S2, which is a set of bottom ash scraps of different materials such as Cu, Al, Brass and Zn, was measured and presented in Figure 5.11. The average *CIF* lines of the scraps of a specific metal turned out lower than those for the pure sample set S1 (cf. 5.11 & 5.9a). This was expected because the scraps were exposed to waste incinerator conditions that rendered them less pure, while their shapes were also particularly more complicated than the generic particles of reference set S1. The large

variation in conductivity will complicate the positive identification of the irregularly shaped and heat-affected bottom ash metals. However, for quality inspection of an already pre-sorted product, for example scanning the contents of a high-grade copper product with low level of Al contamination, the belt sensor may yet be able to provide an acceptable prediction of the Al contents. A condition is that a large-scale test is carried out on the specific product at hand to provide statistically converged results that allow for a reliable assessment of the belt sensor performance.

Based on the measured average *CIF* lines two sorting methods were tested using a logical approach: high and low conductive sorting (one detection level) and high-low-intermediate conductive sorting (two detection levels). Logical testing showed that sorting is possible to a limited degree. Using hi-low sorting the material composition of particles in the high conductive collector was Cu=91.7%, Al=93.3%, Brass=19.5%, Zn=21.1% and in the low conductive collector it was Brass =78%, Zn=78.9%, Cu=8.3%, Al=6.7% (see Figure 5.12).

For the hi-low-int method the particle material composition was Cu=62.5%, Al=93.3%, Brass=0.0%, Zn=0.0% in the high conductive collector and Brass =78%, Zn=78.9%, Cu=8.3%, Al =6.7 in the low conductive collector. The remainder of the particles ended up in the intermediate collector. As may be expected, the resulting logical sorting performance is also limited due to the inherently large variation in conductivity of the bottom ash particles. As such, the conductivity alone does not seem to offer enough distinctive information to sort this type of metal scrap. An option would be to combine it with the effective area information that is also delivered by the belt sensor. This parameter is linked to the shape of a particle, which in turn is linked to a specific metal as determined by the end-of-life product it originated from. In this way the belt sensor may indeed offer a more effective method to allow for more reliable metals sorting as well as more reliable quality inspection.

References:

- Grover W.F.**, 1973, Inductance Calculations Working Formulas and Tables, Dover Publication, Inc. New York, N.Y.10014, ISBN 0-87664-557-0, pp.70-73.
- CDA Publications** 122, 1998, High Conductivity Copper for Electrical Engineers, available at Copper Development Association website, www.cda.org.uk.
- Simon N.J.** Drexler E. S. Reed R. P. 1992, Properties of Copper and Copper Alloys, NIST Publications 177.

Chapter 6

Conclusions and recommendations

6.1 Conclusions

This thesis primarily is devoted to research on the development of a hybrid sensor that can be applied inline for the quality control of concentrated nonferrous (NF) scrap metals. These scraps are recovered from municipal solid waste incinerator (MSWI) bottom ash materials, size 1-6mm, by using state of the art eddy current separator (ECS) technology. As a result a proposed hybrid sensor was developed in this research and tested in laboratory and in-situ for online detection of metal grade (G) of the NF metal concentrated fraction, where it was considered that the metal grade is a significant qualifier that can be used effectively for the continuous adjustment of the splitter settings of the ECS machine. The hybrid sensor is composed of two basic sensor sections namely infrared sensor (IRS) and electromagnetic sensor (EMS), where the IRS section gives total count data for all particles in the sample stream and the EMS section gives only the count data for the NF metal particles present in the stream. Each sensor is characterized in terms of sensitivity, repeatability and accuracy.

During the characterization phase the count correction factors (C^{IRS} and C^{EMS}) for each sensor type were experimentally determined at average particle feed rates ranging from 7 to 219 particles per second using synthetic samples of known composition (cf.2.5a and b, Chapter 2). The count data for both sensors were highly repeatable (see Table 2.3). At low feed rate ≤ 13 particle per second the C^{IRS} and C^{EMS} were close to unity but at higher feed rate these were increasing that was due to the simultaneous falling of some particles through the sensor but that number of missing particles was quite repeatable that gave a possibility for applying the count correction factors to eliminate this stationary error by calibration.

A method for the detection of metal grade (G) of the falling particle stream was developed and validated using synthetic samples at different values of (k) average particle mass ratio between non-metal and metal where for synthetic samples the used values of k were 2.69, 1.23, 0.54, and 0.24.

As an application of the hybrid sensor a representative amount of bottom ash materials was tested (see Table 2.4). The hybrid sensor showed excellent performance in measurement of G with an accuracy of 2.4% at average feed rate of 13 particles per second. Using the sensor count data and manual analyses of metal grade of these bottom ash materials the value of k was estimated which was $k = 0.49 \pm 0.07$ at moisture content 7.1wt%.

Afterwards for functionality analyses a prototype of the developed hybrid sensor is built in a compact way to give some degree of robustness and then tested in laboratory with some controlled experimental conditions and in situ. The average and standard deviation for the differences in metal grade between the sensor measurements and the manual analyses were 0.0% +/- 1.8% using a moist batch in the laboratory with 10.7% moisture content, 1.5% +/- 6.0% in-situ using the dry ashes from batch I with 4.7% moisture content, and 3.1% +/- 11.8% in-situ using the wet ashes from batch I with 13% moisture content. Crucial for measurement accuracy was the correct value of k , which is the ratio of average mass of all mineral and metal particles in the whole batch. The measured average values and standard deviations were $k = 0.48 \pm 0.04$ in the laboratory, $k = 0.60 \pm 0.20$ in-situ for the dry ash and $k = 1.22 \pm 0.49$ in-situ for the wet ash (cf. 3.3a and 3.6) which showed that the average values for k were sufficient for accurate measurement of the metal grade. The measurements and trends in sensor data from the laboratory and in-situ dry feed are quite comparable, considering the ECS machines were different and the bottom ashes came from different sources. Both the metals recovery (metals content ratio of product and feed) and grade proved sensitive to the splitter distance.

From laboratory test it showed that a 10 mm shift may produce 10% change in recovery or 18% change in grade, while over the range of 40 mm splitter distance the grade and recovery both change by at least a factor two (cf. 3.5). On the other hand the trend for grade sensitivity against splitter position in in-situ was quite comparable and convincing with the laboratory results (cf. 3.5, 3.7 and 3.10). In conclusion, the hybrid sensor unit may find its application in online product quality control or it may be used in automated control over the optimum ECS splitter distance.

After completion of the hybrid sensor research this research was extended to a fundamental issue in the field of sensor sorting of nonferrous (NF) scrap metals from waste by means of eddy current technique. In order to do that a model for the eddy current belt sensor was proposed in this thesis with a theoretical conductivity approach for the identification of different NF scraps on a conveyor.

For experimental validation of the conductivity approach the eddy current belt sensor was constructed and characterized using a set of pure samples S1 of different NF metals (Cu, Al and Brass) each of six generic shapes such as disk, disk block, square plate, square block, rod and cylinder. All experimental results of the belt sensor have been presented in Chapter 5 and the theoretical basis is described in Chapter 4. Using these pure samples the belt sensor showed the assumptions made in the conductivity approach were valid enough and the calculations came very close to the sensor data. The tests using the pure sample set S1 produced a database of *CIF* lines for Cu, Al and Brass which were $CIF_{Cu} = 43499 \pm 1555$, $CIF_{Al} = 38183 \pm 635$, $CIF_{Brass} = 28850 \pm 2237$ that can be used for the identification of different particles of different metals on a conveyor. The sensor performance was quite repeatable and sensitive enough to detect the change in conductivity. Actually the measured value of the *CIF* for different materials was different therefore this thesis recommended that a database of material *CIF* can be obtained from where the material can be distinguished from each other. Moreover the conductivity of the particles was calculated using Eq. (5.3) after knowing the *CIF* value of the particle with an average accuracies $-0.1 \pm 3.5\%$ for Cu, $-1.6 \pm 7.9\%$ for Al and $1.0 \pm 7.5\%$ for Brass, where the average value of the calibration constant *D* was $D_{Cu} = 14.73 \pm 0.54$, $D_{Al} = 7.75 \pm 0.60$ and $D_{Brass} = 5.35 \pm 0.42$ (see Figure 5.9c).

Then, as an application of the belt sensor, the same method was applied for the identification of the different precious metal scraps in a sample set S2 of bottom ash materials. A test was carried out using these scrap particles that produced average *CIF* lines which were presented in Figure 5.11. On the basis of the measured average *CIF* lines of the scraps a sorting statistics was produced by logical test using the methods, first high and low (hi-low) conductive sorting, second high low intermediate (hi-low-int) conductive sorting. The hi-low

conductive sorting method produced a statistics of the scrap particles where in high conductive collector the composition of sorted materials was Cu=91.7%, Al=93.3% Brass =19.5%, Zn=21.1% and in low conductive collector was Brass =78%, Zn=78.9%, Cu=8.3%, Al=6.7%. On the other hand the hi-low-int conductive sorting method produced the statistics where in high conductive collector the composition of sorted materials was Cu=62.5% Al=13.3%, Brass =0.0%, Zn =0.0% and in low conductive collector was Brass= 78.0%, Zn=78.9%,Cu =8.3% Al=6.7% while the rest of the scraps went into intermediate conductive collector. It can be concluded that the eddy current belt sensor, possibly in combination with other sensor sorting technique, can be useful for accurate sorting of metal scraps from MSWI bottom ash waste.

6.2 Recommendations

Moisture content and fines are two vital parameters that interfere the performance of an ECS. The bottom ash material sometimes becomes too dry that produces lots of fines by breaking and dissociation of materials in a bottom ash treatment plant. The produced fines can be accumulated on the surface of the optical IRS section of the hybrid sensor which can alter the sensitivity of the sensor that can cause a significant drop of the hybrid sensor in accurate measurement of metal grade (G). Therefore the result of this will be a complete misguide of the splitter setting of the associated ECS machine and possibly a malfunction in quality control of the NF concentrated fraction of the bottom ash materials. Therefore from practical point of view the thesis recommends to use some sort of technical remedy like regular air flashing for removal of fines from the inside of sampling tube.

On the other hand the moisture contents of the bottom ash materials may vary from 10 wt% to 20 wt%. But for very high degree of moisture content some complications may occur for example if the bottom ash materials looks very wet that the particle statistics may be changed completely which means all of the fines will be adhered with the particles and particles themselves may become heavier due to the absorbed water. Sometimes it can be an issue that these wet particles may get stuck to the inside wall of the sampling tube and etc. All of these unexpected situations may occur simultaneously if the bottom ash materials are

completely open to heavy rain for longer period of time or if the ECS machine is operating in open air in a heavily rainy day. However, to avoid these unexpected and extreme situations for the case of high degree of moisture content this thesis recommends having some sort of special cleaning process for removing the watery stuffs from the tube or special care for correcting the k value for wet bottom ash materials.

Now let us present some recommendations for further advancement of the belt sensor research. For identification of different NF scraps on a conveyor the conductivity approach was the driving tool of the eddy current belt sensor. The conductivity approach model overlooked the effect of self-induction and mutual induction of a particle for inherent variation of these shapes and also did not consider the effect of different frequencies on calculation of the effective parameter $C2$ which was actually interpreted as an equivalence of the projected field surface of a particle with respect to the thin reference disk. For example the value of conductivity calibration constant D was $D \gg 1$ which was also varying with respect to conductivity of the materials. Probably the conductivity of the particles had significant impact on self-induction that can also change the coupling between applied and scattered field of a particle. So the conductivity approach model could be more efficient and exact if at least these effects could be adopted by introducing variables which are related to particle shape, self-induction, mutual induction and frequency.

In parallel with the conductivity sorting there might have been some shape correlations among the type of the materials in bottom ash scraps. For example most of the Al scraps in bottom ash materials are found to be flat type, Cu scraps are found to be ball, wire, or rounded droplet type, and etc. So the capabilities of identification of different shapes could also be used as a second parameter in conjunction with the measured CIF and that could improve the sorting accuracy of the materials. . These issues may lead to new research problems for further advancement of sensor research in the field of quality control and sensor sorting of NF metal scraps in MSWI bottom ash materials.